Neutron-Induced Scintillation in Organics

Mauritzson, Nicholai

2023

Link to publication

Total number of authors:
1

Neutron-Induced Scintillation in Organics

NICHOLAI MAURITZSON
DEPARTMENT OF PHYSICS | FACULTY OF SCIENCE | LUND UNIVERSITY

Neutron-Induced Scintillation in Organics

Neutron-Induced Scintillation in Organics

by Nicholai Mauritzson

LUND
UNIVERSITY

Thesis for the degree of Doctor of Philosophy
Thesis advisors: Dr. Kevin Fissum, Dr. Hanno Perrey, Dr. Francesco Messi,
Dr. Robert Frost
Faculty opponent: Professor Tom Davinson

To be presented, with the permission of the Faculty of Science of Lund University, for public criticism in the Rydberg lecture hall at the Department of Physics on Friday, the 31st of March 2023 at 13:15.

Organization	Document name
LUND UNIVERSITY	**DOCTORAL DISSERTATION**
Department of Physics Box 118 SE–221 00 LUND Sweden	Date of disputation 2023-03-31
	Sponsoring organization
Author(s) Nicholai Mauritzson	

Title and subtitle
Neutron-Induced Scintillation in Organics

Abstract

Neutrons are widely used as probes of matter to study materials in a broad range of fields from physics, chemistry and medicine to material sciences. Any application utilizing neutrons needs to employ a well-understood and optimized neutron-detector system. This thesis is centered on fundamental aspects of neutron-detector development, including the establishment of the Source Testing Facility at Lund University, experimental methods for the in-depth characterization of scintillator-based neutron detectors and analytical and computational methods for the precise interpretation of results. It focuses on the response of liquid organic scintillators to fast-neutron and gamma-ray irradiations, specifically for NE 213A, EJ 305, EJ 331 and EJ 321P. A simulation-based method for detector calibration was developed which allowed for the use of polyenergetic gamma-ray sources in this low energy-resolution environment. With an actinide/beryllium neutron source and a time-of-flight setup, beams of energy-tagged neutrons were used to study the energy-dependent behaviour of the intrinsic pulse-shape of NE 213A and EJ 305 scintillators. The results demonstrated the advantages of the neutron-tagging method and how the combination of neutron tagging and pulse-shape discrimination can give deeper insight into backgrounds resulting from inelastic neutron scattering. A comprehensive characterization of the neutron scintillation-light yield for NE 213A, EJ 305, EJ 331 and EJ 321P was also performed. It employed the simulation-based calibrations to confirm existing light-yield parametrizations for NE 213A and EJ 305, and resulted in light-yield parametrizations for EJ 331 and EJ 321P extracted for the first time from data. In addition to the development of a simulation-based framework for the study of neutron-induced scintillation in organic scintillators, the methods and results presented in this thesis lay the foundation for future source-based neutron-tagging efforts and scintillator-detector research and development.

Key words
liquid organic scintillator, oil, time-of-flight, neutron tagging, light yield, simulation, calibration, NE 213A, EJ 305, EJ 331, EJ 321P, Source Testing Facility, pedagogy

Classification system and/or index terms (if any)

Supplementary bibliographical information	Language English

ISSN and key title	ISBN 978-91-8039-556-4 (print) 978-91-8039-557-1 (pdf)

Recipient's notes	Number of pages 174	Price
	Security classification	

I, the undersigned, being the copyright owner of the abstract of the above-mentioned dissertation, hereby grant to all reference sources the permission to publish and disseminate the abstract of the above-mentioned dissertation.

Signature _____

Date _____2023-02-13_____

Neutron-Induced Scintillation in Organics

by Nicholai Mauritzson

LUND
UNIVERSITY

A doctoral thesis at a university in Sweden takes either the form of a single, cohesive research study (monograph) or a summary of research papers (compilation thesis), which the doctoral student has written alone or together with one or several other author(s).

In the latter case the thesis consists of two parts. An introductory text puts the research work into context and summarizes the main points of the papers. Then, the research publications themselves are reproduced, together with a description of the individual contributions of the authors. The research papers may either have been already published or are manuscripts at various stages (in press, submitted, or in draft).

Faculty of Science, Department of Physics

Camaraderie, adventure, and steel on steel.
The stuff of legend! Right, Boo?
- Minsc

Contents

List of Abbreviations

CAD	Computer-Aided Design
CERN	Conseil Européen pour la Recherche Nucléaire
ESS	European Spallation Source
FD	First-Derivative
FOM	Figure-of-Merit
FWHM	Full-Width-at-Half-Maximum
HH	Half-Height
HV	High Voltage
LG	Long Gate
LY	Light Yield
MS	Monte Carlo
PS	Pulse Shape
PSD	Pulse-Shape Discrimination
PuBe	Plutonium-Beryllium
QDC	Charge-to-Digital Converter
RTD	Rise-Time Discriminiation
SG	Short Gate
SMD	Simulated Maximum Deposition
TOF	Time-of-Flight
TP	Turning-Point
YAP:Ce	Yttrium Aluminum Perovskit:Cerium (Ce^+ doped $YAlO_3$)

List of Figures

List of Tables

List of Publications

This thesis is based on the following publications, referred to by their Roman numerals:

I **The neutron tagging facility at Lund University**

F. Messi, H. Perrey, K. Fissum, M. Akkawi, R. Al Jebali, J.R.M. Annand, P. Bentley, L. Boyd, C.P. Cooper-Jensen, D.D. DiJulio, J. Freita-Ramos, R. Hall-Wilton, A. Huusko, T. Ilves, F. Issa, A. Jalgén, K. Kanaki, E. Karnickis, A. Khaplanov, S. Koufigar, V. Maulerova, G. Mauri, **N. Mauritzson**, W. Pei, F. Piscitelli, E. Rofors, J. Scherzinger, H. Söderhielm, D. Söderström, I. Stefanescu
arXiv:1711.10286 included.   Published in International Atomic Energy Agency, Modern Neutron Detection, IAEA-TECDOC-1935, IAEA, Vienna (2020)

II **GEANT4-based calibration of an organic liquid scintillator**

N. Mauritzson, K.G. Fissum. H. Perrey, J.R.M. Annand, R.J.W. Frost, R. Hall-Wilton, R. Al Jebali, K. Kanaki, V. Maulerova-Subert, F. Messi, E. Rofors
Nuclear Instruments and Methods in Physics Research Section A, Volume 1023, 2022, 165962

III **Technique for the measurement of intrinsic pulse-shape discrimination for organic scintillators using tagged neutrons**
N. Mauritzson, K.G. Fissum, J.R.M. Annand, H. Perrey, R.J.W. Frost, R. Al Jebali, A. Backis, R. Hall-Wilton, K. Kanaki, V. Maulerova-Subert, C. Maurer, F. Messi, E. Rofors
Nuclear Instruments and Methods in Physics Research Section A, Volume 1039, 2022, 167141

IV **Light-yield response of liquid scintillators using $2-6$ MeV tagged neutrons**

N. Mauritzson, K.G. Fissum, J.R.M. Annand, H. Perrey, R.J.W. Frost, R. Al Jebali, A. Backis, R. Hall-Wilton, K. Kanaki, V. Maulerova-Subert, C. Maurer, F. Messi, E. Rofors, J. Scherzinger
Preprint to be sumbmitted to Nuclear Instruments and Methods in Physics Research Section A

All papers are reproduced with permission of their respective publishers.

Publications Not Included in This Thesis

I   **A comparison of untagged gamma-ray and tagged-neutron yields from ^{241}AmBe and ^{238}PuBe sources**
J. Scherzinger, R. Al Jebali, J.R.M. Annand, K.G. Fissum, R. Hall-Wilton, S. Koufigar, **N. Mauritzson**, F. Messia, H. Perrey, E. Rofors
Applied Radiation and Isotopes, 127 2017 98-102

II   **Tagging fast neutrons from a ^{252}Cf fission-fragment source**

J. Scherzinger, R. Al Jebali, J.R.M. Annand, A. Bala, K.G. Fissum, R. Hall-Wiltonb, D. Hamilton, **N. Mauritzson**, F. Messi, H. Perrey, E. Rofors
Applied Radiation and Isotopes, 128 2017 270-274

III   **Response of a Li-glass/multi-anode photomultiplier detector to α-particles from ^{241}Am**
E. Rofors, H. Perrey, R. Al Jebali, J.R.M. Annand, L. Boyd, U. Clemens, S. Desert, R. Engels, K.G. Fissum, H. Frielinghaus, C. Gheorghe, R. Hall-Wilton, S. Jaksch, A. Jalgén, K. Kanaki, G. Kemmerling, V. Maulerova, **N. Mauritzson**, R. Montgomery, J. Scherzinger, B. Seitz
Nuclear Instruments and Methods in Physics Research Section A, 929, 2019, 90-96

IV   **From micro- to macro- neutron sources: The Lund Broad-band Neutron Facility**

H. Perrey, M. Elfman, K. Fissum, R.J.W. Frost, N. De La Rosa, M. Kristensson, P. Kristiansson, **N. Mauritzson**, F. Messi, C. Nilsson, J. Pallon and E. Rofors
E3S Web of Conferences 231, 01005, 2020

V   **Nya metoder gav bättre laborationer**

N. Mauritzson, H. Perrey
Fysikersamfundets, Fysikaktuellt, December, 2020, p13-14

VI   **Response of a Li-glass/multi-anode photomultiplier detector to focused proton and deuteron beams**
E. Rofors, J. Pallon R. Al Jebali, J. R.M. Annand, L. Boyd, U. Clemens, S. Desert, M. Elfman, R. Engels, K.G. Fissum, H. Frielinghaus, R.J.W. Frost, S. Gardner, C. Gheorghe, R. Hall-Wilton, S. Jaksch, A. Jalgén, K. Kanaki, G. Kemmerling, P. Kristiansson, K. Livingston, V. Maulerova, **N. Mauritzson**, R. Montgomery, H. Perrey, T. Richter, J. Scherzinger, B. Seitz, M. Shetty
Nuclear Instruments and Methods in Physics Research Section A, 984, 2020, 164604

VII   **Vanadium-based neutron beam monitor**

V. Maulerova, K. Kanaki, P. M. Kadletz, R. Woracek, T. Wilpert, K. Fissum, A. Laloni, **N. Mauritzson**, F. Issa, R. Hall-Wilton
Physical Review Accelerators and Beams 23, 072901, 2020

VIII   **Response of a Li-glass/multi-anode photomultiplier detector to collimated thermal-neutron beams**
E. Rofors, **N. Mauritzson**, H. Perrey, R. Al Jebali, J.R.M. Annand, L. Boyd, M.J. Christensen, U. Clemens, S. Desert, R. Engels, K.G. Fissum, H. Frielinghaus, C. Gheorghe, R. Hall-Wilton, S. Jaksch, K. Kanaki, S. Kazi, G. Kemmerling, I. Llamas Jansa, V. Maulerova, R. Montgomery, T. Richter, J. Scherzinger, B. Seitz, M. Shetty
Nuclear Instruments and Methods in Physics Research Section A, 999, 2021, 165170

IX   **Simulation of the response of the Solid State Neutron Detector for the European Spallation Source**
L. Boyd, E. Rofors, J.R.M. Annand, K.G. Fissum, R. Hall-Wilton, R. Al Jebali, K. Kanaki, K. Livingston, V. Maulerova, **N. Mauritzson**, R. Montgomery, H. Perrey, B. Seitz
Nuclear Instruments and Methods in Physics Research Section A, 998, 2021, 165174

X   **A Compact Accelerator Driven Neutron Source at the Nuclear-Applications Laboratory, Lund University**
R.J.W. Frost, M. Elfman, K. Fissum, M. Kristensson, P. Kristiansson, **N. Mauritzson**, J. Pallon, H. Perrey, G. Pédehontaa-Hiaa, A. Sjöland, K. Stenström
International Conference on Accelerators for Research and Sustainable Development, Volume-3 Full-Papers, pp. 114-119, 2023

Acknowledgements

Populärvetenskaplig Sammanfattning på Svenska

Neutroner hittar man inuti atomens kärna. Som namnet anger är neutronen en neutral partikel, dvs. den saknar elektrisk laddning. Om man frigör dessa från atomen så har man ett mycket användbart verktyg. Utan elektrisk laddning kan neutronen penetrera djupare in i materia och därför användas för materiella studier för att ge information om den atomära och subatomära världen, till exempel inom fysik, kemi, biologi och medicin. Men samtliga metoder som använder sig av neutroner behöver ett sätt att "se" neutronen. En neutron detektor!

Neutron detektorer finns färdiga att köpa direkt från en tillverkaren men kan också för unika ändamål behöva specialutvecklas. Till exempel på European Spallation Source (ESS) här i Lund så pågår där utveckling av nya och unika neutron detektor system för att kunna uppfylla dom framtida höga kraven när ESS drar igång. Men oberoende vilken väg man väljer krävs det att man skapar sig mycket god förståelse om varje specifik detektor. Frågor man behöver besvara kan inkludera: Är det någon skillnad när en gamma foton eller neutron träffar detektorn? Kan man bestämma energin på neutronerna som detekteras? Hur lång tid tar det att läsa ut en signal från detektorn osv. För att kunna besvara dessa frågor och fler krävs ingående utveckling och studie samt tillgång till en dedikerad forskningsmiljö och utrustning. I Source Testing Facility (STF) på Lunds Universitet finns just en sådan miljö. Här har dussintals detektor prototyper och hundratals studenter strövat igenom sedans dess invigning hösten 2015. Kärnan av STF består av en uppställning för neutron "tagging" som kallas för Akvariet. Här är det möjligt att med hjälp av radioaktiva neutron källor bestämma neutronens energi genom att mäta tiden den flyger över ett bestämt avstånd. Eftersom neutronerna på STF har relativt höga hastigheter (ca 10'000'000 km/h) så behöver man mäta denna tid med mycket små marginaler. Faktiskt så små som 0.000000001 sekunder eller 1 miljarddels sekund!

Men oberoende hur trevligt det än är att sitta på STF, så räcker det inte bara med ett labb och bra utrustning för att kunna karakterisera en neutron detektor. Experimentella metoder för att utforska specifika egenskaper av detektorn behöver utvecklas och beprövas för att slutligen kunna implementeras. Det är just metoderna som ger oss svaren vi är ute efter. Fokuset på denna avhandling har varit att utveckla och implementera just experimentella metoder och främst för en just en typ av neutron detektor. Den så kallade scintillator detektorn. Scintillatorer har använts som partikel detektorer i över 100 år och utvecklingen av nya scintillator material är än idag ett aktivt forskningsområde. Scintillator detektorn fungerar genom att den inkommande neutronen träffar materialet och ge upphov till ljusblixtar. Generellt så blir dessa ljusblixtar stora och skarpa för höga neutron energier och svagare för låga neutron energier. En ljuskänslig sensor omvandlar dessa ljusblixtar till elektriska signaler som kan användas för att studera händelsen.

Metoder som utvecklats i denna avhandling har använt dessa ljusblixtar för att bland annat urskilja neutroner och gamma fotoner i radioaktiva miljöer. Tillsammans med neutron tagging metoden på STF har detta resulterat i fördjupad insikt om scintillator materialets basfunktion. Även metoder baserade på datasimulering har utvecklats från granskningen av dessa ljusblixtar. Man kan använda sig av simuleringar för att säkerställa sina experimentella resultat samt att ge insikt i den bakomliggande fysiken. Simulering är ett mycket kraftfull redskap eftersom det ger dig facit direkt i hand. Detta innehåller detaljerad information om vad som träffade detektorn, när det hände, med vilken energi osv. När man lyckas att återskapa dom experimentella resultaten i sin simulering så har man tillgång till hela detta facit! Denna kopplingen mellan simulering och experimentella resultat har givit upphov till metoder för energibestämning av detekterade partiklar med högre precision samt publicering av första karakteriseringen av nya scintillator material.

Introduction

Neutrons are fundamental to the makeup of matter. They are most often found bound within the atomic nucleus but can be freed through nuclear processes. As free uncharged particles, they can serve as a unique tool for investigating the atomic and subatomic world. Beams of free neutrons are particularly useful. Applications cover a diverse range of scientific fields including (but not limited to):

- as a non-destructive imaging tool [1],

- for the determination of moisture content in soils and other materials [2, 3],

- for the characterization of mixed neutron/gamma-ray fields [4], for example, to derive parameters of the plasma in nuclear-fusion experiments [5],

- to flag neutrino production [6],

- to establish the presence of low-activity radionuclides [7, 8].

Any such application requires a suitable and well-understood method of detecting neutrons. For those cited above, the underlying technology is liquid organic scintillator detectors. Neutrons are fundamentally challenging to detect since they are usually inferred from processes such as scattering or absorption which result in secondary particles. The secondary particles are then detected. Here, the neutron interacts with the scintillator resulting in a brief flash of visible light which is recognized by a light-sensitive sensor.

Scintillator detectors have been around for well over 100 years [9] and the development of new scintillator materials and application-specific detection systems [10] remains an active field of research. Such research and development is largely an iterative process which requires:

- a dedicated environment equipped with the relevant tools, equipment and infrastructure,

- experimental methods which can provide insight into detector properties and responses to different types of radiation,

- analytical and computational methods which can quantify results as well as provide deeper understanding.

This thesis is focused on neutron-detector development including:

- the development of the user facility known as the Source Testing Facility at Lund University,

- the investigation of intrinsic scintillation light-production differences between gamma-rays and neutrons,

- the measurement and parameterization of neutron-induced light yields of different liquid organic scintillator detectors,

- the establishment of a simulation-based gamma-ray and neutron data-analysis toolkit which includes a method for detector calibration.

Figure 1 presents an overview of the relationship between the core components of the thesis project. In total, four peer-reviewed articles were produced. The interdependence, including supporting tools, equipment, methods and results, is illustrated. Paper I provided the fundamental base upon which the other three papers were built. Papers II-IV evolved serially, each building upon the results and methods established in the previous work. This resulted in systematic experimental methods and a well-benchmarked and stable analysis-code framework.
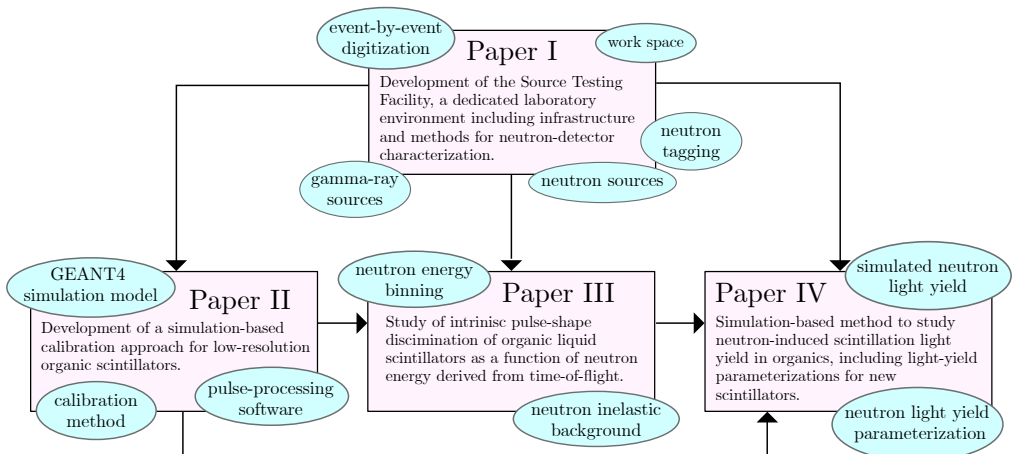
Figure 1: Thesis structure. Arrows indicate the workflow between the projects (boxes). The relevant tools and methods developed for each project (ovals) are also indicated.

Chapter 1

Background and Concepts

1.1   Neutron Interactions with Matter

The interaction of charged particles with matter occurs mainly via charge coupling to atomic electrons via the electromagnetic force. Due to their lack of charge, neutrons instead interact predominately with atomic nuclei via the strong force. The confined nature of nuclei compared to the the extent of the electron cloud and the extremely short range of the strong force[1] results in a low probability for neutron interaction. Interaction mechanisms include (but are not limited to):

- elastic scattering, where the total kinetic energy of the system is conserved so that any energy lost by the neutron is the energy gained by the recoiling nucleus,

- inelastic scattering, where the total kinetic energy is not conserved and may be partially converted into excitation energy of the recoiling nucleus,

- absorption, where the neutron induces a nuclear reaction.

The probability of these interactions depends on the energy of the incident neutron as well as the nuclear structure of the target nucleus. This interaction probability is often referred to as a cross section. In general, the cross section for absorption is largest at lower neutron energies (<0.1 MeV) and depends on the inverse of the time the neutron spends in the vicinity of the nucleus. Depending on the target nucleus, absorption may result in secondary charged-particle emissions or gamma-rays. The elastic scattering cross section becomes substantial in the MeV energy range. The inelastic scattering cross section is significant

---

[1]The range of the electromagnetic force is infinite, while the strong force is limited to $\sim 10^{-15}$ m.

only at higher energies (>0.1 MeV) since the energy of the neutron must be greater than the lowest excited state of the target nucleus. The absolute probabilities for each of these reactions depend upon target-specific properties.

1.2 Neutron Detection

The detection of a charged particle is relatively straightforward since it will directly ionize the detector medium. Neutrons are generally detected indirectly via the production of secondary charged reaction products and/or gamma-rays. The detection of these reaction products can then be used to infer the detection of a neutron. Due to the energy dependence of the neutron interaction, different detection techniques may be employed. In the following discussion, neutron energies are split into two broad categories: slow neutrons ($E_n < 0.5$ eV) and fast neutrons ($E_n > 0.1$ MeV). Neutrons with intermediate energies between 0.5 eV and 0.1 MeV are not discussed. A more detailed review of the neutron-energy definitions including the intermediate energies can be found in Refs. [11, 12].

1.2.1 Slow Neutrons

The detection of slow neutrons is commonly accomplished through absorption reactions which produce secondary charged particles and/or gamma-rays. Gaseous detectors based on ^{3}He are the "gold standard" for thermal-neutron detection ($E_n \approx 25$ meV) since the neutron absorption cross section for ^{3}He is particularly high at this energy. Figure 1.1 shows the cross section for neutron absorption for the isotopes ^{3}He, ^{6}Li and ^{10}B, which are commonly used for slow-neutron detection [13]. The absorption cross section falls as a function of neutron energy, and at above ~0.5 MeV peaks corresponding to specific nuclear-energy levels can be seen. The elastic scattering cross sections for the same isotopes are also shown. These remain relatively constant across the entire neutron-energy range.

The slow-neutron absorption reaction for ^{3}He is:

$$n + {}^3\text{He} \rightarrow {}^3\text{H} + p + \text{Q}(0.764\,\text{MeV}),\qquad(1.1)$$
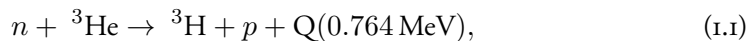
where n is a neutron, ^{3}He is the target, ^{3}H is a triton, p is a proton and Q is the energy released by the reaction. The resulting triton and proton, which share the Q-value as kinetic energy, are easily detected due to their high ionization density. They consequently travel a relatively short distance in the detector medium. The detection of either of these secondary particles can be used to infer the neutron. However, due to the indirect detection method, any information about the energy of the incoming neutron is lost.

4
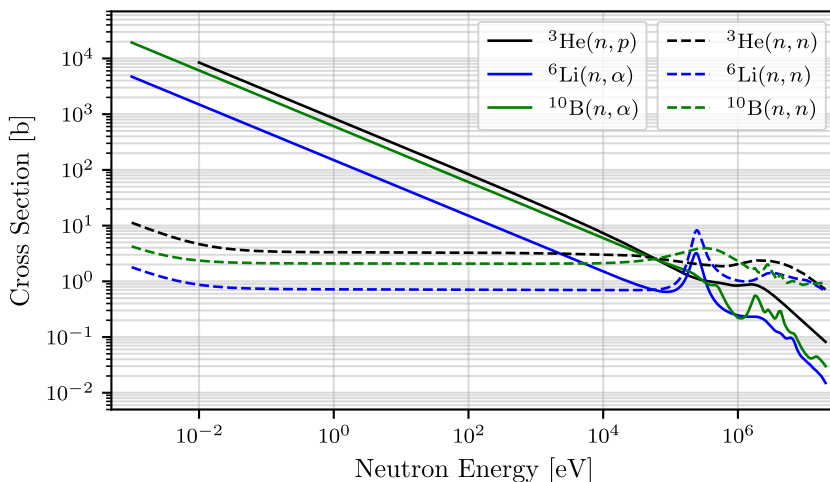
Figure 1.1: Neutron interaction cross sections. Neutron absorption (solid) and elastic scattering (dashed) shown for ^{3}He (black), ^{6}Li (blue) and ^{10}B (green). Data from Ref. [14].

1.2.2 Fast Neutrons

As seen in Figure 1.1, the probability of nuclear absorption drops rapidly with increasing energy. At higher energies ($E_n > 0.5\,\text{MeV}$), the main interaction mechanism becomes neutron-nucleus elastic scattering. Here, the neutron scatters from the nucleus of an atom and transfers a portion (or all) of its kinetic energy. The neutron can then be indirectly detected via the detection of the recoiling nucleus. The maximum possible transferable energy $E_R^{\max}$ of the neutron occurs for backscattering collisions where the scattering angle is 180°:

$$E_R^{\max} = \frac{4A}{(1+A)^2} E_n, \tag{1.2}$$

where A is the atomic mass of the target nucleus and E_n is the incident neutron energy [11]. The maximum transferable energy for a selection of isotopes is shown in Table 1.1.

Table 1.1: Neutron-nucleus elastic scattering. The maximum transferable energy is listed.

Target nucleus	Atomic mass	Maximum energy transfer [%]
^{1}H	1	100
^{2}H	2	88.9
^{3}He	3	75.0
^{4}He	4	64.0
^{12}C	12	28.4
^{16}O	16	22.1

Due to the very similar masses of the neutron and the ^{1}H nucleus (proton), the neutron can potentially transfer all of its energy in a single scattering event. This makes hydrogen-rich detector materials like organic scintillators efficient fast-neutron detectors.

1.2.3 Neutron Time-of-Flight

The energy of a charged particle can be determined from the total energy deposited in a detector volume as long as the particle does not escape. This is often a relatively straight-forward task due to the large stopping power of most materials. A large stopping power results in the rapid energy loss of the incident particle through interactions with the atomic electrons. Determining the energy of a neutron is more complicated, since its detection generally occurs through indirect processes which result in partial energy deposition. A fast neutron will generally require multiple scattering events to stop. The recoiling charged particles resulting from each scatter will each carry some portion of the energy of the incident neutron. The low probability of interaction of a neutron results in a large mean free path. This greatly increases the chance of a neutron escaping the detector volume, resulting in a lower overall detection efficiency.

A common technique used to determine neutron energy is the time-of-flight (TOF) method illustrated in Fig. 1.2.
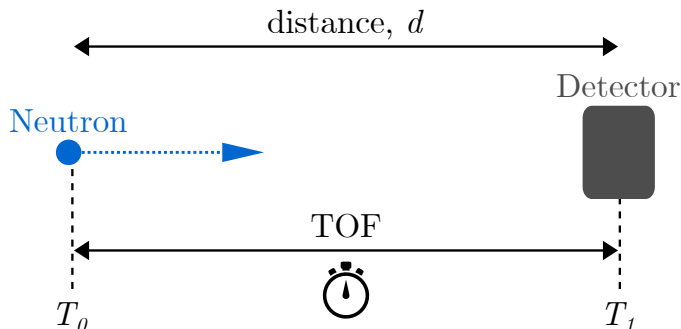
Figure 1.2: Time-of-flíght principle. The time it takes a neutron to traverse a known distance d is measured.

The time it takes a neutron to traverse a given distance (d) is measured using a start (T_0) and stop (T_1) time signal, where $T_1 - T_0 = $ TOF. The speed and thus energy of the neutron can be determined using:

$$E_n = \frac{1}{2} m_n \frac{d^2}{\text{TOF}^2},$$

(1.3)

where E_n is the neutron kinetic energy, m_n the mass of the neutron and d is the distance traveled[2]. A complication associated with this technique is the requirement of a suitable timing reference (T_0). Given an appropriate experimental setup, the TOF technique can in principle be used to measure any neutron energy.

1.3 Photon Interactions with Matter

The mechanisms which describe the photon-matter interaction are:

- the photoelectric effect,

- scattering such as coherent scattering and Compton scattering,

- pair production.

These mechanisms have cross sections which depend upon the energy of the photon and the Z-value of the material, shown in Fig. 1.3 for ^{12}C.

In general, the interaction probability decreases as the photon energy increases. In the case of the photoelectric effect, the photon is absorbed by a bound atomic electron, which is freed. The energy of the incident photon (less the electron-binding energy) is carried away by the freed electron as kinetic energy. The cross section for the photoelectric effect dominates at lower photon energies and decreases as the energy increases. For coherent scattering, a photon interacts with an atomic electron resulting in angular deflection but no transfer of energy. For Compton scattering, the photon interacts with an atomic electron and transfers a portion of its energy, again freeing the electron. This results in an angular deflection of the incident photon and a reduction of its energy. The difference in energy (less the electron-binding energy) is carried away by the recoiling electron as kinetic energy. The photon energy after scattering E'_γ is given by:

---

[2]Relativistic energy corrections are negligible below 10 MeV.

$$E'_\gamma = \frac{E_\gamma}{1 + \frac{E_\gamma}{m_e c^2}(1 - \cos\theta)}, \tag{1.4}$$

where E_γ is the incoming photon energy, $m_e c^2$ is the electron rest mass energy (0.511 MeV) and θ is the photon-scattering angle with respect to the incoming photon direction [11]. The maximum energy transfer $E_{\text{CE}}^{\max}$ to the recoiling electron occurs when the scattering angle of the gamma-ray is 180°, corresponding to backscattering. The maximum electron recoil-energy transfer via Compton scattering[3] is given by:

$$E_{\text{CE}}^{\max} = \frac{2E_\gamma^2}{m_e c^2 + 2E_\gamma}. \tag{1.5}$$

In case of pair production, a photon with an energy exceeding at least double the rest-mass energy of an electron is absorbed and converted into an electron/positron pair. The remaining energy is shared equally between the electron and positron as kinetic energy. Due to energy and momentum conservation, this interaction can only occur in the vicinity of the Coulomb field of a nucleus or, at higher energies, within the Coulomb field of an electron. The cross section for pair production dominates at higher photon energies.
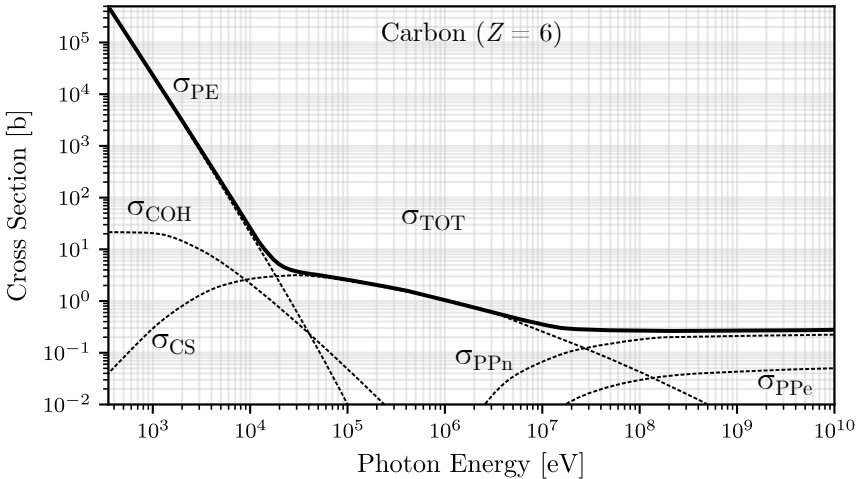
Figure 1.3: Photon interaction probability for ^{12}C. Cross sections (dashed lines) are shown for the photoelectric effect σ_{PE}, coherent scattering σ_{COH}, Compton scattering σ_{CS} and pair production in the vicinity of a nucleus σ_{PPn} or in the vicinity of an electron σ_{PPe}. The total cross section σ_{TOT} is given by the solid line. Data from Ref. [15].

---

[3]For this work, Compton scattering was an essential mechanism which allowed for the energy calibration of low Z-value detector materials.

1.4 Scintillation Detectors

Scintillation, which governs the conversion of energy to light, is one of many ways in which particles can be detected. Scintillation-based detectors are commonly used in nuclear physics, particle physics, homeland security and medicine [16] (to name a few). Following the excitation of the scintillator by ionizing radiation, de-excitation results in the emission of scintillation photons in the visible spectrum. The scintillation-light intensity is often proportional to the energy deposited in the scintillator. Using a light-sensitive sensor, the scintillation can be converted into an electrical signal.

There are two principle types of scintillation emissions, each categorized by the time scale of their de-excitation. Emissions with fast decay times ($\sim$1 ns) are referred to as fluorescence while those with slower decay times ($\geq$1 μs) are referred to as phosphorescence. Figure 1.4 shows the total light output of a multiple component scintillation event together with the different decay times of the underlying components.
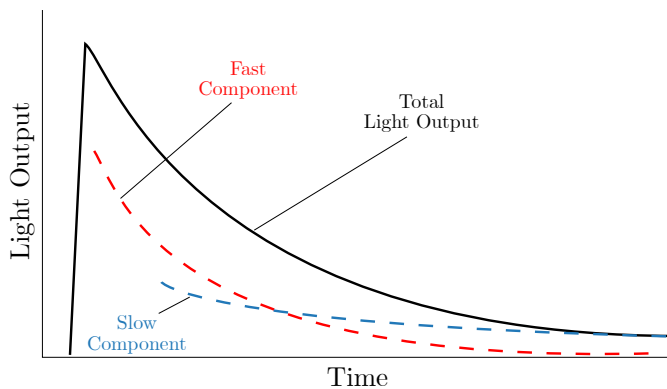
Figure 1.4: Scintillation light components. Total light output (solid line) shown together with the fast (red dashed lines) and slow (blue dashed lines) components. Figure modified from Ref. [9].

Further details on different types of scintillators can be found in Refs. [9, 11].

1.4.1 Inorganic Scintillators

Inorganic scintillators employ a regular crystal lattice to enable the scintillation process. An inorganic scintillator is often doped with a small amount of an impurity known as an activator which together with the crystal structure determines the energy-level structure. Figure 1.5 shows a schematic of a typical inorganic scintillator energy-level diagram. The conduction band consists of electrons which are able to easily migrate across the crystal lattice, while the valence band is formed by electrons bound locally. Incident ionizing

radiation promotes electrons from the valence band to the conduction band. The doped activator states allow the conduction-band electrons to de-excite to the activator states, and across the activator band gap to the activator ground state. A scintillation photon is emitted in the process. Without the activator states, de-excitation from the conduction band to the valence band across the crystal band gap would result in scintillation photons which would be self absorbed by the crystal.
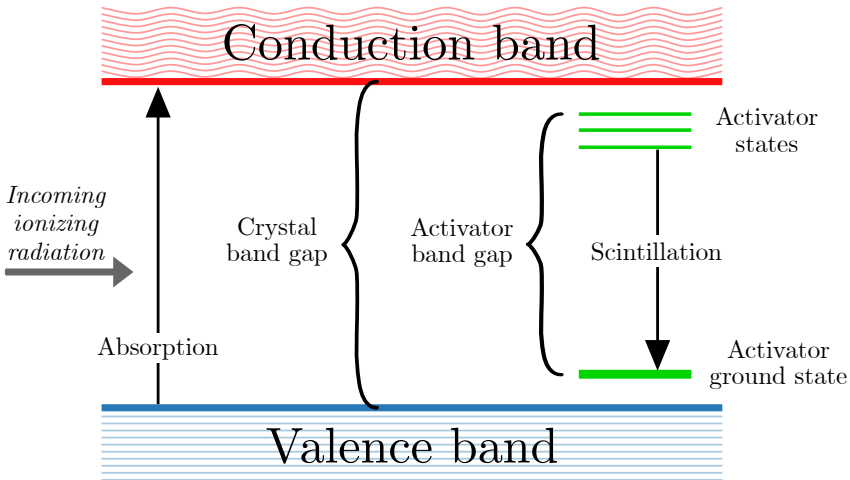
Figure 1.5: Electron energy-band structure of an inorganic scintillator. The conduction band (red) and the valence band (blue) dominate. The horizontal green lines represent activator states. Electron de-excitation can give rise to the emission of scintillation light. Black arrows indicate excitation or de-excitation between states. Figure modified from Ref. [11].

By varying the dopant type and concentration, the energy of the scintillation photons can be tuned, while ensuring the material is transparent to its own radiation. Since the production of inorganic scintillators often requires a crystal lattice to be artificially produced, the size and geometry of the scintillator can be a limiting factor. Alternatively, powder-based inorganic scintillators can be suspended and cast in an epoxy resin [17]. Inorganic scintillators generally have a large Z-value material composition, and exhibit a high light output and linear energy response. This makes them suitable for photon spectroscopy [11, 18].

1.4.2   Organic Scintillators

Organic scintillators generally consist of hydrogen and carbon. This low Z composition makes organic scintillators unsuitable for spectroscopy but useful for fast-neutron detection due to the increased scattering cross section and large maximum possible energy transfer. Aromatic hydrocarbon molecules have a closed valence electron loop shared across the molecule. The valence electrons exhibit what is known as π-electron energy levels consisting of singlet and triplet states, as illustrated in Fig. 1.6.
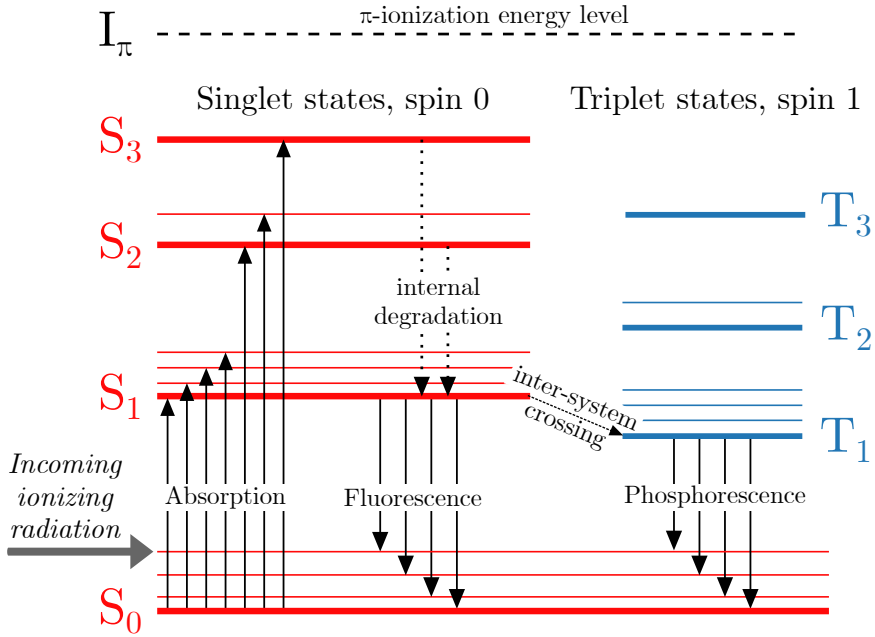
Figure 1.6: Energy-level diagram of the π-electron levels of an organic scintillator. The singlet states (red) and triplet states (blue) are shown separated for clarity. The thick horizontal lines indicate primary energy levels and the thinner lines indicate vibrational energy levels. The solid black arrows indicate excitation or de-excitation between states and the dotted arrows indicate non-radiative transitions between states. Figure modified from Ref. [19].

When ionizing radiation excites the electron levels, the resulting $S_3 \rightarrow S_2$ and $S_2 \rightarrow S_1$ transitions de-excite in a radiationless fashion through internal degradation on a picosecond time scale. Scintillation is produced by $S_1 \rightarrow S_0$ and $T_1 \rightarrow S_0$ transitions. There are several processes which determine the intensity and time structure of the scintillation light:

- Absorption of energy not resulting in ionization places the π-electrons into excited singlet states ultimately resulting in the radiative transition $S_1 \rightarrow S_0$, which produces prompt fluorescent scintillation light.

- Inter-system crossing allows electrons from the S_1 state to populate the T_1 state. However, the de-excitation $T_1 \rightarrow S_0$ is largely forbidden due to spin conservation, resulting in much longer decay times for the resulting phosphorescent scintillation light.

- While in the T_1 state, electrons can migrate back into the S_1 state through thermal excitations via the the close-lying vibrational energy levels. From here, the radiative transition $S_1 \rightarrow S_0$ occurs which results in a delayed fluorescent scintillation light on a ~ 100 ns time scale.

- Two T_1-excited molecules may combine and through Triplet-Triplet Annihilation [20], one may end up in the S_0-state while the other ends up in an excited S^*-state. The radiative transition $S_1 \rightarrow S_0$ results in delayed fluorescent scintillation light as above.

- Singlet and triplet states may also be populated through the ionization of the π-electrons (past the I_π-level) and subsequent recombination. About 12% of recombining π-electrons return to singlet states, while $\sim$75% return to triplet states [21]. At this point, the previously discussed processes take over.

Figure 1.7 highlights the processes responsible for prompt and delayed fluorescent and phosphorescent scintillation-light emissions.
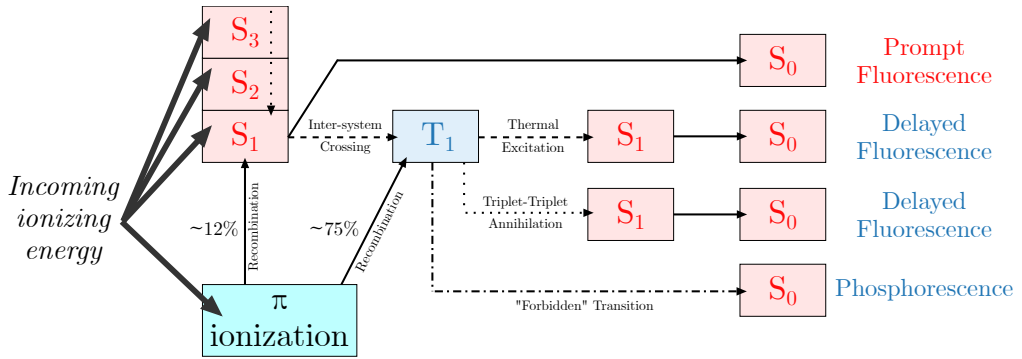
Figure 1.7: Overview of organic-scintillation processes. The interplay between the different scintillation mechanisms responsible for prompt and delayed fluorescent and phosphorescent light emissions are highlighted.

For organic scintillators, in an ideal case, the light output per unit path length dL/dx is given as a function of the ionization density of the incoming particle dE/dx [11] as

$$\frac{dL}{dx} = S\frac{dE}{dx}, \tag{1.6}$$

where S is the scintillation efficiency. S determines the amount of energy which is converted into light and can vary continuously from 0 (no light conversion) to 1 (complete light conversion). A typical organic scintillation efficiency is less than 10% [22]. The scintillation efficiency is affected by self absorption, in which scintillation light is reabsorbed by the scintillator. The difference between the possible absorption energies and the emission energies is known as the Stokes shift [11], and is ideally as large as possible. For organics, the favorable absorptions are larger than the emitted scintillation-photon energies which limits self-absorption.

With increasing ionization density, the light output becomes less linear due to heat and vibrational energy transfer between excited scintillator molecules. This removes energy from

the normal light-production mechanisms and reduces the total light output of the scintillator. Known as quenching, it was first explained by Birks [23], who postulated that it was caused by temporary damage to the scintillator molecules due to ionization along the particle track. To better represent the experimental observation of non-linear light yield at higher dE/dx, Eq. 1.6 may be rewritten as

$$\frac{dL}{dx} = S\frac{\frac{dE}{dx}}{1 + kB\frac{dE}{dx}},$$ (1.7)

where kB is the fractional quenching value known as the Birks parameter. This relation is only relevant for high values of dE/dx resulting from protons and heavy ions. Electrons have a relatively small dE/dx even at higher energies, resulting in the linear dependence previously discussed. Generally, quenching is less pronounced in gaseous scintillator detectors due to their reduced density and more pronounced in liquid scintillator detectors due to their higher density.

The ionization of molecular electrons other than π-electrons destroys the scintillator molecule resulting in permanent damage. This will lead to a permanent reduction in S. Any scintillator detector thus has a limited life time which is directly dependent on the intensity of irradiation.

1.4.3   Pulse-Shape Discrimination

For certain scintillators, the relative amounts of prompt fluorescence and delayed fluorescence produced are dependent on the dE/dx of the ionizing particle. This directly affects the time structure, or pulse shape (PS) of the scintillation light[4]. In organic scintillators, higher dE/dx ionization tracks populate more of the T^* long-decay states compared to the S^*-states. Furthermore, the effect of quenching is greater, which works to suppress the prompt-fluorescent intensity. Both these effects combine to modify the resulting scintillation PS by increasing the relative proportion of slow-scintillation components in the signal. Since dE/dx is directly dependent on the type of particle causing the ionization, PS discrimination (PSD) allows for the identification of particle species. Figure 1.8 shows a typical time-dependent light-pulse comparison between signals with varying amounts of slow-scintillation components.

---

[4]Certain inorganic scintillators also exhibit this effect, see Refs. [24, 25].
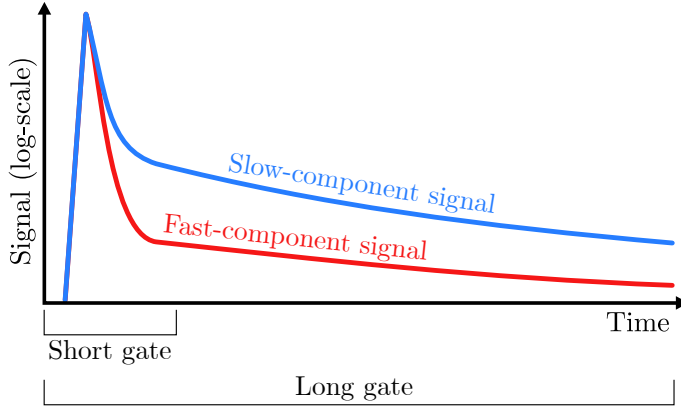
Figure 1.8: Pulse-shape comparison in a scintillator with PSD capabilities. A predominately slow-component signal (blue) and a predominately fast-component signal (red) along with two integration gate lengths (short gate and long gate) are shown. Figure from Ref. [26].

A PSD evaluation of a given signal can be performed by examining the signal over different time periods. For example, the quantity PS may be defined as:

$$\text{PS} = \frac{\text{Long gate integral} - \text{Short gate integral}}{\text{Long gate integral}}. \tag{1.8}$$

This normalization results in higher PS values for predominately slow-component signals and lower PS values for predominately fast-component signals. Other PSD techniques such as rise-time discrimination (RTD) [27, 28] have been proposed. RTD compares the time it takes for the pulse to rise to the peak amplitude or fractions thereof.

1.4.4   Scintillators in This Work

For this work, the liquid organic scintillators NE 213A [29], EJ 305 [30], EJ 331 [31] and EJ 321P [32] were investigated. Properties of these scintillators are presented in Table 1.2.

Table 1.2: Selected scintillator properties.

Scintillator	NE 213A	EJ 305	EJ 331	EJ 321P
Density [g/cm^3]	0.874	0.893	0.89	0.85
Light Yield (% Anthracene)	75	80	68	21
Peak emission wavelength [nm]	420	425	424	425
Flash point [°C]	54	45	44	115
H/C ratio	~1.21	~1.33	~1.32	~2.06
Gadolinium content [% w/w]	-	-	1.5	-

NE 213A is a pseudocumene-based variant of the widely used NE 213 [33] developed for fast-neutron detection. It exhibits excellent neutron/gamma-ray PSD. EJ 305 has very large scintillation light yield and very good optical transmission properties. It also demonstrates some PSD properties. EJ 331 is a Gadolinium-doped scintillator (here, 1.5% by weight) which (in addition to fast neutrons) makes it sensitive to thermal neutrons through the absorption reaction $^{nat}\text{Gd}(n, \gamma)$. EJ 321P is a mineral oil-based scintillator (non-organic) with a relatively low light output but with a high $^{1}\text{H}/^{12}\text{C}$ ratio, making it more sensitive to fast neutrons. The high flash point makes it suitable for use in large detector volumes.

Chapter 2

Apparatus and Setup

2.1 Experimental Facility and Setup

2.1.1 A Laboratory for Neutron Tagging

The majority of the work presented in this thesis was carried out at the Source Testing Facility (STF) [34] of the Nuclear Physics Division at Lund University. The facility was developed in conjunction with the Detector Group of the European Spallation Source (ESS). The STF is a user facility which provides all the equipment, tools and infrastructure necessary for the development, characterization and commissioning of detector systems [35, 36, 37, 38, 39, 40, 41] and shielding materials [42]. A large number of neutron and gamma-ray sources are available. A neutron-tagging setup which produces beams of polyenergetic neutrons is a critical, perhaps even unique, laboratory component. The facility has routinely hosted neutron TOF labs for hundreds of students as well as Bachelor, Master and PhD projects [26, 43, 44, 45, 46].

Figure 2.1 shows a 3D model of the STF, highlighting the major elements of the facility. The interlocked area is where the majority of the irradiations were performed. It hosts the neutron sources and is located behind a lockable gate. Signal, high voltage, network and gas lines are patched through to the interlocked area from the outside DAQ and IT areas. Designated work areas exist for the dismantling and modification of detector prototypes as needed.

Figure 2.2 shows the STF before and after its initial development starting in the spring of 2015 and ending with the inauguration in the autumn of 2015. The author played a key role in the development of the facility.
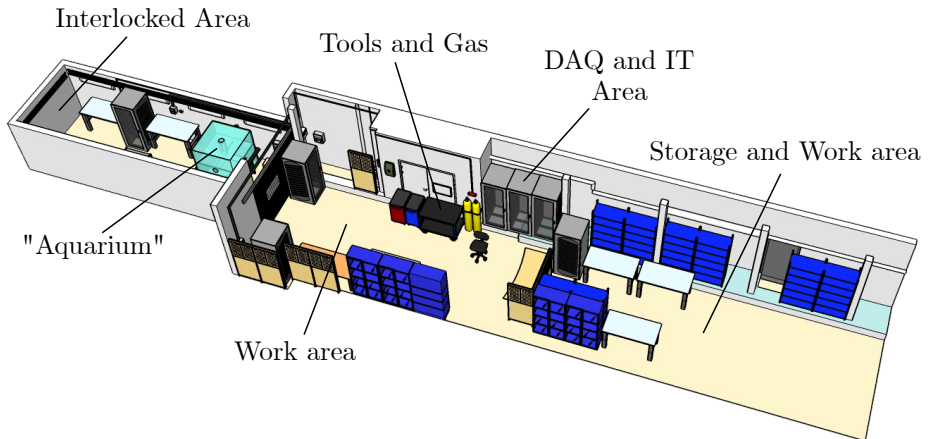
Figure 2.1: 3D model of the Source Testing Facility. Workzones are labeled.
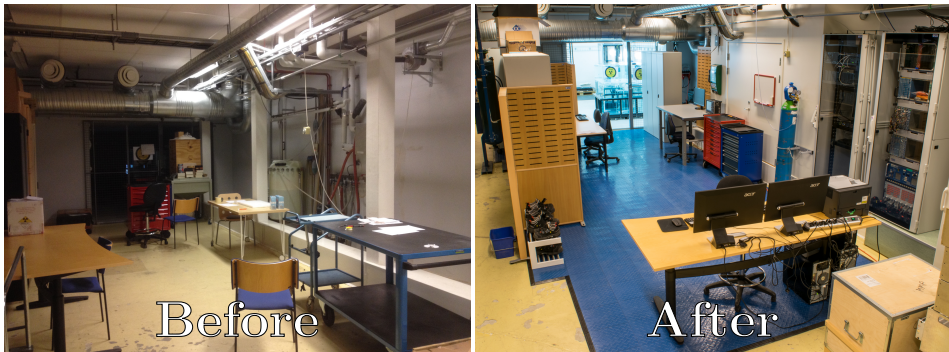
Figure 2.2: The Source Testing Facility development. Pictures taken in the spring (left) and autumn (right) of 2015.

2.1.2 Experimental Setup

Inside the STF interlocked area, a neutron source was housed inside a $1.4 \times 1.4 \times 1.4 \, \text{m}^3$ poly-methyl-methacrylate (PMMA) cube. Filled with de-ionized water, this cube is referred to as the Aquarium. Figure 2.3 shows a CAD model of the Aquarium with the placement of a neutron detector in front of one of the cylindrical beam ports. There are four of these beam ports which provide a direct line of sight between a neutron source (when not in its parked position) and the outside world. A more detailed explanation of the Aquarium design can be found in Ref. [45].
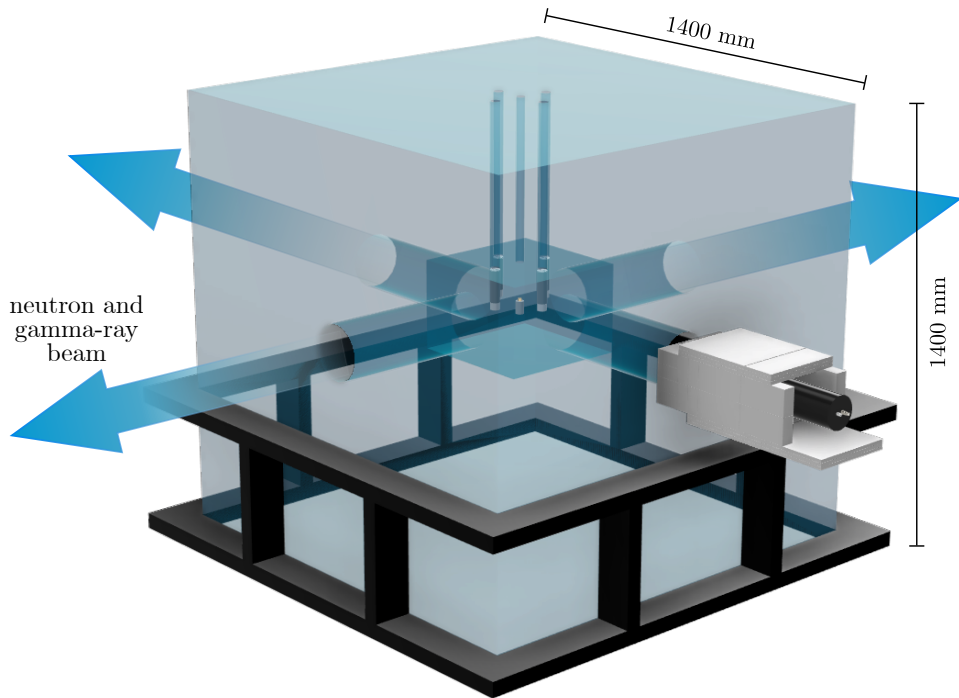
Figure 2.3: 3D model of the experimental setup. The Aquarium (blue) is shown along with the steel support structure (black). Detectors may be placed in front of each beam port.

2.2 Radioactive Sources

2.2.1 Actinide/Beryllium Neutron Sources

Since the discovery of the neutron by Chadwick in 1932 [47], actinide/beryllium-based neutron sources have been widely used in research. The neutron-producing reaction is based on the α-decay of the actinide and the subsequent α-absorption by a ^{9}Be isotope, resulting in ^{12}C and a free neutron according to

$$\alpha + {}^9\text{Be} \rightarrow {}^{12}\text{C}^{(*)} + n. \tag{2.1}$$
$$\hookrightarrow {}^{12}\text{C} + \gamma(4.44\,\text{MeV})$$
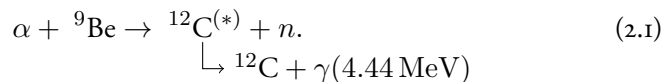
The recoiling ^{12}C nucleus can be produced in its first excited state (4.44 MeV) with a ~55% probability [48]. If so, it will promptly de-excite with the emission of a 4.44 MeV gamma-ray. The maximum possible Q-value for the reaction is given by the rest-mass difference of the reactants and products as:

$$Q = m_{^9\mathrm{Be}} + m_\alpha - m_n - m_{^{12}\mathrm{C}} \approx 5.7\,\mathrm{MeV}. \tag{2.2}$$

In the case of ^{238}Pu, $\sim$71% of the time the maximum emitted alpha energy is $\sim$5.5 MeV [49], resulting in a maximum neutron kinetic energy of $\sim$11.2 MeV. Figure 2.4 shows a typical PuBe fast-neutron energy spectrum calculated by Kozlov *et al.* [50].
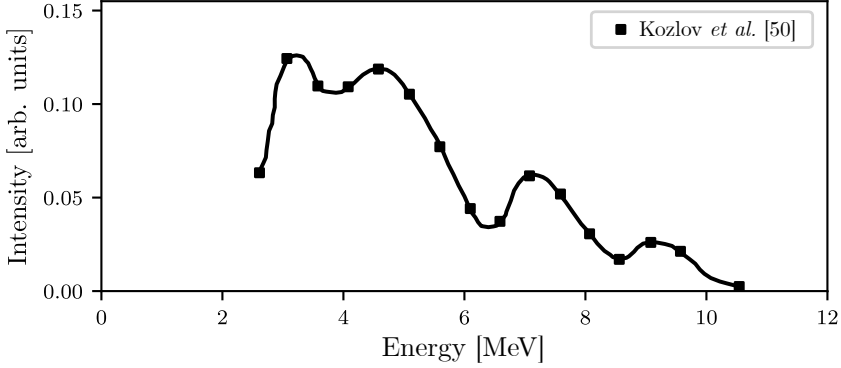
Figure 2.4: PuBe fast-neutron energy spectrum. Full energy spectrum corresponding to the $\sim$11.2 MeV Q-value. Threshold set to 2 MeV.

2.2.2 Gamma-ray Sources

The gamma-ray sources used for the energy calibration of the detectors employed in this thesis is presented in Table 2.1. Compton scattering is the main interaction mechanism due to the relatively low Z-value compositions of the liquid organic scintillators.

Table 2.1: Gamma-ray sources. E_γ refers to the gamma-ray energy while $E_{\mathrm{CE}}^{\mathrm{max}}$ refers to the maximum energy of the Compton electron. "Single" refers to sources where a single gamma-ray emission was considered, while "double" refers to sources where two different gamma-rays were considered.

Source	E_γ [MeV]	E_{CE} [MeV$_{ee}$]	Type
^{22}Na	0.51	0.34	double
^{137}Cs	0.66	0.48	single
^{60}Co	1.17	0.96	double
^{22}Na	1.28	1.06	double
^{60}Co	1.33	1.12	double
^{232}Th	2.62	2.38	single
AmBe	4.44	4.20	single

2.3 Photomultiplier Tubes and Detectors

2.3.1 Photomultiplier Tubes

A photomultiplier tube (PMT) is a photosensitive device which converts scintillation light into an electric signal. Figure 2.5 shows a schematic of a PMT coupled to a scintillator material. Incoming ionizing radiation produces scintillation photons. These photons are converted into electrons at the photocathode of the PMT via the photoelectric effect. The typical electron conversion efficiency (quantum efficiency) is 20-30% depending on the wavelength of the scintillation photons. The inside of the PMT is vacuum tight. Through an applied voltage, electric fields guide the electrons to the first dynode. PMTs are very sensitive to external magnetic fields, as the initial photoelectrons can easily be deflected. To prevent this, a PMT is normally enclosed in a material with a very high magnetic permeability, known as a μ-metal shield. The kinetic energy of the photoelectron striking the first dynode frees more electrons, and the electric field accelerates these electrons from one dynode to the next. This amplifies the electric current at each subsequent dynode. Typical electron amplifications of $\sim 10^7$ result at the final dynode known as the anode. The amplitude and total charge of the current pulse at the anode is generally proportional to the amount of light produced in the scintillator.
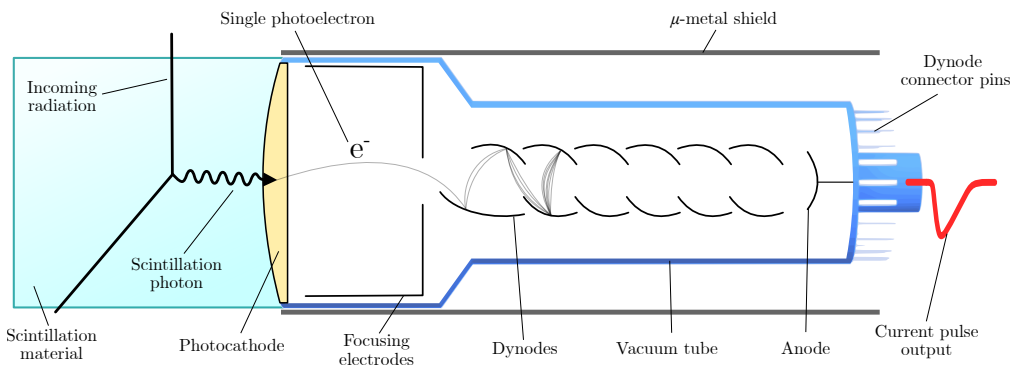
Figure 2.5: Schematic overview of a scintillator and PMT assembly. Incoming ionizing radiation produces scintillation photons which are converted into photoelectrons at the photocathode. The photoelectrons are amplified through the dynode chain to produce a current pulse at the anode.

Optical coupling between the PMT and the scintillator may be improved with optical grease. Optical grease can increase the scintillation light transmission by bridging any air gaps caused by irregular surfaces. However, aging of the grease will degrade the light transmission over time and regular maintenance may be require to maintain the signal strength. For this work, dry-fitted PMTs with no optical grease were employed to ensure the reproducibility of the results.

2.3.2 Detectors

Figure 2.6 shows a 1 in. inorganic YAP:Ce and PMT assembly together with a 3 in. liquid organic scintillator and PMT assembly. These detectors were employed extensively in this thesis.
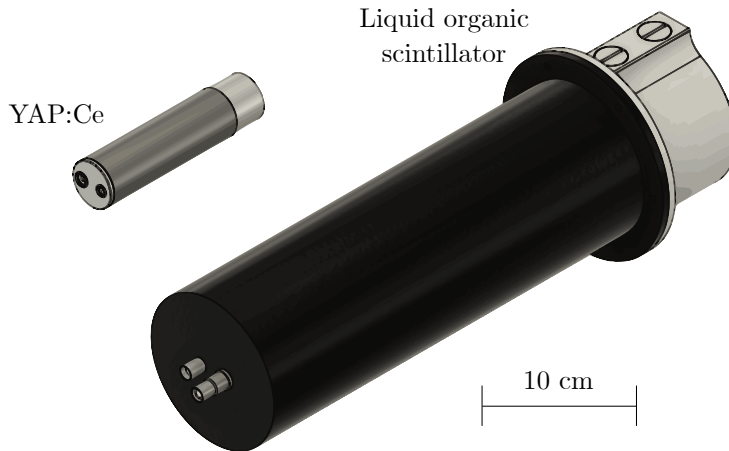
Figure 2.6: CAD model of the detectors (to scale). Left: YAP:Ce. Right: liquid organic scintillator.

The YAP:Ce inorganic scintillator [51] was comprised of a 1 in. $\times$ 1 in. (diameter $\times$ length) cylindrical crystal coupled to a 1 in. Hamamatsu Type R1924 PMT [52] provided by Scionix [53]. The gain of the YAP:Ce detectors was set using a ^{22}Na source with the high voltage fixed at about -750 V. As described earlier, inorganic scintillators like the YAP:Ce have a good gamma-ray sensitivity and furthermore, are largely insensitive to neutrons of all energies [54]. The YAP:Ce detectors were used to detect the 4.44 MeV gamma-rays from the PuBe source and provide a timing reference for neutron TOF measurements.

A more detailed view of the liquid organic scintillator detector components can be seen in Fig. 2.7. The cylindrical aluminum cup had a 3 mm wall thickness and an inner dimension of 94 mm $\times$ 62 mm (diameter $\times$ length) which resulted in a volume of $\sim$430 cm^3. The inside surface of the aluminum was painted with TiO$_2$-based reflective coating (EJ 520 [55]). This coating is specifically intended for use in contact with liquid organic scintillators, including those based on stronger solvents like xylene and toluene. A 93 mm $\times$ 5 mm (diameter $\times$ thickness) borosilicate-glass optical window [56] was glued into place on the cup using Araldite 2000+ [57] two-part epoxy. Once the cup had been filled with a scintillator, the entrance and exhaust ports were sealed with screws and Viton O-rings [58]. The completed cell was dry fitted to a 72.5 mm $\times$ 57 mm (diameter $\times$ length) PMMA UVT [59] light guide which was also painted with a TiO$_2$-based reflective coating (EJ 510 [60]). A 3 in. diameter Electron Tubes type 9821KB PMT [61] was dry fitted to the light guide.

The entire assembly was housed inside an enclosure, which included a μ-metal magnetic shield and a spring-loaded connector/base assembly. This held the PMT, light guide and scintillator cell together. The typical operating voltage was about $-2\,\mathrm{kV}$, comparable to previous investigations of similar detectors [54, 62, 63, 64].
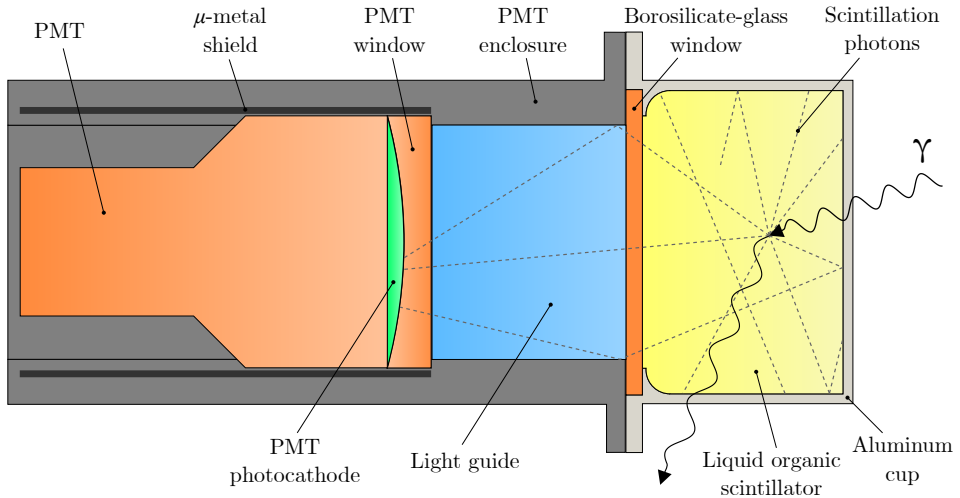
Figure 2.7: Detector assembly schematic. A typical interaction results in the emission of scintillation light, some of which reaches the photocathode.

Figure 2.8 shows a cross-sectional view of a typical neutron-detector setup. In this case, a liquid organic scintillator detector with the front face centered vertically on the beam port at 925 mm from the center of the PuBe neutron source is shown. The front of the Pb shield was 160 mm thick[1]. The remainder of the shielding was 30 mm thick. A mixed radiation field of neutrons and gamma-rays passed through the 500 mm long beam port of the Aquarium. The background in the Pb enclosure was measured without the aperture using a 1.5 in. LaBr$_3$:Ce gamma-ray detector to be less than 1 Hz, with the PuBe source in its parked positions out of line-of-sight of the detector.

This experimental setup facilitated TOF measurements, while the gamma-ray energy calibrations were performed in a more radiologically "quiet" part of the experimental hall away from the Pube source.

---

[1]It included a $\sim$10 × 10 mm^2 aperture to allow for a very small number of source-related gamma-rays to pass through in data-taking mode.
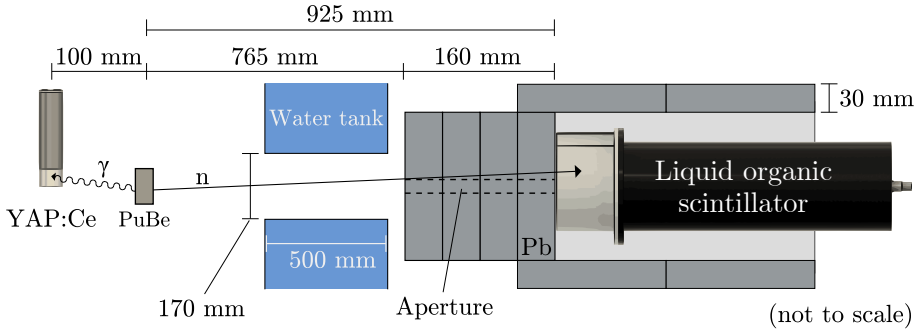
Figure 2.8: Overview of a typical experimental setup (not to scale). The distances between the source, YAP:Ce and liquid organic scintillator detectors are shown along with the dimensions of the Aquarium aperture. The thickness of the Pb shielding is also detailed.

2.4 Digital Pulse Processing and Time-of-Flight

2.4.1 Digital Pulse Processing

Figure 2.9 shows a schematic of the experimental setup and the pulse processing logic chain along with the digitized signal waveform of a typical detector pulse. Processing was performed using a CAEN VX1751 Waveform Digitizer [65] which samples analog pulses with a 1 GHz sampling rate, a bandwidth of 500 Mhz across a $1\,\mu s$ window and a 1 V peak-to-peak (Vpp) dynamic input range. This results in 1000 samples per event. Due to the 1 Vpp dynamic input range, the signal from the liquid organic scintillator detectors needed to be attenuated[2] to capture the full amplitude of the measured irradiation. A CAEN type N858 variable attenuator [66] was used to equalize the signal amplitudes from each of the scintillators passed to the digitizer, see Table 2.2.

Table 2.2: Attenuation. Attenuators were used to equalize the signal amplitudes.

Scintillator	NE 213A	EJ 305	EJ 331	EJ 321P
Attenuation factor [dB]	12	16	15	6
Attenuation factor	3.98	6.31	5.62	2.00

The liquid organic scintillator signal (ch1) was used to trigger the acquisition for all digitizer channels via a falling-edge threshold set to $-25\,mV$. The digitizer initially sampled the waveform into a buffer which allowed the values prior to the falling-edge threshold to be recorded. The event-timing marker which determined the location of the start of the pulse was derived using an interpolating zero-crossover method [11]. This was necessary to remove the time-walk associated with the falling-edge threshold. The zero-crossover method works

---

[2] The signals from the YAP:Ce detectors did not require any attenuation.

by splitting the incoming pulse into two identical pulses. One pulse was inverted while the other was delayed ($\sim$7 ns). After which, both were summed, resulting in a bipolar pulse. The zero-crossing point of the bipolar pulse was used to determine the event-timing marker. The baseline was determined by averaging the amplitude of the first 20 samples (20 ns), with this constant value then being subtracted from each sample comprising the digitized pulse. A numerical integration was performed starting 25 samples before the event-timing marker and extending 60 ns or 500 ns, resulting in short-gate (SG) and long-gate (LG) current integrals. These values, often referred to as QDC (charge-to-digital converter) values, represent the charge in the signal (proportional to the energy deposited by the event), which is histogrammed. The relative timing between the liquid organic scintillator (ch1) and YAP:Ce detectors (ch2 − 5) was determined by taking the difference between the event-timing markers of the incoming pulses event-by-event. This resulted in four independent TOF measurements, one for each YAP:Ce detector. Data from each of the four YAP:Ce measurements, once calibrated, were combined.
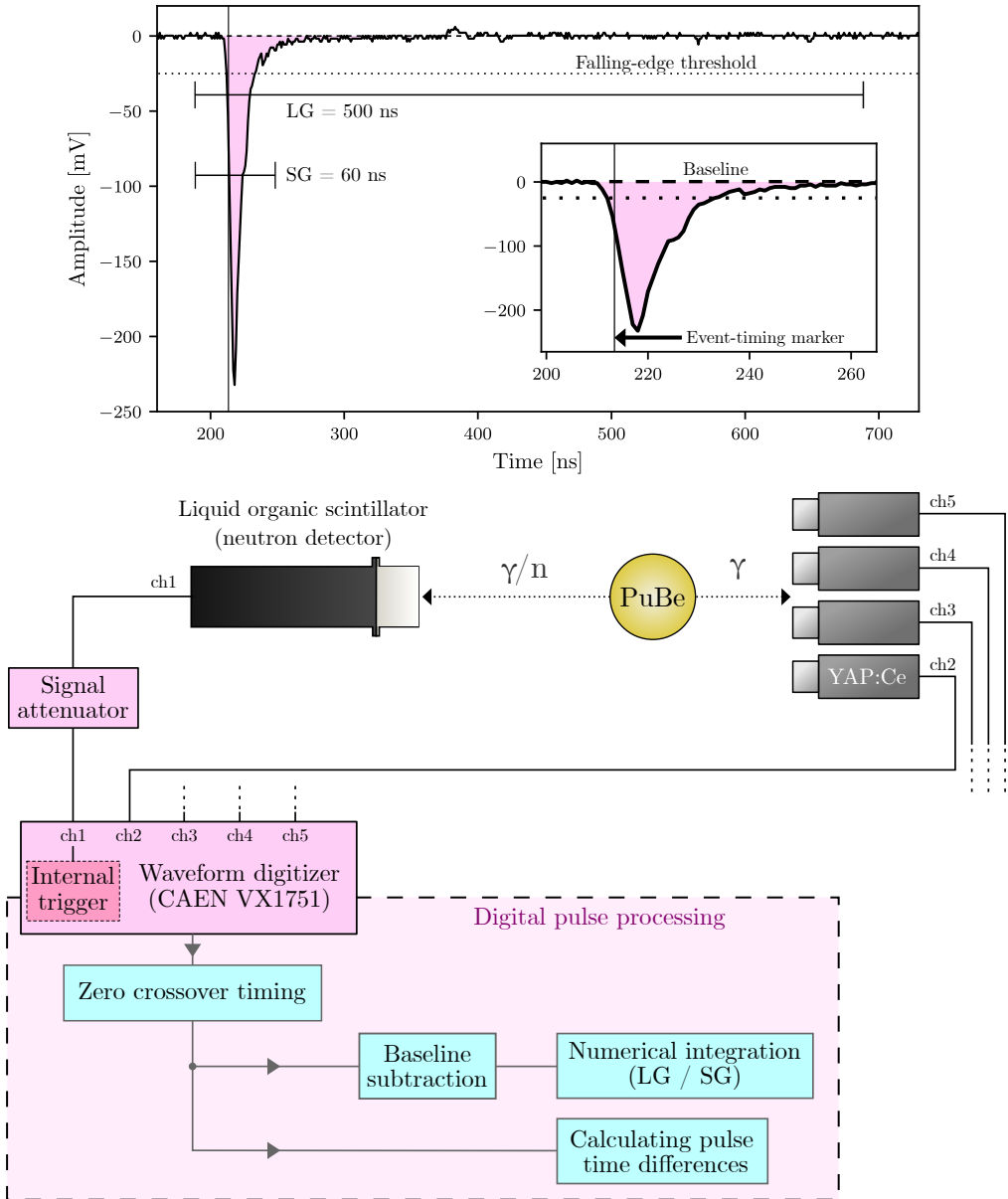
Figure 2.9: Digital pulse processing schematic. Top: Typical digitized signal waveform. The falling-edge threshold is shown along with baseline, event-timing marker, short-gate (SG) and long-gate (LG) integration windows. Bottom: The experimental setup including the PuBe sopurce, YAP:Ce detectors, liquid organic scintillator detector and attenuation module. The digitizer and digital pulse processing logic chain (dashed box) is also shown.

2.4.2 Time-of-Flight

Neutron tagging and thus TOF determination was made possible due to the previously discussed correlated emission of both a neutron and a gamma-ray from the PuBe source. There are three main classes of TOF events-of-interest:

- correlated neutron/gamma-ray events: a fast neutron is detected in the liquid organic scintillator detector and a corresponding 4.44 MeV gamma-ray is detected in a YAP:Ce detector. These events are also known as tagged neutrons.

- correlated gamma-ray/gamma-ray events: a low-energy cascade gamma-ray from the actinide is detected in the liquid organic scintillator detector and a correlated 4.44 MeV gamma-ray is detected in a YAP:Ce detector[3]. These events are also known as gamma-flash events.

- uncorrelated events: a neutron is detected in the liquid organic scintillator detector and a uncorrelated gamma-ray is detected in the YAP:Ce detector (for example), resulting in an arbitrary time difference[4]. These events are also knows as random events.

Figure 2.10 shows a typical histogram of the pulse-time differences between a signal in the liquid organic scintillator and a YAP:Ce detector. The three event-types described above are clearly shown. Since all gamma-rays travel with the speed of light, the position of the gamma-flash feature remains fixed. The width of the gamma-flash is the result of electronic jitter, the physical size and geometry of the source and finite detector volume.

---

[3]Correlated cascade events are also possible but have been removed in the data analysis.

[4]Any non-correlated emissions may result in a random event. Random events are mainly source related but can also be caused by other background radiation.
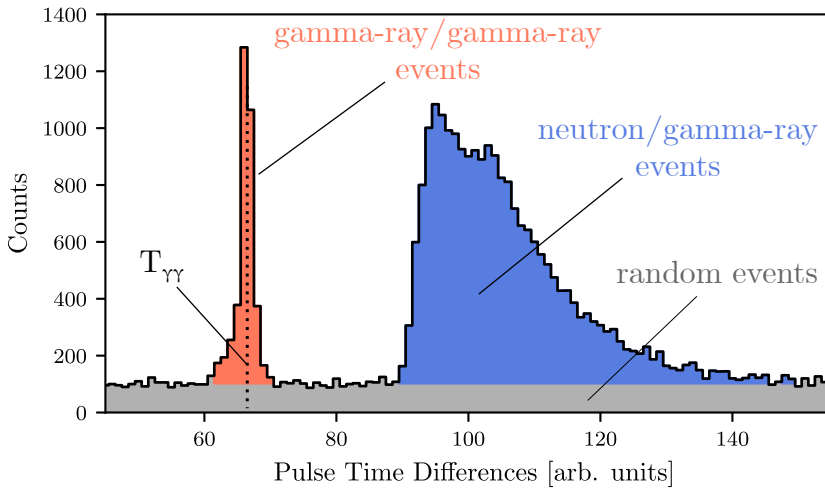
Figure 2.10: Uncalibrated time-difference spectrum. Gamma-flash (red), tagged neutrons (blue) and random background (gray) are shown. The fitted location of the gamma-flash distribution ($T_{\gamma\gamma}$, vertical dotted line) is also shown.

Figure 2.11 shows the full PuBe fast-neutron energy spectrum originally presented in Fig. 2.4 together with a tagged neutron energy spectrum by measured by Scherzinger *et al.* [62]. The tagging of the neutrons limits the maximum neutron energy to ∼6 MeV.
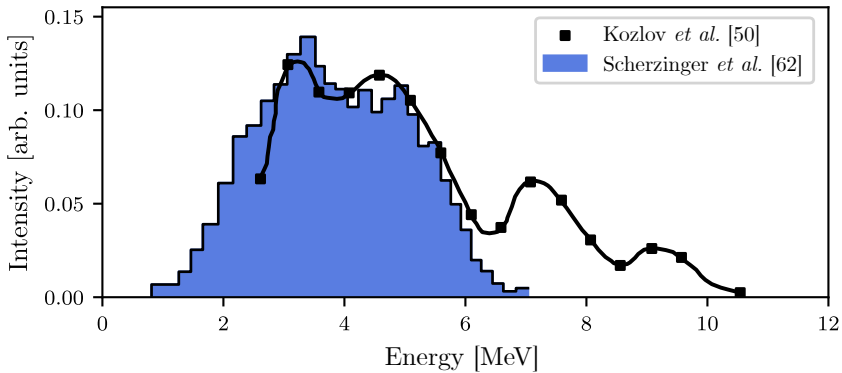
Figure 2.11: PuBe fast-neutron energy spectrum. Full energy spectrum (open histogram) as before. The tagged energy spectrum (shaded histogram) was energetically limited to ∼6 MeV.

The time origin T_0 at which the particle emission occurred was inferred from the mean location of the gamma-flash by fitting a Gaussian function to the distribution and subtracting the TOF of the gamma-ray:

$$T_0 = T_{\gamma\gamma} - \frac{d}{c},$$

where $T_{\gamma\gamma}$ is the mean location of the gamma-flash, d is the distance between the source and liquid organic scintillator and c is the speed of light. Establishing the timing of T_0 resulted in the calibrated TOF spectrum shown in Fig. 2.12. Calibrated neutron-energy spectra could then be produced.

The random-event contribution was subtracted [67] from each neutron-energy bin. Note that the extent of the random-event region (ω_{random}) selected for this subtraction was from -750 ns to -50 ns in the nonphysical region of the distribution, which assured that the data set was truly random.
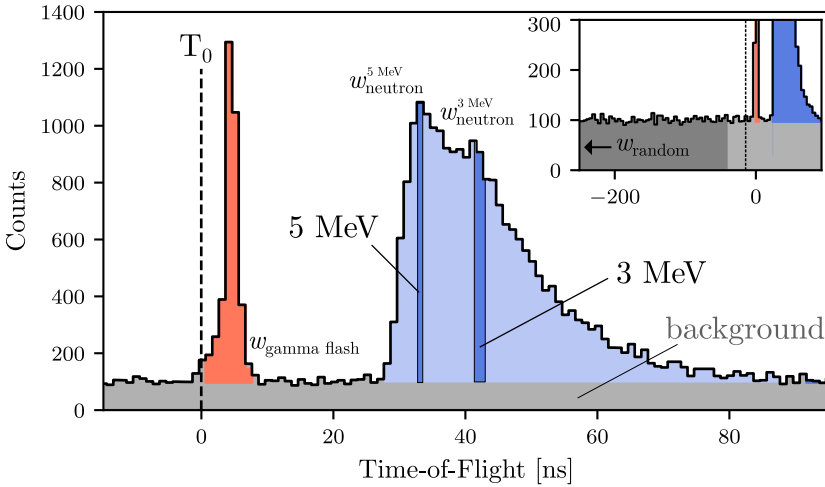
Figure 2.12: Calibrated TOF spectrum. The gamma-flash (red), tagged neutron (blue) and random background (gray) are shown along with 3 and 5 MeV neutron-energy bins (dark blue). The calculated position of T_0 (vertical dashed line) is also shown. The inset shows the random region selected for background subtraction.

A comparison between the analog-based TOF setup used in previous studies [64, 68] and the digitizer-based TOF setup employed in this work can be found in Ref. [44], where the potential of digital-waveform processing was first mentioned.

2.5   Data Sets

The PuBe neutron source was placed at the center of the Aquarium at a distance of 925 mm from the face of the liquid organic scintillator detector (see Fig. 2.8). The YAP:Ce detector thresholds were set to 3 MeV. This resulted in the 4.44 MeV gamma-ray associated with the decay of the first excited state of ^{12}C being selected by the YAP:Ce. It also resulted in a suppression of the random background for the TOF measurements. The threshold of the liquid organic scintillator detector was set to 100 keV. Two data sets were collected for each liquid organic scintillator: a neutron TOF data set and a gamma-ray calibration data set. A gamma-ray calibration data set was also collected for the YAP:Ce detectors. The typical total run time for the TOF measurements for each scintillator was 140 h, taken in 1 h increments. The typical run time for the gamma-ray irradiations was 1 h, and 10 h for background measurements.

Chapter 3

Methods

3.1   Monte Carlo Simulation

A Monte Carlo (MC) simulation is a numerical approach to calculating predictions of complex models involving probability distributions. MC-based simulations are not unique to the field of physics or even natural science and can be found in other fields such as sociology [69] and finance [70]. Consider for example a particle traveling through a material. The particle, based on its properties and the properties of the material, will have a probability of interacting with the material in many different ways. This may be through ionization, elastic scattering or absorption, for example. The probabilities for these interactions, which have been experimentally determined or modeled, are randomly sampled by the MC. Given enough sampling, a pattern may emerge resulting in a predicted outcome. A precise MC which replicates data may be used as a cheaper, virtual alternative to measurements.

GEANT4 (GEometry ANd Tracking) is a MC-based simulation toolkit developed at Conseil Européen pour la Recherche Nucléaire (CERN) [71] to simulate particle interactions with matter, including detector responses. There exists a wide variety of GEANT4-based simulation toolkits developed for use in related fields of research such as space exploration [72] and medicine [73] (to name a few). For this work, a GEANT4-based simulation of the detector geometry was developed[1] which featured scintillation-photon tracking. The simulation employed GEANT4 version 4.10.04 [74] patch 03 (8 February 2019) using electromagnetic physics classes `G4EmStandardPhysics`, `G4EmExtraPhysics`, hadronic physics class `FTFP_BERT_HP` and optical photon production class `G4OpticalPhysics`. The scintillation photons were generated by a single gamma-ray or neutron and tracked through

---

[1]Detailed technical information regarding the GEANT4 code developed for this work can be found in Appendix A.1.

the detector assembly. For the best possible agreement with data, a GEANT4 simulation requires accurate material definitions. Special care was taken with the refractive indices, ^{1}H/^{12}C ratios, densities and absorption lengths for each material making up the detector assembly. The scintillation photons which reached the photocathode were converted to photoelectrons with an energy-dependent quantum efficiency [61]. The simulations considered both reflection at medium boundaries (governed by the index of refraction of the material) and bulk absorption (which effectively removed the scintillation photons from the simulation).

3.2   Event Sampling

Radioactive sources generally emit particles isotropically. In order to reproduce the experimental data, a quasi-isotropic particle-emission routine was implemented in the simulations. This allowed for the reproduction of partial hits or clipping events, where a primary particle only passed through the edge of the scintillator volume. A true isotropic source of ionizing radiation was approximated by randomizing the particle direction, event-by-event, into a conical shape which intersected the upstream face of the detector assembly. Compared to an isotropic source radiating into 4π steradians, this quasi-isotropic approach saved greatly on computing resources as the majority of events generated struck the detector. A pencil-beam particle-emission routine was also implemented to allow for the disentanglement of inherent detector properties such as resolution. Together, the isotropic and pencil-beam simulations facilitated an excellent reproduction of the experimental data and a more detailed study of the underlying detection mechanisms. 3D views of the isotropic and pencil-beam particle sources is shown in Fig. 3.1.
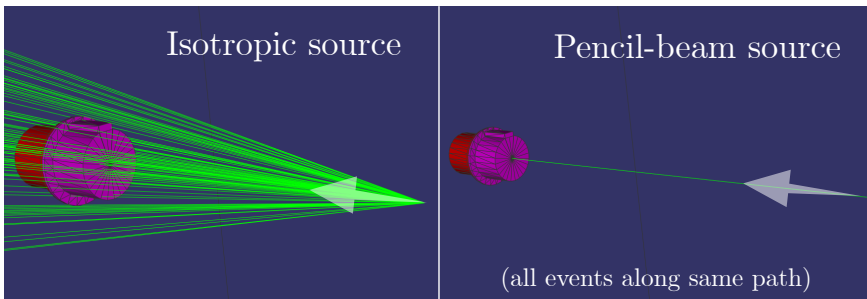
Figure 3.1: 3D views of isotropic and pencil-beam sources. GEANT4 representation of isotropic (left) and pencil-beam (right) simulations. A beam of neutrons (green) is shown incident on the scintillator cup (pink) and PMT (red) assembly from right to left.

Simulated photoelectron spectra at the photocathode of the PMT are shown in Fig. 3.2 for both isotropic and pencil-beam simulations for neutrons and gamma-rays. In both

cases, the edge of the photoelectron distribution corresponding to the isotropic simulation is about 5% lower than the pencil-beam simulation. Further, a relatively larger number of photoelectrons appear in the tail of the isotropic simulation. These effects are attributed to the highly confined spacial distribution of scintillation photons associated with the pencil beam, with the production confined to the symmetry axis of the detector. Scintillation quenching suffered by recoiling protons (neutron interactions) and the lack thereof by recoiling electrons (gamma-ray interactions) is also illustrated by the decrease in the number of photoelectrons produced per MeV in the case of the neutron distribution.
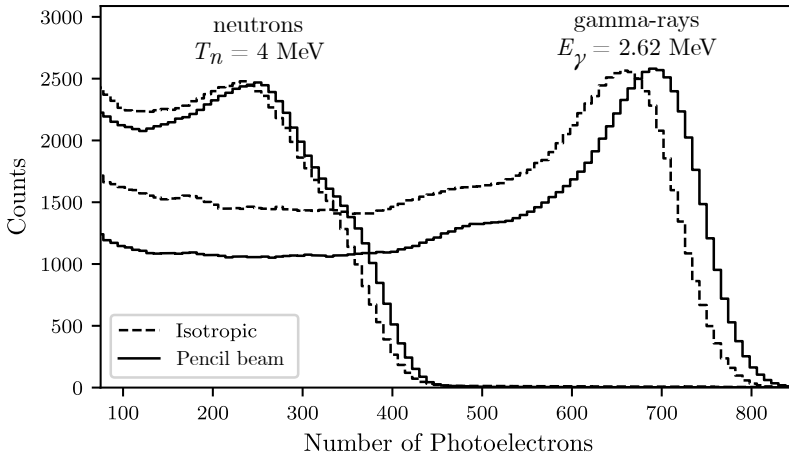
Figure 3.2: Simulated isotropic and pencil-beam photoelectron distributions at the PMT photocathode. Isotropic (dashed lines) and pencil-beam (solid lines) simulations. The heights of the distributions have been fixed for visualization. EJ 305 scintillator.

Two main simulation sets were produced: a gamma-ray simulation set used for detector calibration and a neutron simulation set used for the evaluation of neutron scintillation. These sets were further divided into $(S_\gamma^{\text{iso}}, S_\gamma^{\text{pen}})$ and $(S_n^{\text{iso}}, S_n^{\text{pen}})$ subgroups for gamma-rays and neutrons, respectively.

The gamma-ray simulations included:

- S_γ^{iso}: produced to match the gamma-ray calibration data as closely as possible using an isotropic source. Photoelectrons produced by recoiling secondary electrons were counted.

- S_γ^{pen}: produced to study the inherent detector behavior using a pencil-beam source. Photoelectrons produced by recoiling secondary electrons were again counted. Furthermore, only events depositing within $2\,\text{keV}$ of $E_{\text{CE}}^{\text{max}}$ were chosen.

The neutron simulations included:

- S_n^{iso}: produced to match the neutron scintillation data as closely as possible using an isotropic source and energy-optimized kB values (see below). Photoelectrons produced by recoiling protons were counted.

- S_n^{pen}: produced to study the inherent detector behaviour using a pencil-beam source. Monoenergetic neutrons and energy-optimized kB values were employed (see below). Photoelectrons produced by recoiling protons were counted if the neutron-energy deposition was within 1% of the incident neutron energy.

The neutron simulations ranged from $2 - 6\,\text{MeV}$ in $0.25\,\text{MeV}$ steps.

3.3 Geant4-based Detector Calibration

The simulation-based gamma-ray data-calibration method allowed for the mapping of measured charge-based data in units of QDC channels to electron-equivalent energies (MeV$_{ee}$). Electron-equivalent refers to the energy an electron needs to generate the same amount of scintillation light produced by a quenching particle such as a proton. The relatively low Z-value composition of organic scintillators result in gamma-ray interactions occuring mainly through Compton scattering. This makes it difficult to reliably identify measured features such as peaks for calibration purposes as none are present.

The simulated detector responses to several different gamma-rays were matched to the background-subtracted data obtained for the same gamma-rays. Matching was optimized at the Compton edge location using a least-squares minimization method and included smearing[2]. Figure 3.3 shows a typical calibration with background-subtracted experimental data and the simulations S_γ^{iso} and S_γ^{pen} for three different gamma-ray energies. The S_γ^{iso} simulation set matches the measured Compton edge while the heavily constrained S_γ^{pen} simulation set produced a more peak-like feature corresponding to $E_{\text{CE}}^{\text{max}}$. The Compton-edge locations were determined by fitting a Gaussian function to S_γ^{pen} and then averaging the simulation over $\pm 3\sigma$ of the fitted function. A zero-enforced linear fit was used to determine the calibration for each scintillator material. The results are summarized in Table 3.1.

---

[2]The Compton edge distribution smearing ranged from $\sim 25\%$ at $0.34\,\text{MeV}_{ee}$ (^{22}Na) to $\sim 10\%$ at $4.20\,\text{MeV}_{ee}$ (AmBe) for all scintillators and matches well with previous work on similar detectors [64].
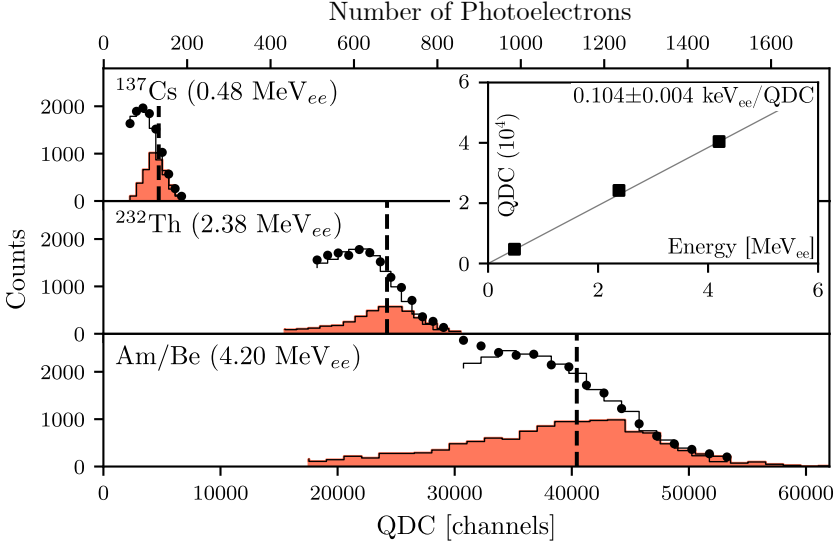
Figure 3.3: Energy calibration. Data (filled points), S_γ^{iso} (solid lines), S_γ^{pen} (filled histograms) and the peak positions (vertical dashed lines) corresponding to $E_{\text{CE}}^{\text{max}}$ are shown. The inset figure shows the resulting energy calibration and fit. NE 213A scintillator.

The simulated photoelectron distributions from the S_γ^{pen} simulation were used to calibrate these to MeV_{ee}. The results are summarized in Table 3.1. This approach allowed the neutron simulations to be calibrated to the experimental data directly.

Table 3.1: Electron-equivalent calibrations. Zero-enforced calibration values for data and simulation.

Units	NE 213A	EJ 305	EJ 331	EJ 321P
$[\frac{\text{photoelectrons}}{\text{MeV}_{ee}}]$	3810 ± 90	3530 ± 80	3910 ± 90	4050 ± 90
$[\frac{\text{keV}_{ee}}{\text{channel}}]$	0.111 ± 0.002	0.066 ± 0.002	0.099 ± 0.001	0.144 ± 0.002

3.4 Tuning of Birks Parameter and Smearing

The built-in scintillation quenching function standard to GEANT4 considers the Birks parameter but lacks the second-order energy-dependent term which is claimed by some authors [75, 76] to produce better agreement. Rather than modifying GEANT4, an energy-dependent kB optimization was performed. The tuning of Birks parameter was only relevant for the neutron light-yield simulations due to the relatively high ionization density of the recoiling protons. Gamma-rays produce scintillation light via recoiling electrons which have a much lower ionization density, resulting in a linear light output.

When simulating the neutron-scintillation response, the Birks parameter was tuned to optimize the agreement with measured data at each neutron energy. Figure 3.4 illustrates the method. A range of six kB values was simulated and the multiplicative scale factor Δ needed to match the results of each simulation with the data was determined with a least-squares minimization. Each optimization included an energy-dependent smearing[3] which was derived through a separate least-squares minimization.

The optimal kB value was determined by linearly fitting the (kB, Δ) data set and locating $\Delta = 1$. The smearing value was determined by averaging the individual smearing values. In general, the highest kB value required the least amount of smearing to match the data.
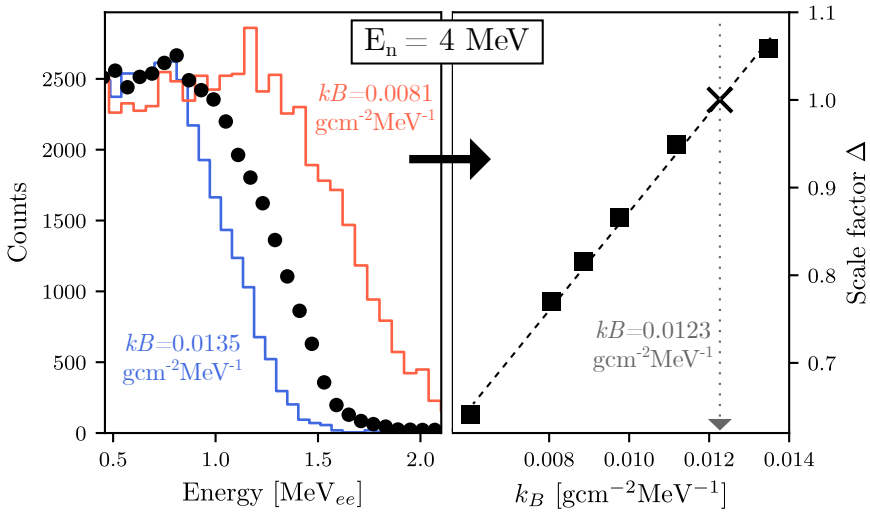
Figure 3.4: Optimization method for kB values. Left: experimental data (filled circles) and neutron simulations (blue and red) with smearing values of 12% and 13%, respectively. Right: optimization. EJ 305 scintillator.

This process was repeated for neutron energies from $2 - 6\,\text{MeV}$ in $0.5\,\text{MeV}$ steps for each of the scintillator materials. The optimal smearing values varied from $\sim$35% at $2\,\text{MeV}$ to $\sim$5% at $6\,\text{MeV}$ for all scintillators. The optimized kB and smearing distributions were each fitted according to:

$$f(E_n) = \frac{A}{E_n} + B, \tag{3.1}$$

---

[3]Smearing was applied to take into account all effects not currently considered within the simulation, such as the physical size and geometry of the radioactive source, electronic noise and signal propagation (to name a few).

where A and B are constants. Figure 3.5 shows the optimized values and the fitted trends. The fitted trends were used as inputs to the simulations of S_n^{iso} and S_n^{pen}.
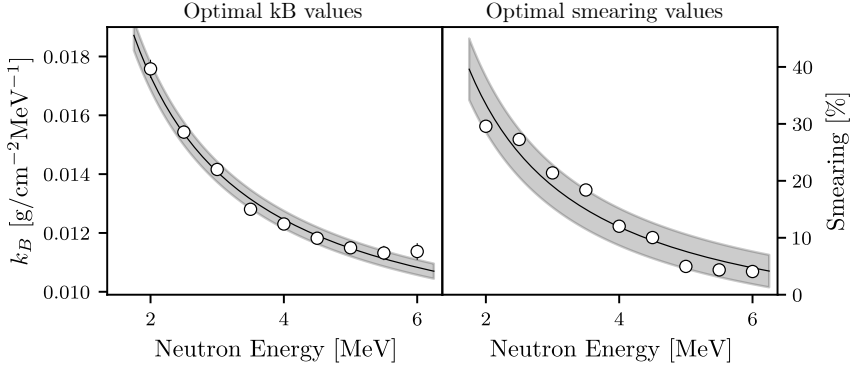
Figure 3.5: Optimized kB and smearing values. Data points (white circles), fitted trends (solid lines) and uncertainties in the fitted trends (shaded area) are shown. EJ 305 scintillator.

Figure 3.6 shows the results obtained with the constant kB built-in GEANT4 quenching mechanism and those obtained using the energy-dependent kB values. The constant kB value was determined using the 4 MeV neutron data set and the method explained above. This resulted in the best agreement at $E_n = 4\,\text{MeV}$, but poorer agreement at other energies. The optimized kB value and smearing for each neutron energy resulted in excellent agreement across the entire energy range.
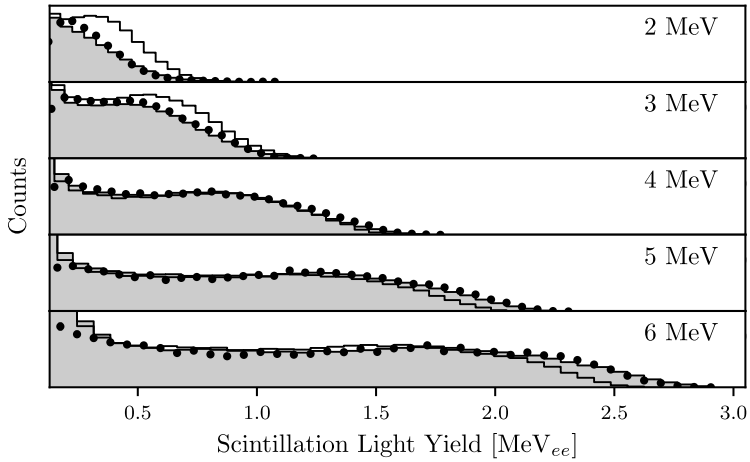
Figure 3.6: Simulations performed with energy-dependent and energy-independent kB. Measured calibrated scintillation light yield (filled circles) and simulations shown without (open histograms) and with (shaded histograms) energy dependence. EJ 305 scintillator.

3.5 Intrinsic Pulse-Shape Discrimination

PS was studied for $2-6\,\mathrm{MeV}$ neutrons in $0.25\,\mathrm{MeV}$ steps for each scintillator. The PS was considered intrinsic rather than integrated since the application of TOF cuts resulted in PS distributions corresponding to gamma-rays and neutrons, respectively. Figure 3.7 shows a PS spectrum produced with uncorrelated and correlated data for an NE 213A liquid organic scintillator employing a $2\,\mathrm{MeV}_{ee}$ detector threshold. The uncorrelated data show a typical broad PS distribution with the left peak representing gamma-rays and the right peak representing neutrons. The correlated data result from TOF cuts around the tagged-neutron and gamma-flash features. Both distributions were corrected for randoms. Note the separation between the data sets for each particle species and also the appearance of two peaks in the neutron distribution. The left "neutron" peak is the result of non-prompt gamma-rays (NPGs). These are events with a neutron time signature but the PS signature of a gamma-ray. They are generally caused by fast neutrons inelastically scattering in the Pb shielding (or the detector materials [4, 77]). The de-excitation of the excited Pb nucleus results in the emission of gamma-rays which are detected in the liquid organic scintillator. A high purity germanium gamma-ray detector was used to study the energies of the NPG contributions. The results showed that the main contribution was from the excited states of $^{\mathrm{nat}}$Pb, predominately the $2.615\,\mathrm{MeV}$ gamma-ray from the de-excitation of the first excited state of ^{208}Pb.
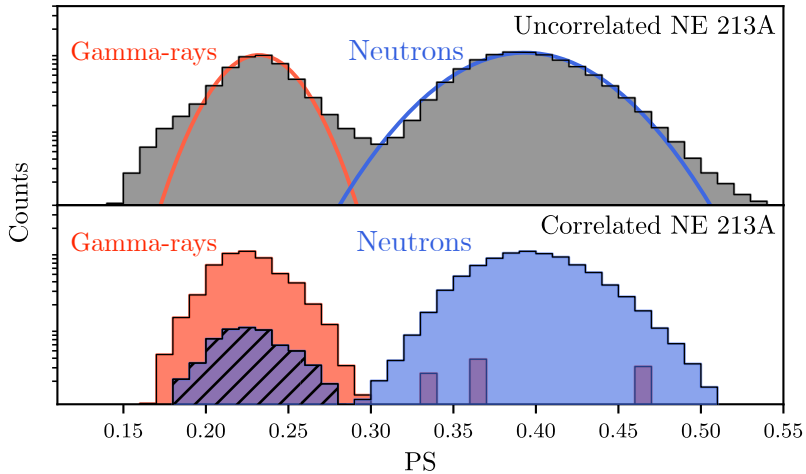
Figure 3.7: Pulse-shape spectra for the NE 213A scintillator. Top: uncorrelated data, without neutron tagging. The red and blue curves are Gaussian fits. Bottom: correlated data where TOF was used to separate the neutron and gamma-ray distributions. The diagonally hatched areas show the non-prompt gamma-ray contributions. A $2\,\mathrm{MeV}_{ee}$ detector threshold was employed.

Gaussian functions may be fitted to the gamma-ray and neutron distributions to extract a figure-of-merit (FOM) for n/γ discrimination. This FOM value allows for comparison of the PSD capabilities of different scintillators and is defined as:

$$\text{FOM} = \frac{|\mu_n - \mu_\gamma|}{\text{FWHM}_n - \text{FWHM}_\gamma}, \tag{3.2}$$

where $\mu_{n,\gamma}$ are the mean positions and $\text{FWHM}_{n,\gamma}$ are the full-widths-at-half-maximum of the gamma-ray and neutron PS distributions. A larger FOM value indicates better n/γ separation. The FOM values resulting from the intrinsic PS data for NE 213A and EJ 305 liquid organic scintillators are shown as a function of detector threshold in Fig. 3.8 and neutron kinetic energy in Fig. 3.9. Overall, NE 213A shows better PSD performance compared to EJ 305. Both scintillators show dependence on threshold but little dependence on neutron energy.
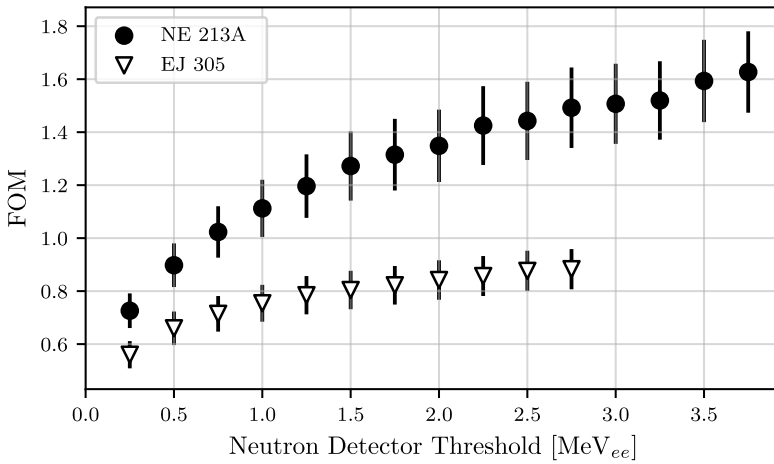
Figure 3.8: Threshold dependent figures-of-merit. FOM extracted from correlated PS data for NE 213A (black dots) and EJ 305 (open triangles).
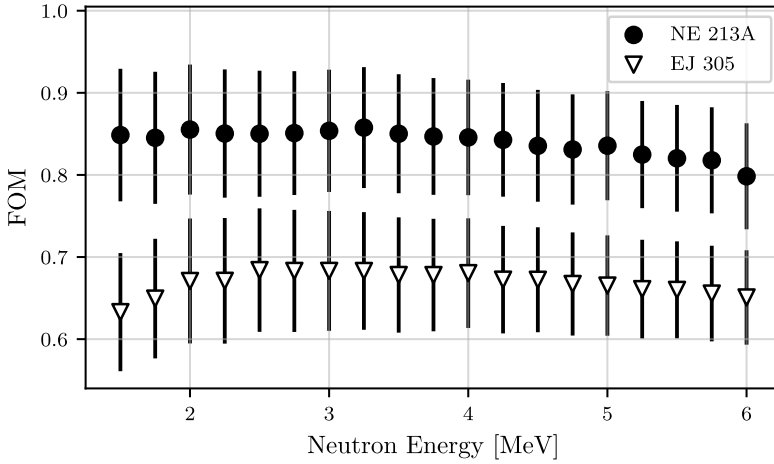
Figure 3.9: Energy dependent figures-of-merit. FOM extracted from correlated PS data for NE 213A (black dots) and EJ 305 (open triangles). A $0.5\,\mathrm{MeV}_{ee}$ detector threshold was employed.

3.6 Neutron Light-Yield Response

A simulation-based method was also developed to determine the maximum proton transfer-edge locations corresponding to a single neutron scatter in the liquid scintillators. Figure 3.10 shows the random-subtracted data for 2, 4 and 6 MeV beams of neutrons incident on EJ 305. S_n^{iso} and S_n^{pen} are also shown. The calibration of the simulation resulted in very good agreement with the data. The neutron scintillation-light yield associated with the maximum proton transfer-edge location was determined by considering S_n^{pen}. The insert figure shows the neutron-energy deposition resulting from proton recoils only, along with a 1% energy cut employed to produce the heavily constrained S_n^{pen} sample set shown in dark blue. The recoil-proton edge was determined fitting a Gaussian function to the S_n^{pen} and then averaging the simulation over $\pm 3\sigma$ of the fitted function. This defined the simulated maximum deposition (SMD) marked as vertical dashed lines.
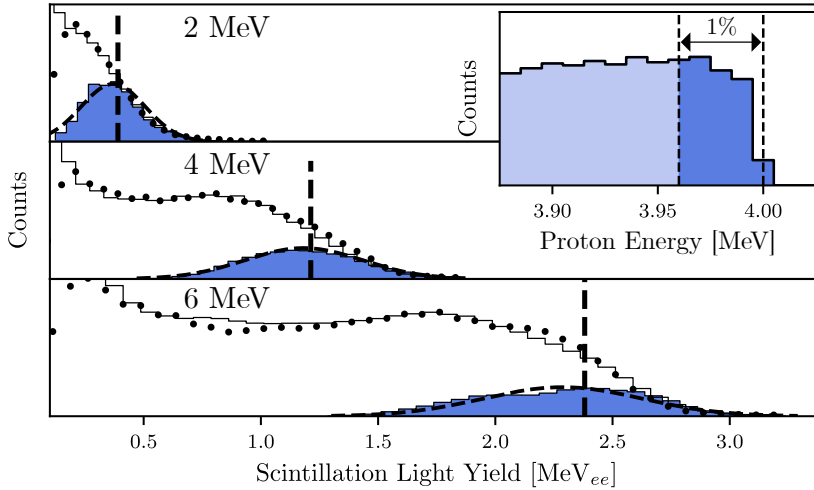
Figure 3.10: Neutron scintillation light yield. Data (filled points) and simulations S_n^{iso} (open histograms) and S_n^{pen} (shaded histograms) are shown for 2 MeV, 4 MeV and 6 MeV neutrons. The inset shows simulated recoil proton energies for 4 MeV neutrons. The dark shaded region between the vertical dashed lines is the 1% energy cut implemented to produce the S_n^{pen} simulation and corresponds to the dark shaded simulated scintillation light yields in the main panel. Fitted Gaussian functions (dashed trends) are shown together with the SMD locations (vertical dashed lines). EJ 305 scintillator.

The SMD method for determining the neutron scintillation-light yield as a function of recoil-proton energy was compared with three well-established data-driven prescriptions. The data-driven methods used to determine the maximum proton transfer-edge locations included:

- Half-Height (HH) method: a Gaussian function was fitted to the edge of the proton-recoil distribution and the location of its half-height was taken to be the maximum transfer,

- Turning-Point (TP) method: a Gaussian function was fitted to the edge of the proton-recoil distribution and the location of the minimum in the first derivative of the function was taken to be the maximum transfer,

- First-Derivative (FD) method: the minimum of the first derivative of the proton-recoil distribution was taken to be the maximum transfer.

Figure 3.11 shows the scintillation-light yield and parameterization for NE 213A using the SMD method in comparison with the three data-driven methods mentioned above. A fitted light-yield parameterization predicted by Kornilov *et al.* [78] is also shown. It is given by

$$L(E_p) = L_0 \frac{E_p^2}{E_p + L_1},$$

(3.3)

where $L(E_p)$ is the neutron scintillation-light yield based upon the specific energy loss of protons, L_0 is an adjustable scaling parameter and L_1 is a material-specific light-yield parameter. The SMD method shows especially good agreement with the TP method while predicting slightly less light yield in comparison with the HH and FD methods. Similar results were produced for EJ 305, EJ 331 and EJ 321P.
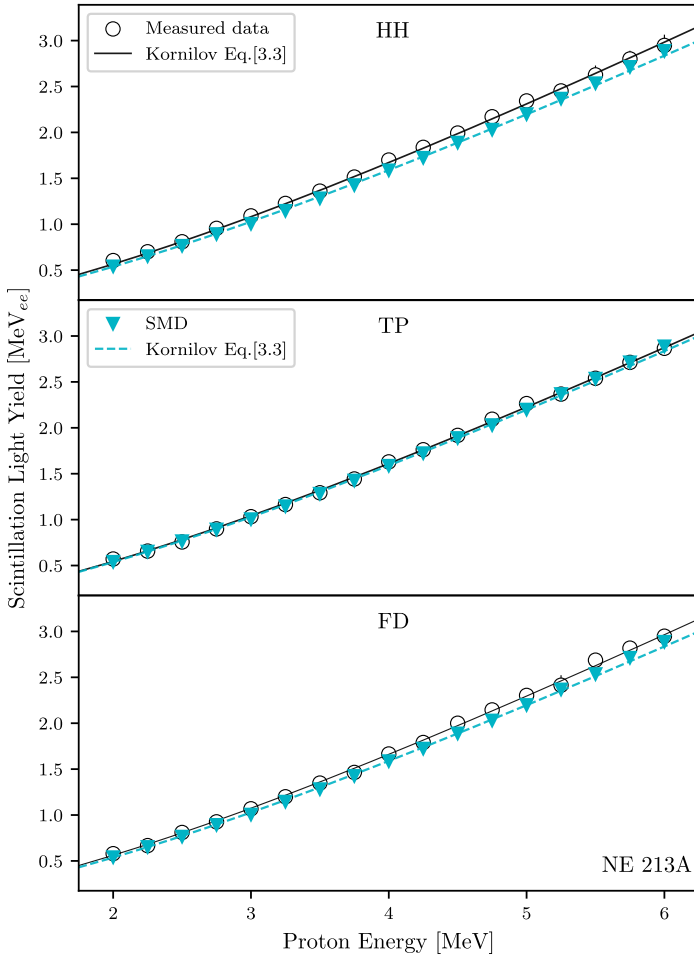
Figure 3.11: Recoil-proton light yields for NE 213A. Measured data (open circles), SMD predictions (closed triangles). The Kornilov light-yield parameterizations are shown for the measured data (black solid lines) and SMD method (blue dashed lines), respectively. The SMD results shown are the same in all panels. The uncertainties are smaller than the data points.

Chapter 4

Closing

4.1 Summary

The STF at Lund University is a dedicated environment for detector development. It has facilitated the experimental work carried out in this thesis. The neutron-tagging apparatus associated with the Aquarium infrastructure at the STF was used to perform a comprehensive series of neutron-scintillation characterizations for liquid organic scintillators. Measurements were performed on NE 213A, EJ 305, EJ 331 and EJ 321P, all of which were contained in detectors having identical physical form factors. This facilitated the the systematics of the comparison. A digitizer-based pulse-processing framework was developed which allowed for straightforward and reproducible data processing. A detailed GEANT4 simulation was created and used to interpret the data. It considered both gamma-rays and neutrons. The simulation took into account optical transmission through the detector assembly by tracking individual scintillation photons. The gamma-ray simulation was found to agree very well with gamma-ray calibration data. A carefully selected sub-set of a simulated gamma-ray spectrum allowed the Compton edge locations to be determined more accurately than with previous data-driven methods. This facilitated the energy calibration of the detectors. The intrinsic PSD capabilities of NE 213A and EJ 305 were measured using tagged neutrons. Removal of the underlying random-coincidence background facilitated a cleaner separation of the neutrons and gamma-rays. NPG events, which have a neutron TOF signature but a gamma-ray PSD signature, were identified. They were due to fast neutrons inelastically scattering in the ^{nat}Pb shielding. FOM was derived by studying the neutron/gamma-ray separation in the PS distributions. While FOM as a function of the incident neutron energy was essentially constant, FOM improved with increasing threshold. Overall, the PSD performance of NE 213A was superior to that of EJ 305. Neutron scintillation-light yield was measured for NE 213A, EJ 305, EJ 331 and EJ 321P using tagged neutrons. The simulation

was matched to the background-corrected neutron TOF data using an energy-dependent Birks parameter. The simulation approach reproduced the data very well and allowed the maximum recoil proton-edge locations to be determined more accurately than with previous data-driven methods. The response characteristics of NE 213A and EJ 305 matched existing results very well. The response characteristics of EJ 331 and EJ 321P were previously unmeasured.

4.2   Observations

Tagging via TOF allows for clear separation of neutrons and gamma-rays which promotes intrinsic rather then integrated studies of detector properties. The gamma-ray simulation facilitated the energy calibration of the measured scintillation-light yield. Compared with well-established data-driven calibration methods the simulation-based approach provided further insight into the underlying physical processes. It also allowed for the unfolding of spectra containing multiple gamma-rays, even when the energy separation between the gamma-rays is small. Further, it allowed for the quantification of background NPGs resulting from inelastic scattering of fast neutrons in shielding material and the detector apparatus itself. The coupling of PS discrimination capable detectors with neutron tagging facilitated studies of intrinsic PS, allowing for a more detailed assessment of the PS discrimination capabilities of the scintillators studied. The resulting FOM show only limited dependence on neutron energy. However, FOM show an increasing trend as a function of increasing detector threshold. The simulation-based SMD method located the maximum proton-recoil edge and facilitated a detailed scintillation light-yield calibration. This allowed for non data-driven parametrizations of the scintillation-light yield.

4.3   Outlook

Neutron-induced light-yield and light-output parameters for two previously uninvestigated scintillator materials have been presented. The gadolinium-doped scintillator EJ 331, due to the thermal-neutron sensitivity of ^{nat}Gd, may act as a bridge between fast-neutron and thermal-neutron detection. The mineral-oil based scintillator EJ 321P, due to its low toxicity and high flash point, is particularly suitable as an explosion-resistant alternative in large-volume applications. The $\sim$2 : 1 ^{1}H/^{12}C ratio makes it an excellent choice for fast-neutron detection. Next generation scintillators, including those based on mineral oil, are especially suitable for developing active neutron shielding or active moderators.

The neutron irradiation studies performed in this thesis were limited to $2 - 6$ MeV due to the 4.44 MeV gamma-ray accompanying the neutron emission. Extending this relatively

limited energy range using beams of higher energy neutrons from an accelerator-based neutron source would be a straight-forward and valuable addition to the database. Mapping the responses at higher energies would allow a better understanding of the underlying mechanisms over a more significant energy region. Mapping the responses at lower energies would likely be difficult using this technique as scattering does not produce a large enough energy transfer to the recoils for them to be detected.

A future extension of the tagging technique into the domain of thermalized neutrons may be envisioned. While thermal-neutron tagging presents many challenges, it would constitute a game-changer for source-based irradiation techniques in the field of slow-neutron science. Significant effort has already been invested in the design of a liquid organic scintillator vessel to be used as an active moderator[1]. This active moderator could provide a useful additional signal corresponding to the neutron-moderation process. This signal coupled with the tagged fast neutron and the detection of the thermalized neutron may allow for the reconstruction of the entire process from neutron emission to moderation to detection. The EJ-321P mineral-oil based scintillator would make an excellent active moderator due to its high ^{1}H/^{12}C ratio.

The gadolinium-doped scintillator EJ 331 is a relatively new hybrid scintillator. It could be used as a fast-neutron and thermal-neutron detector all-in-one. About 99% of the Q-value associated with neutron absorption on ^{nat}Gd leads to a cascade of of gamma-rays. This may require extensive studies using a high resolution gamma-ray detector. Nevertheless, the conversion of a fast neutron into a cascade of gamma-rays presents interesting possibilities, perhaps as thermal-neutron shielding.

---

[1]See Appendix A.2 for more details on the active moderator design.

References

[1] R. Zboray, R. Adams, and Z. Kis. Fast Neutron Radiography and Tomography At a 10 MW Research Reactor Beamline. *Applied Radiation and Isotopes*, 119:43–50, 2017.

[2] Toshihiko Ohnuki, Tadatoshi Yamamoto, and Yoshiki Wadachi. A Non-Destructive Method for Determining the Distribution of Soil Water Content By Measuring Fast Neutron Transmission Using an NE-213 Organic Scintillator. *Japanese Journal of Applied Physics*, 23(8R):1124, 1984.

[3] A.A Naqvi, M.M Nagadi, Khateeb ur Rehman, and S Kidwai. Performance Comparison of NE213 Detectors for Their Application in Moisture Measurement. *Applied Radiation and Isotopes*, 53(4-5):745–754, 2000.

[4] Horst Klein and Sonja Neumann. Neutron and photon spectrometry with liquid scintillation detectors in mixed fields. *Nuclear Instruments and Methods in Physics Research Section A: Accelerators, Spectrometers, Detectors and Associated Equipment*, 476(1):132–142, 2002. Int. Workshop on Neutron Field Spectrometry in Science, Technology and Radiation Protection.

[5] F. Binda, J. Eriksson, G. Ericsson, C. Hellesen, S. Conroy, M. Nocente, and E. Andersson Sundén. Generation of the Neutron Response Function of an NE213 Scintillator for Fusion Applications. *Nuclear Instruments and Methods in Physics Research Section A: Accelerators, Spectrometers, Detectors and Associated Equipment*, 866:222–229, 2017.

[6] M. Anderson, S. Andringa, E. Arushanova, S. Asahi, M. Askins, D. J. Auty, A. R. Back, Z. Barnard, N. Barros, D. Bartlett, F. Barão, R. Bayes, E. W. Beier, A. Bialek, S. D. Biller, E. Blucher, R. Bonventre, M. Boulay, D. Braid, E. Caden, E. J. Callaghan, J. Caravaca, J. Carvalho, L. Cavalli, D. Chauhan, M. Chen, O. Chkvorets, K. J. Clark, B. Cleveland, C. Connors, I. T. Coulter, D. Cressy, X. Dai, C. Darrach, B. Davis-Purcell, M. M. Depatie, F. Descamps, F. Di Lodovico, N. Duhaime, F. Duncan, J. Dunger, E. Falk, N. Fatemighomi, V. Fischer, E. Fletcher, R. Ford, N. Gagnon,

K. Gilje, P. Gorel, K. Graham, C. Grant, J. Grove, S. Grullon, E. Guillian, A. L. Hallin, D. Hallman, S. Hans, J. Hartnell, P. Harvey, M. Hedayatipour, W. J. Heintzelman, J. Heise, R. L. Helmer, J. L. Hernández-Hernández, B. Hreljac, J. Hu, T. Iida, A. S. Inácio, C. M. Jackson, N. A. Jelley, C. J. Jillings, C. Jones, P. G. Jones, K. Kamdin, T. Kaptanoglu, J. Kaspar, K. Keeter, C. Kefelian, P. Khaghani, L. Kippenbrock, J. R. Klein, R. Knapik, J. Kofron, L. L. Kormos, B. Krar, C. Kraus, C. B. Krauss, T. Kroupova, K. Labe, I. Lam, C. Lan, B. J. Land, R. Lane, S. Langrock, A. LaTorre, I. Lawson, L. Lebanowski, G. M. Lefeuvre, E. J. Leming, A. Li, J. Lidgard, B. Liggins, X. Liu, Y. Liu, V. Lozza, M. Luo, S. Maguire, A. Maio, K. Majumdar, S. Manecki, J. Maneira, R. D. Martin, E. Marzec, A. Mastbaum, N. McCauley, A. B. McDonald, J. E. McMillan, P. Mekarski, M. Meyer, C. Miller, M. Mlejnek, E. Mony, I. Morton-Blake, M. J. Mottram, S. Nae, M. Nirkko, V. Novikov, H. M. O'Keeffe, E. O'Sullivan, G. D. Orebi Gann, M. J. Parnell, J. Paton, S. J. M. Peeters, T. Pershing, Z. Petriw, L. Pickard, D. Pracsovics, G. Prior, J. C. Prouty, S. Quirk, A. Reichold, R. Richardson, M. Rigan, A. Robertson, J. Rose, R. Rosero, P. M. Rost, J. Rumleskie, M. A. Schumaker, M. H. Schwendener, D. Scislowski, J. Secrest, M. Seddighin, L. Segui, S. Seibert, I. Semenec, T. Shantz, T. M. Shokair, L. Sibley, J. R. Sinclair, K. Singh, P. Skensved, T. Sonley, R. Stainforth, M. Strait, M. I. Stringer, R. Svoboda, A. Sörensen, B. Tam, J. Tatar, L. Tian, N. Tolich, J. Tseng, H. W. C. Tseung, E. Turner, R. Van Berg, J. G. C. Veinot, C. J. Virtue, B. von Krosigk, E. Vázquez-Jáuregui, J. M. G. Walker, M. Walker, J. Wang, O. Wasalski, J. Waterfield, J. J. Weigand, R. F. White, J. R. Wilson, T. J. Winchester, P. Woosaree, A. Wright, J. P. Yanez, M. Yeh, T. Zhao, K. Zuber, and A. Zummo. Search for invisible modes of nucleon decay in water with the SNO+ detector. *Phys. Rev. D*, 99:032008, Feb 2019.

[7] Michael F L'Annunziata, Alex Tarancón, Héctor Bagán, and José F García. Liquid scintillation analysis: principles and practice. In *Handbook of radioactivity analysis*, pages 575–801. Elsevier, 2020.

[8] G. Pédehontaa-Hiaa, H. Holstein, S. Mattsson, C.L. Rääf, and K.E. Stenström. Tritium in urine from members of the general public and occupationally exposed workers in Lund, Sweden, prior to operation of the European Spallation Source. *Journal of Environmental Radioactivity*, 213:106141, 2020.

[9] William R Leo. *Techniques for nuclear and particle physics experiments: a how-to approach*. Springer-Verlag, 1987.

[10] Sebastian Jaksch, Ralf Engels, Günter Kemmerling, Uwe Clemens, Sylvain Désert, Hanno Perrey, Codin Gheorghe, Arne Fredriksen, Petter Øya, Henrich Frielinghaus, et al. Recent developments SoNDe high-flux detector project. In *Proceedings of the International Conference on Neutron Optics (NOP2017)*, page 011019, 2018.

[11] G.F. Knoll. *Radiation Detection and Measurement.* Wiley, New York, NY, U.S.A., 1989.

[12] nuclear-power.com. `https://www.nuclear-power.com/`.

[13] E. Rofors, H. Perrey, R. Al Jebali, J.R.M. Annand, L. Boyd, U. Clemens, S. Desert, R. Engels, K.G. Fissum, H. Frielinghaus, C. Gheorghe, R. Hall-Wilton, S. Jaksch, A. Jalgén, K. Kanaki, G. Kemmerling, V. Maulerova, N. Mauritzson, R. Montgomery, J. Scherzinger, and B. Seitz. Response of a Li-glass/multi-anode photomultiplier detector to α-particles from ^{241}Am. *Nuclear Instruments and Methods in Physics Research Section A: Accelerators, Spectrometers, Detectors and Associated Equipment*, 929:90–96, 2019.

[14] D.A. Brown, M.B. Chadwick, R. Capote, A.C. Kahler, A. Trkov, M.W. Herman, A.A. Sonzogni, Y. Danon, A.D. Carlson, M. Dunn, D.L. Smith, G.M. Hale, G. Arbanas, R. Arcilla, C.R. Bates, B. Beck, B. Becker, F. Brown, R.J. Casperson, J. Conlin, D.E. Cullen, M.-A. Descalle, R. Firestone, T. Gaines, K.H. Guber, A.I. Hawari, J. Holmes, T.D. Johnson, T. Kawano, B.C. Kiedrowski, A.J. Koning, S. Kopecky, L. Leal, J.P. Lestone, C. Lubitz, J.I. Márquez Damián, C.M. Mattoon, E.A. McCutchan, S. Mughabghab, P. Navratil, D. Neudecker, G.P.A. Nobre, G. Noguere, M. Paris, M.T. Pigni, A.J. Plompen, B. Pritychenko, V.G. Pronyaev, D. Roubtsov, D. Rochman, P. Romano, P. Schillebeeckx, S. Simakov, M. Sin, I. Sirakov, B. Sleaford, V. Sobes, E.S. Soukhovitskii, I. Stetcu, P. Talou, I. Thompson, S. van der Marck, L. Welser-Sherrill, D. Wiarda, M. White, J.L. Wormald, R.Q. Wright, M. Zerkle, G. Žerovnik, and Y. Zhu. ENDF/B-VIII.0: The 8th Major Release of the Nuclear Reaction Data Library with CIELO-project Cross Sections, New Standards and Thermal Scattering Data. *Nuclear Data Sheets*, 148:1–142, 2018. Special Issue on Nuclear Reaction Data.

[15] JH Hubbell. Review of photon interaction cross section data in the medical and biological context. *Physics in Medicine & Biology*, 44(1):R1, 1999.

[16] Paul Lecoq. Development of new scintillators for medical applications. *Nuclear Instruments and Methods in Physics Research Section A: Accelerators, Spectrometers, Detectors and Associated Equipment*, 809:130–139, 2016. Advances in detectors and applications for medicine.

[17] Alexander Wolfertz, Robert Adams, and Grégory Perret. First tests of a gamma-blind fast neutron detector using a ZnS:Ag-epoxy mixture cast around wavelength-shifting fibers. *Nuclear Instruments and Methods in Physics Research Section A: Accelerators, Spectrometers, Detectors and Associated Equipment*, 971:164003, 2020.

[18] M Moszyński. Inorganic scintillation detectors in γ-ray spectrometry. *Nuclear Instruments and Methods in Physics Research Section A: Accelerators, Spectrometers, Detectors and Associated Equipment*, 505(1-2):101–110, 2003.

[19] John Betteley Birks. *The theory and practice of scintillation counting: International series of monographs in electronics and instrumentation*, volume 27. Elsevier, 1964.

[20] Nicholas J Turro, Vaidhyanathan Ramamurthy, Juan C Scaiano, et al. *Modern molecular photochemistry of organic molecules*, volume 188. University Science Books Sausalito, CA, 2010.

[21] Warren L. Buck. The Origin of Scintillations in Organic Materials. *IRE Transactions on Nuclear Science*, 7(2/3):11–16, 1960.

[22] AA Noujaim, C Ediss, and LI Weibe. *Liquid scintillation: science and technology*. Academic Press, 2013.

[23] J B Birks. Scintillations from Organic Crystals: Specific Fluorescence and Relative Response to Different Radiations. *Proceedings of the Physical Society. Section A*, 64(10):874, oct 1951.

[24] K. Wilhelm, J. Nattress, and I. Jovanovic. Development and operation of a ^{6}LiF:ZnS(Ag)—scintillating plastic capture-gated detector. *Nuclear Instruments and Methods in Physics Research Section A: Accelerators, Spectrometers, Detectors and Associated Equipment*, 842:54–61, 2017.

[25] M.P. Taggart, M. Nakhostin, and P.J. Sellin. Investigation into the potential of GAGG:Ce as a neutron detector. *Nuclear Instruments and Methods in Physics Research Section A: Accelerators, Spectrometers, Detectors and Associated Equipment*, 931:121–126, 2019.

[26] N, Mauritzson. Design, Construction and Characterization of a Portable Fast-Neutron Detector. *Lund University*, 2017. Student Paper.

[27] P.J. Sellin, G. Jaffar, and S.D. Jastaniah. Performance of digital algorithms for n/γ pulse shape discrimination using a liquid scintillation detector. *IEEE Nuclear Science Symposium. Conference Record IEEE Cat. No.03CH37515*, pages 1057–1060 Vol.2, 2003.

[28] V.T Jordanov, J.A Pantazis, and A.C Huber. Compact Circuit for Pulse Rise-Time Discrimination. *Nuclear Instruments and Methods in Physics Research Section A: Accelerators, Spectrometers, Detectors and Associated Equipment*, 380(1):353–357, 1996.

[29] JRM Annand, B-E Andersson, I Akkurt, and B Nilsson. An NE213A TOF spectrometer for high resolution (γ, n) reaction measurements. *Nuclear Instruments and Methods in Physics Research Section A: Accelerators, Spectrometers, Detectors and Associated Equipment*, 400(2-3):344–355, 1997.

[30] EJ-305 Highest Light output Liquid Scintillator. `http://www.ggg-tech.co.jp/maker/eljen/ej-305.html`.

[31] EJ-331, EJ-335 – Gadolinium Loaded Liquid Scintillator – Eljen Technology. https://eljentechnology.com/products/liquid-scintillators/ej-331-ej-335.

[32] EJ-321 Series – Mineral Oil Based Liquid Scintillator – Eljen Technology. https://eljentechnology.com/products/liquid-scintillators/ej-321-series.

[33] NE-213 is no longer produced. Eljen Technologies offers EJ-301 while Saint Gobain offers BC-501. https://eljentechnology.com/products/liquid-scintillators/ej-301-ej-309, https://www.crystals.saint-gobain.com/radiation-detection-scintillators/liquid-scintillators/neutron-gamma-psd-bc-501a-bc-519.

[34] Francesco Messi, H Perrey, K Fissum, M Akkawi, R Al Jebali, JRM Annand, P Bentley, L Boyd, CP Cooper-Jensen, DD DiJulio, et al. The neutron tagging facility at Lund University. *International Atomic Energy Agency (IAEA), IAEA-TECDOC–1935*, 2020.

[35] Hanno Perrey, Linus Ros, Mikael Elfman, Ulrika Bäckström, Per Kristiansson, and Anders Sjöland. Evaluation of the in-situ performance of neutron detectors based on EJ-426 scintillator screens for spent fuel characterization. *Nuclear Instruments and Methods in Physics Research Section A: Accelerators, Spectrometers, Detectors and Associated Equipment*, 1020:165886, 2021.

[36] B Seitz, JRM Annand, L Boyd, and K Fissum. Modern Neutron Detectors with Fast Timing Resolution. In *Modern Neutron Detection: Proceedings of a Technical Meeting*, pages 273–277, 2020.

[37] Francesco Piscitelli, Giacomo Mauri, Alessio Laloni, and Richard Hall-Wilton. Verification of He-3 proportional counters' fast neutron sensitivity through a comparison with He-4 detectors-He-3 and He-4 proportional counters' fast neutron sensitivity and evaluation of the cosmic neutron fluxes at ESS. *The European Physical Journal Plus*, 135(7):577, 2020.

[38] G Mauri, I Apostolidis, MJ Christensen, A Glavic, Chung-Chuan Lai, A Laloni, F Messi, A Lindh Olsson, L Robinson, J Stahn, et al. The Multi-Blade Boron-10-based neutron detector performance using a focusing reflectometer. *Journal of Instrumentation*, 15(03):P03010, 2020.

[39] Giacomo Mauri, Francesco Messi, Kalliopi Kanaki, Richard Hall-Wilton, and Francesco Piscitelli. Fast neutron sensitivity for 3He detectors and comparison with Boron-10 based neutron detectors. *EPJ Techniques and Instrumentation*, 6(1):3, 2019.

[40] Giacomo Mauri, Francesco Messi, Kalliopi Kanaki, Richard Hall-Wilton, E Karnickis, Anton Khaplanov, and F Piscitelli. Fast neutron sensitivity of neutron detectors based on boron-10 converter layers. *Journal of Instrumentation*, 13(03):P03004, 2018.

[41] F Messi, F Piscitelli, G Mauri, M Anastasopoulos, K Fissum, Richard Hall-Wilton, C Höglund, K Kanari, E Karnickis, A Khaplanov, et al. Gamma-and Fast Neutron-Sensitivity of 10 B-Based Neutron Detectors at ESS. In *2017 IEEE Nuclear Science Symposium and Medical Imaging Conference (NSS/MIC)*, pages 1–2. IEEE, 2017.

[42] D.D. DiJulio, C.P. Cooper-Jensen, H. Perrey, K. Fissum, E. Rofors, J. Scherzinger, and P.M. Bentley. A polyethylene-B_4C based concrete for enhanced neutron shielding at neutron research facilities. *Nuclear Instruments and Methods in Physics Research Section A: Accelerators, Spectrometers, Detectors and Associated Equipment*, 859:41–46, 2017.

[43] V. Maulerova. Vanadium-based neutron-beam monitor. *Lund University*, 2019. Student Paper.

[44] R. Kjær Høier. Identification of Neutrons Using Digitized Waveforms. *Lund University*, 2019. Student Paper.

[45] J. Scherzinger. Neutron Irradiation Techniques. *Lund University*, 2016. PhD thesis.

[46] E. Rofors. A Fast Pixelated Thermal-Neutron Detector. *Lund University*, 2020. PhD thesis.

[47] James Chadwick. Possible existence of a neutron. *Nature*, 129(3252):312–312, 1932.

[48] A.D. Vijaya and Arun Kumar. The neutron spectrum of Am/Be neutron sources. *Nuclear Instruments and Methods*, 111(3):435–440, 1973.

[49] E. Browneand J. K. Tuli. NuData: Nuclear Data Sheets 122, 205 (2014). `https://www.nndc.bnl.gov/nudat3`.

[50] AG Kozlov, BoA Moiseenko, VB Pavlovich, EG Ponomarev, ND Tyufyakov, AS Shtan', and VS Yaskevich. Pu^{238}-Be neutron sources. *Soviet Atomic Energy*, 25(6):1375–1376, 1968.

[51] M. Moszyński, M. Kapusta, D. Wolski, W. Klamra, and B. Cederwall. Properties of the YAP:Ce scintillator. *Nuclear Instruments and Methods in Physics Research Section A: Accelerators, Spectrometers, Detectors and Associated Equipment*, 404(1):157–165, 1998.

[52] Hamamatsu Photonics. `http://www.hamamatsu.com`.

[53] Scionix Holland BV. `http://www.scionix.nl`.

[54] J. Scherzinger, J.R.M. Annand, G. Davatz, K.G. Fissum, U. Gendotti, R. Hall-Wilton, E. Håkansson, R. Jebali, K. Kanaki, M. Lundin, B. Nilsson, A. Rosborge, and H. Svensson. Tagging fast neutrons from an ^{241}Am/^{9}Be source. *Applied Radiation and Isotopes*, 98:74–79, 2015.

[55] EJ-520 – reflective paint for liquid scintillator cell. `http://www.ggg-tech.co.jp/maker/eljen/ej-520.html`.

[56] BOROFLOAT. `https://www.schott.com/en-gb/products/borofloat`. Supplied by Glasteknik i Emmaboda AB, Utvägen 6 SE-361 31 Emmaboda, Sweden.

[57] Araldite 2000. `http://www.araldite2000plus.com`. Araldite is a registered trademark of Huntsman.

[58] Viton o-rings. `https://www.oringsusa.com/o/viton/`. Viton is a registered trademark of DuPont Performance Elastomers LLC.

[59] Poly-methyl-methacrylate, also known as PMM, acrylic, plexiglass, and lucite. Supplied by Nordic Plastics Group AB, Bronsyxegatan 6, SE-213 75 Malmoe, Sweden.

[60] EJ-510 – reflective paint for light guides. `https://eljentechnology.com/products/accessories/ej-510`.

[61] 9821B series photomultiplier. `https://et-enterprises.com/images/data_sheets/9821B.pdf`.

[62] J. Scherzinger, R. Al Jebali, J.R.M. Annand, K.G. Fissum, R. Hall-Wilton, S. Koufigar, N. Mauritzson, F. Messi, H. Perrey, and E. Rofors. A comparison of untagged gamma-ray and tagged-neutron yields from ^{241}AmBe and ^{238}PuBe sources. *Applied Radiation and Isotopes*, 127:98–102, 2017.

[63] R. Jebali, J. Scherzinger, J.R.M. Annand, R. Chandra, G. Davatz, K.G. Fissum, H. Friederich, U. Gendotti, R. Hall-Wilton, E. Håkansson, K. Kanaki, M. Lundin, D. Murer, B. Nilsson, A. Rosborg, and H. Svensson. A first comparison of the responses of a 4He-based fast-neutron detector and a NE-213 liquid-scintillator reference detector. *Nuclear Instruments and Methods in Physics Research Section A: Accelerators, Spectrometers, Detectors and Associated Equipment*, 794:102–108, 2015.

[64] J. Scherzinger, R. Al Jebali, J. R M Annand, K. G. Fissum, R. Hall-Wilton, K. Kanaki, M. Lundin, B. Nilsson, H. Perrey, A. Rosborg, and H. Svensson. "The light-yield response of a NE-213 liquid-scintillator detector measured using 2–6 MeV tagged neutrons. *Nuclear Instruments & Methods in Physics Research. Section A: Accelerators, Spectrometers, Detectors, and Associated Equipment*, 840:121–127, December 2016.

[65] CAEN. VX1751 4/8 Channel 10 bit 2/1 GS/s Digitizer. https://www.caen.it/products/vx1751/.

[66] CAEN. N858 Dual Attenuator. https://www.caen.it/products/n858/.

[67] R.O. Owens. Statistical treatment of tagged photon experiments. *Nuclear Instruments and Methods in Physics Research Section A: Accelerators, Spectrometers, Detectors and Associated Equipment*, 288(2):574–584, 1990.

[68] Julius Scherzinger, Ramsey Al Jebali, JRM Annand, KG Fissum, Richard Hall-Wilton, Sharareh Koufigar, Nicholai Mauritzson, Francesco Messi, Hanno Perrey, and Emil Rofors. A comparison of untagged gamma-ray and tagged-neutron yields from ^{241}AmBe and ^{238}PuBe sources. *Applied Radiation and Isotopes*, 127:98–102, 2017.

[69] Thomas M Carsey and Jeffrey J Harden. *Monte Carlo simulation and resampling methods for social science*. Sage Publications, 2013.

[70] Peter Jäckel. *Monte Carlo methods in finance*, volume 2. J. Wiley, 2002.

[71] S. Agostinelli, J. Allison, K. Amako, J. Apostolakis, H. Araujo, P. Arce, M. Asai, D. Axen, S. Banerjee, G. Barrand, F. Behner, L. Bellagamba, J. Boudreau, L. Broglia, A. Brunengo, H. Burkhardt, S. Chauvie, J. Chuma, R. Chytracek, G. Cooperman, G. Cosmo, P. Degtyarenko, A. Dell'Acqua, G. Depaola, D. Dietrich, R. Enami, A. Feliciello, C. Ferguson, H. Fesefeldt, G. Folger, F. Foppiano, A. Forti, S. Garelli, S. Giani, R. Giannitrapani, D. Gibin, J.J. Gómez Cadenas, I. González, G. Gracia Abril, G. Greeniaus, W. Greiner, V. Grichine, A. Grossheim, S. Guatelli, P. Gumplinger, R. Hamatsu, K. Hashimoto, H. Hasui, A. Heikkinen, A. Howard, V. Ivanchenko, A. Johnson, F.W. Jones, J. Kallenbach, N. Kanaya, M. Kawabata, Y. Kawabata, M. Kawaguti, S. Kelner, P. Kent, A. Kimura, T. Kodama, R. Kokoulin, M. Kossov, H. Kurashige, E. Lamanna, T. Lampén, V. Lara, V. Lefebure, F. Lei, M. Liendl, W. Lockman, F. Longo, S. Magni, M. Maire, E. Medernach, K. Minamimoto, P. Mora de Freitas, Y. Morita, K. Murakami, M. Nagamatu, R. Nartallo, P. Nieminen, T. Nishimura, K. Ohtsubo, M. Okamura, S. O'Neale, Y. Oohata, K. Paech, J. Perl, A. Pfeiffer, M.G. Pia, F. Ranjard, A. Rybin, S. Sadilov, E. Di Salvo, G. Santin, T. Sasaki, N. Savvas, Y. Sawada, S. Scherer, S. Sei, V. Sirotenko, D. Smith, N. Starkov, H. Stoecker, J. Sulkimo, M. Takahata, S. Tanaka, E. Tcherniaev, E. Safai Tehrani, M. Tropeano, P. Truscott, H. Uno, L. Urban, P. Urban, M. Verderi, A. Walkden, W. Wander, H. Weber, J.P. Wellisch, T. Wenaus, D.C. Williams, D. Wright, T. Yamada, H. Yoshida, and D. Zschiesche. Geant4—a simulation toolkit. *Nuclear Instruments and Methods in Physics Research Section A: Accelerators, Spectrometers, Detectors and Associated Equipment*, 506(3):250 – 303, 2003.

[72] A. Le Postollec, S. Incerti, M. Dobrijevic, L. Desorgher, G. Santin, P. Moretto, O. Vandenabeele-Trambouze, G. Coussot, L. Dartnell, and P. Nieminen. Monte

Carlo Simulation of the Radiation Environment Encountered by a Biochip During a Space Mission to Mars. *Astrobiology*, 9(3):311–323, 2009. PMID: 19368517.

[73] S. Incerti, I. Kyriakou, M. A. Bernal, M. C. Bordage, Z. Francis, S. Guatelli, V. Ivanchenko, M. Karamitros, N. Lampe, S. B. Lee, S. Meylan, C. H. Min, W. G. Shin, P. Nieminen, D. Sakata, N. Tang, C. Villagrasa, H. N. Tran, and J. M. C. Brown. Geant4-DNA example applications for track structure simulations in liquid water: A report from the Geant4-DNA Project. *Medical Physics*, 45(8):e722–e739, 2018.

[74] J. Allison, K. Amako, J. Apostolakis, H. Araujo, P. Arce Dubois, M. Asai, G. Barrand, R. Capra, S. Chauvie, R. Chytracek, G. A. P. Cirrone, G. Cooperman, G. Cosmo, G. Cuttone, G. G. Daquino, M. Donszelmann, M. Dressel, G. Folger, F. Foppiano, J. Generowicz, V. Grichine, S. Guatelli, P. Gumplinger, A. Heikkinen, I. Hrivnacova, A. Howard, S. Incerti, V. Ivanchenko, T. Johnson, F. Jones, T. Koi, R. Kokoulin, M. Kossov, H. Kurashige, V. Lara, S. Larsson, F. Lei, O. Link, F. Longo, M. Maire, A. Mantero, B. Mascialino, I. McLaren, P. Mendez Lorenzo, K. Minamimoto, K. Murakami, P. Nieminen, L. Pandola, S. Parlati, L. Peralta, J. Perl, A. Pfeiffer, M. G. Pia, A. Ribon, P. Rodrigues, G. Russo, S. Sadilov, G. Santin, T. Sasaki, D. Smith, N. Starkov, S. Tanaka, E. Tcherniaev, B. Tome, A. Trindade, P. Truscott, L. Urban, M. Verderi, A. Walkden, J. P. Wellisch, D. C. Williams, D. Wright, and H. Yoshida. Geant4 developments and applications. *IEEE Transactions on Nuclear Science*, 53(1):270–278, 2006.

[75] R.L. Craun and D.L. Smith. Analysis of response data for several organic scintillators. *Nuclear Instruments and Methods*, 80(2):239–244, 1970.

[76] RE Pywell, BD Sawatzky, J Ives, NR Kolb, R Igarashi, and WA Wurtz. Light output response of BC-505 liquid scintillator. *Nuclear Instruments and Methods in Physics Research Section A: Accelerators, Spectrometers, Detectors and Associated Equipment*, 565(2):725–730, 2006.

[77] Tomáš Novotny. Photon spectrometry in mixed neutron-photon fields using NE 213 liquid scintillation detectors. Technical report, Physikalisch-Technische Bundesanstalt, 1997.

[78] N.V. Kornilov, I. Fabry, S. Oberstedt, and F.-J. Hambsch. Total characterization of neutron detectors with a ^{252}Cf source and a new light output determination. *Nuclear Instruments and Methods in Physics Research Section A: Accelerators, Spectrometers, Detectors and Associated Equipment*, 599(2):226–233, 2009.

[79] EJ-301 – Eljen Technoloy. `https://eljentechnology.com/products/liquid-scintillators/ej-301-ej-309`.

[80] Geant4 book for application developers (2020) Release 10.6. `http://geant4-userdoc.web.cern.ch/geant4-userdoc/UsersGuides/ForToolkitDeveloper/fo/BookForToolkitDevelopers.pdf`.

[81] Peter Gumplinger. Optical photon processes in Geant4. *Users' Workshop at CERN*, 2002.

[82] Refractive index database. `https://refractiveindex.info/`.

[83] Project Jupyter. `https://jupyter.org/`.

[84] Python 3.8.5. `https://www.python.org/`.

Scientific publications

Author Contributions

Paper I: The neutron tagging facility at Lund University

N. Mauritzson: Methodology, Conceptualization, Investigation, Fabrication, Software, Validation, Data Curation, Visualization, Review & Editing

Paper II: GEANT4-based calibration of an organic liquid scintillator

N. Mauritzson: Conceptualization, Methodology, Software, Validation, Formal analysis, Investigation, Data Curation, Writing, Original Draft, Review & Editing, Visualization, Project administration

Paper III: Technique for the measurement of intrinsic pulse-shape discrimination for organic scintillators using tagged neutrons

N. Mauritzson: Conceptualization, Methodology, Software, Validation, Formal analysis, Investigation, Data Curation, Writing, Original Draft, Review & Editing, Visualization, Project administration

Paper IV: Light-yield response of liquid scintillators using $2-6\,\mathrm{MeV}$ tagged neutrons

N. Mauritzson: Conceptualization, Methodology, Software, Validation, Formal analysis, Investigation, Data Curation, Writing, Original Draft, Review & Editing, Visualization, Project administration

Paper 1

THE NEUTRON-TAGGING FACILITY AT LUND UNIVERSITY

F. MESSI, H. Perrey, K. Fissum, D.D. DiJulio, E. Karnickis, V. Maulerova, N. Mauritzson, E. Rofors,
Division of Nuclear Physics, Lund University and
European Spallation Source ERIC
Lund, Sweden
Email: francesco.messi@nuclear.lu.se

A. Huusko, T. Ilves, A. Jalgén, S. Koufigar, H. Söderhielm, D. Söderström
Division of Nuclear Physics, Lund University
Lund, Sweden

R. Hall-Wilton
European Spallation Source ERIC
Lund and
Mid-Sweden University
Sundsvall, Sweden

P. Bentley, C.P. Cooper-Jensen, J. Freita-Ramos, F. Issa, K. Kanaki, A. Khaplanov, G. Mauri, F. Piscitelli, I. Stefanescu
European Spallation Source ERIC
Lund, Sweden

J. Scherzinger
Department of Physics, University of Pisa
Pisa, Italy

R. Al Jebali
European Spallation Source ERIC
Lund, Sweden and
School of Physics and Astronomy, Glasgow University,
Glasgow, UK

J.R.M. Annand, L. Boyd
School of Physics and Astronomy, Glasgow University,
Glasgow, UK

M. Akkawi, W. Pei
University of Toronto,
Toronto, Canada

Abstract

Over the last decades, the field of thermal neutron detection has overwhelmingly employed He-3-based technologies. The He-3 crisis together with the forthcoming establishment of the European Spallation Source have necessitated the development of new technologies for neutron detection. Today, several promising He-3-free candidates are under detailed study and need to be validated. This validation process is in general long and expensive. The study of detector prototypes using neutron-emitting radioactive sources is a cost-effective solution, especially for preliminary investigations. That said, neutron-emitting sources have the general disadvantage of broad, structured, emitted-neutron energy ranges. Further, the emitted neutrons often compete with unwanted backgrounds of gamma-rays, alpha-particles, and fission-fragments. By blending experimental infrastructure such as shielding to provide particle beams with neutron-detection techniques such as tagging, disadvantages may be converted into advantages. In particular, a technique known as tagging involves exploiting the mixed-field generally associated with a neutron-emitting source to determine neutron time-of-flight and thus energy on an event-by-event basis. This allows for the definition of low-cost, precision neutron beams. The Source-Testing Facility, located at Lund University in Sweden and operated by the SONNIG Group of the Division of Nuclear Physics, was developed for just such low-cost studies. Precision tagged-neutron beams derived from radioactive sources are available around-the-clock for advanced detector diagnostic studies. Neutron measurements performed at the Source Testing Facility are thus cost-effective and have a very low barrier for entry. In this paper, we present an overview of the project.

1.   INTRODUCTION

Neutrons of all energies are important probes of matter. The precise detection of neutrons emerging from a sample under study is crucial to the quality of the resulting experimental data. Until recently, He-3-based technologies were essentially the only method used for neutron detection. The recent He-3-crisis [1,2] and the proposal of the European Spallation Source (ESS) [3, 4] have led to an aggressive search for alternative technologies [5]. Together, the prohibitive cost of He-3 and the design goals for the new facility with its extremely high flux of neutrons call for completely new concepts for detectors [6] and shielding [7]. Strong candidates for new detector technologies exist, but few of these have been characterized properly. Most are still in their developmental infancy and need to be precisely validated. In general, the validation of a new detector technology is a two-step process: first, wide-ranging irradiations are performed using neutron-emitting radioactive sources, where the cost per neutron is low; and second, promising technologies are then precisely irradiated at neutron-beam facilities, where the cost per neutron is substantially higher. We note that the cost per neutron at a neutron-beam facility can be so high that it may be prohibitively expensive. A facility based upon neutron-emitting radioactive sources is thus a cost-effective solution to this problem with a relatively low entry threshold. Once the sources and necessary infrastructure are in place, "natural" neutrons are available around the clock. Thus, the overhead for initially benchmarking new technology will not be dominated by beam-time associated costs. Further, by instrumenting a source facility with well understood shielding and equipment to take advantage of nuclear-physics knowledge associated with the particular radioactive decay in question, low-cost polychromatic beams of neutrons may be created.

At the Division of Nuclear Physics at Lund University [8], the internationally accessible Source-Testing Facility (STF) [9] facility has been constructed to provide precision beams of neutrons from radioactive sources. Thus, a cost-effective solution for performing advanced detector diagnostics already exists and is in fact routinely employed by its users. The STF has been instrumented to provide all the tools necessary for the initial characterization of newly developed detectors and shielding materials to its users.

2.   THE SOURCE TESTING FACILITY

Constructed at the Division of Nuclear Physics at Lund University in collaboration with the Detector Group [10] at ESS, the STF is operated by the SONNIG group [11]. It is a fully equipped user facility. The STF boasts a complete range of neutron and gamma-ray sources for the characterizations of detectors and is also equipped with several detectors, detector-associated infrastructure and IT, as well as the electronic components essential to the needs of a user-focused laboratory. As there are no reactors or accelerators involved, the STF is available continuously for prototype development and commissioning. Figure 1 shows an overview of the facility.
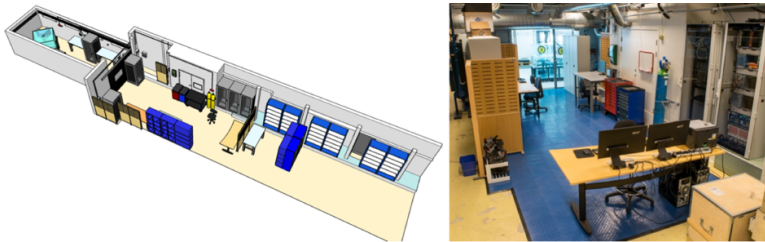
Figure 1: The STF. On the left, a 3D-rendering and on the right, a photo.

The key infrastructure available at the STF includes:

- **Sources**: several mixed-field Actinide-Beryllium sources, a fission neutron source as well as gamma-ray sources. In particular, ^{241}Am-Be, ^{238}Pu-Be and ^{252}Cf (thin window) sources are available as well as ^{57}Co, ^{60}Co, ^{137}Cs, ^{22}Na and ^{133}Ba sources for gamma-ray radiation.

- **Detectors:** - a full set of detectors, both commercially provided and in-house developed, for background monitoring, gamma-ray detection and fast- and thermal-neutron detection. The detector pool of the STF includes plastic and liquid scintillators, gas detectors (He-3 tube, He-4 cells), solid-boron detectors, inorganic crystal scintillators (such as 1.5" CeBr$_3$ and LaBr$_3$ as well as a 12" NaI) and boron-straw tubes, to name a few. Example of detectors available at the STF are shown in Figure 2.

Figure 2: Example of detectors available at the STF. From the left, two plastic scintillator paddles read out by PMTs, one He-4 cell (operated at 5 atm) read out by a 2" PMT, a He-3 tube (calibrated efficiency of 96.1% at 2.5Å) and two NE213 liquid scintillator (0.43 and 4.5 l) read out by a 3" PMT.

- **The Aquarium**: a custom-designed shielding apparatus for neutron sources, delivering if desired beams of "tagged" neutrons[1] (see Figure 3). The Aquarium consist of a 3-section cube of Plexiglas (~1.4 m side), filled with about 2650 l of high-purity water. It is designed to host a neutron source in its centre, together with four gamma-ray sensitive detectors. The dose-rate on the external surface of the cube is < 0.5 μSv/h when an industry standard 18.5 GBq ^{241}Am-Be source is encapsulated. Four horizontal cylindrical apertures of ~17 cm in diameter act as "beam guides", one perpendicular to each of the four vertical faces of the cube, providing four uniform but combined beams of gamma-rays and neutrons from the source.
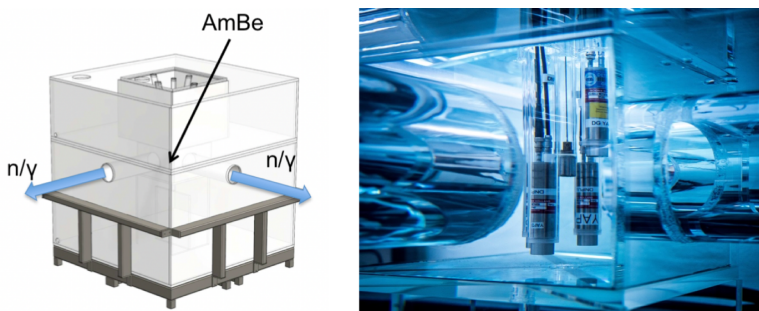
Figure 3: The Aquarium. On the left, a CAD drawing and on the right, a photo of the inner chamber of the Aquarium. The neutron source surrounded by four gamma-ray detectors as well as two of the four beam ports may be seen.

- **A black-box**: a light-tight enclosure for testing light-sensitive detectors such as open photo-multiplier tubes (PMTs) (see Figure 4). The enclosure will eventually contain an optical table with a 1 m^2 work surface. One end of the enclosure will house servo stages which can either carry a calibrated laser emitter or radioactive sources. These servo stages will allow for the mapping of the topological response of areal detectors such as multi-anode PMTs.

---

[1] The neutron-tagging technique is described in detail in Sec. 3.
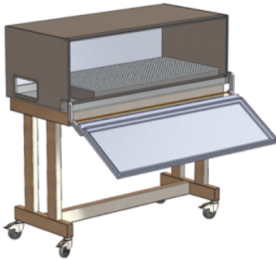
Figure 4: The black-box at the STF. On the left, a CAD drawing of the apparatus under construction and on the right, a photo of the existing prototype. The light-tight box may be surrounded by modular shielding.

- **Electronics and computers**: the STF is equipped with a comprehensive set of electronics modules and computers. The facility is designed to be modular and flexible, so that users can bring their own equipment or use the available infrastructure in any combination. This includes analog NIM, CAMAC and VME modules (discriminators, QDCs, TDCs, visual scalers, etc...) as well as more modern digitizers (see Figure 5). Several computers are also available to be connected to the experimental setup under consideration to acquire data from the detectors.

Figure 5: A subset of the electronics modules available at the STF.

- **Shielding materials:** such as plastic or lead bricks, as well as borated-Al plates and various geometries of borated-plastic material. These may be used to optimise experimental setups.

- **Acquisition and analysis software** are both available, in particular a pair of ROOT-based DAQs [12]. The DAQs may be employed to collect data and to provide a first analysis (see Figure 6). Commercial software is also available for various MCA and Digitizer modules.
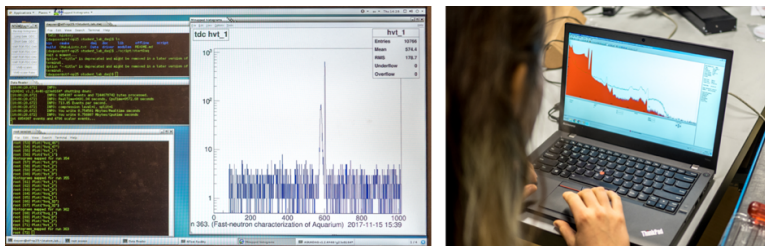
Figure 6: DAQs running at the STF. On the left, a screen shot of a ROOT-based DAQ and on the right, a student using the MCA software.

- **Simulation tools**, based on GEANT4 [13] and included in the simulation framework of the ESS [14, 15, 16], have been developed to characterize the Aquarium and the sources. They are intended to be used to facilitate understanding of features within data that would be difficult to study in real life.

- **SONNIG expertise.** The group members are available for consulting and support. They are highly experienced with the set-up of the experiment and/or the optimization of the DAQs and with how to use the analysis software. Experience with the setup is gladly shared and help with optimizing acquisition software as well as data analysis can be provided.

3. TAGGING NEUTRONS

Employing radioactive sources for detector characterizations can be advantageous to the user. For example, once the setup is optimised and the acquisition of data is started, in contrast to accelerator-based measurements, no further assistance is needed and no night shifts are required. A disadvantage of employing radioactive sources is that the emitted neutrons have a wide range of energies that are not uniform. The ISO 8529-2 recommended neutron-energy spectrum from [241]Am-Be is shown in Figure 7. As can be seen, the emitted neutrons are definitely not mono-energetic. Moreover, any neutron-emitting source likely emits a mixed field of gamma-rays, alpha-particles and neutrons.
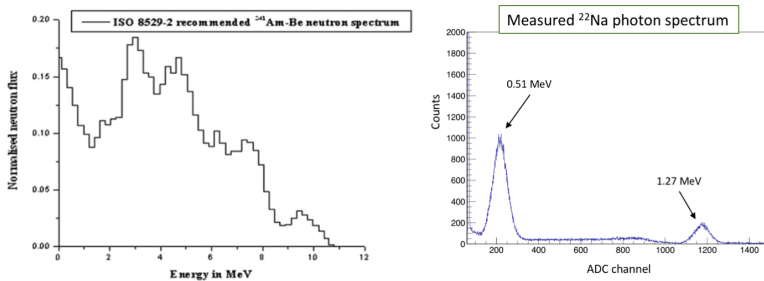
Figure 7: Spectra from sources. On the left, the ISO 8529-2 recommended neutron spectrum for a ^{241}Am-Be source and on the right, a measured gamma-ray-spectrum for a ^{22}Na source.

Further, neutron sources generally radiate mixed field isotropically. Due to the mixed field, the wide energy spectrum of the released neutrons, and the randomness of the underlying decay processes, direct-exposure irradiations offer a less controlled environment compared to a reactor beam line. Clearly, such a beam line may be carefully tuned to provide a continuous mono-energetic beam of neutrons. However, by precisely measuring the radiation field on an event-by-event basis, one can reconstruct the properties of each individual neutron and thereby "tag" the neutrons. The process involves determining the time-of-flight (ToF) and thus the energy of each detected neutron [17, 18].

In a source, such Am-Be, fast neutrons are emitted via the reaction

$$\alpha + {}^9Be \rightarrow {}^{12}C + n$$
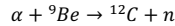
The recoiling ^{12}C is left in its first exited state about 55% of the time and the emitted neutron is accompanied by the prompt emission of a 4.44 MeV gamma-ray from the instantaneous de-excitation of the ^{12}C to its ground state. If both the neutron and the gamma-ray are detected, the ToF and thus kinetic energy of the neutron may be determined on an event-by-event basis (see Figure 8).
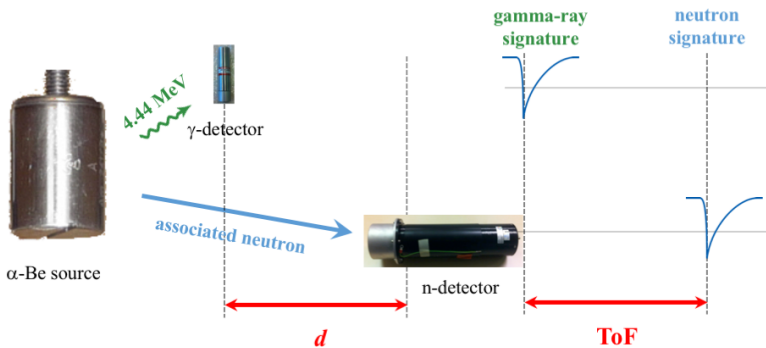
Figure 8: Neutron-Tagging technique. A 4.44 MeV gamma-ray is measured in conjunction with the associated emitted neutron. From the time difference between the detection of the two particles, the ToF of the neutron can be determined and thus its energy may be calculated.

67

In our case, the relative timing between the detection of the gamma-ray by an Yttrium Aluminum Perovskite (YAP) inorganic crystal-scintillator detector and the detection of the neutron by an organic liquid-scintillator detector is measured, resulting in the spectrum shown in Figure 9. For every event, the ToF of the detected neutron can be determined and thus, knowledge of the source-to-detector distances facilitates the calculation of the neutron energy. The setup is self-calibrating thanks to physical events where two gamma-rays are emitted simultaneously by the source. These events both travel the well-known distances involved at the speed of light, and result in a gamma-flash in the ToF spectrum. The gamma-flash provides a reference point from which the instant of the double gamma-ray emission may be determined. In general, the source and YAP detectors are placed inside the central chamber of the Aquarium, while the neutron detector is placed at one of the beam ports.
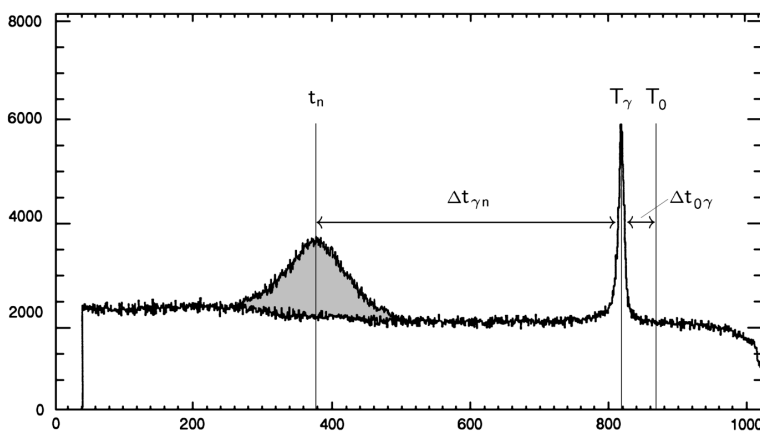
Figure 9: TDC spectrum of tagged fast neutrons (TDC channels vs number of counts). An entry is the time between the start signal from the neutron detector and the stop signal from the gamma-ray detector. The gamma-flash is at T_γ, while the neutron distribution is at t_n. The indicated T_0-position is the reconstructed time of the actual decay. Figure from [19].

With these techniques, the STF is presently capable of measuring the response of detectors to fast neutrons, fast-neutron detection efficiency and the neutron and gamma-ray attenuation properties of shielding materials (tagged neutron energy between 1 and 6 MeV). Note that a major upgrade of the Aquarium and the electronics available at the facility have recently been funded via the Lund University Natural Science Faculty. Together with a corresponding upgrade of the data-acquisition systems, we anticipate a first attempt to tag neutrons of energies in the thermal region ($\sim$ 25 meV) to commence very soon.

4.   EXAMPLES FOR RECENT STUDIES PERFORMED AT THE STF

Highlights of recent results obtained by various user groups of the STF are presented below.

4.1.   CHARACTERIZATION OF SOURCES

All of our neutron sources have been systematically characterized in-situ (see Figure 10), providing important validation benchmarks for our experimental infrastructure [20, 21]. This program of systematic characterization was deemed important since the sources were to be provided to a user community. Requiring each group in this user community to individually study the sources they were provided was felt to be unreasonably inefficient. The tagging technique has been extended to a Cf-252 fission fragment source [22]. For this, the single-sided Cf-252 source was positioned within a gaseous He-4 scintillator detector in which light and heavy fission fragments corresponding to neutron emission were detected as tags. Since the emission spectrum for Cf-252 is exceptionally well-known, an excellent benchmark exists from which it is anticipated the neutron-detection efficiency of a detector can be unfolded.
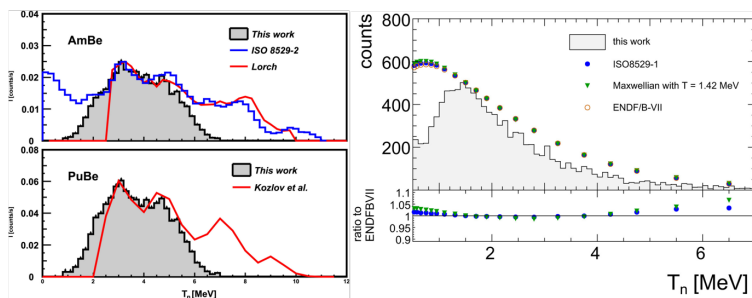
Figure 10: Spectra of sources measured at the STF. On the left, the measured spectra of the AmBe (top) and PuBe (bottom) sources (plots from [21]) and on the right, the measured spectrum of the Cf source (plot from [22]).

4.2. CHARACTERIZATION OF DETECTORS

The STF is ideal for the development of prototypes in preparation for tests at nuclear reactors or on real spallation instruments. It is anticipated that a very large subset of ESS detector prototypes will see the neutrons of the STF at some stage of their development (as the case for the Multi-Grid [23], to cite one). Using either direct irradiation or the tagging technique, simple functionality tests of detector prototypes may be performed. Further, the sensitivity of a prototype to fast-neutron or gamma-ray backgrounds may be investigated. Examples of the latter are recent studies performed on commercially available beam monitors [24] or on the Multi-Blade [25] detector (see Figure 11). The Multi-Blade detector is being developed for reflectometry instruments at ESS.

A recently developed black-box (recall Figure 4), to be equipped with a servo stages on an optical table, has been used to characterize Multi-Anode PMTs for the SoNDe project [26]. The SoNDe project is focused on the development of pixilated, solid-state neutron detectors for ESS.
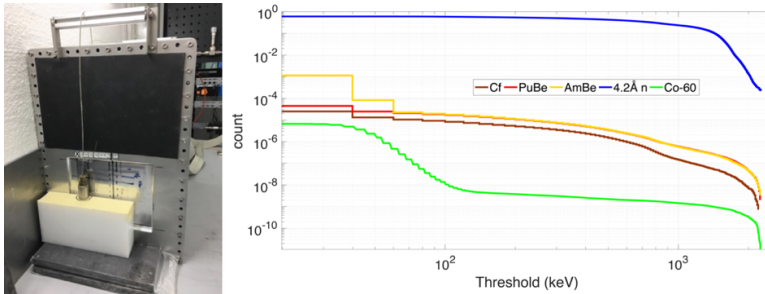
Figure 11: Fast-neutron sensitivity measurement on the Multi-Blade detector: an example of untagged irradiation measure for detector characterization at STF. On the left, a photo of the detector irradiated by the PuBe source at STF and on the right, the cumulative number of counts as function of an energy threshold for different incoming radiations, normalised to the sensitivity of the detector to thermal neutrons (4.2Å). (Plot from [27]).

4.3.   CHARACTERIZATION OF SHIELDING

The potential of the STF is not limited to the development of new neutron instrumentation. Using its tagged-neutron beams, the behavior of materials under neutron or gamma-ray irradiation may be studied in detail [28]. This is a research domain traditionally addressed at reactors or spallation sources which has recently been invigorated with the promise of proton therapy in treating cancer. We investigated radiation attenuation in steel, copper, Polyethylene (PE) and both regular and PE/B_4C-enriched concrete samples using the Aquarium (see Figure 12). Measured transmission spectra of tagged neutrons were compared to simulation with a very high level of agreement (see Figure 13).

Figure 12: Radiation attenuation in shielding material measurements. Transmission measurements were performed.

70
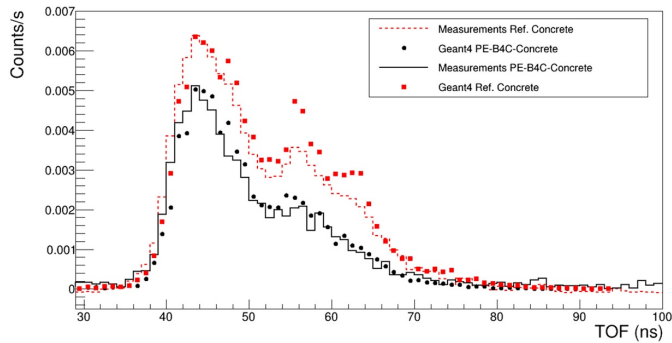
Figure 13: A comparison of measurements and simulations for reference concrete and PE-B₄C-concrete. (Plot from [28]).

4.4. EDUCATION

As part of Lund University infrastructure, the STF has been used extensively for student training at all levels. Table 1 shows a list of thesis work performed to date.

Name of Student	Type of thesis	Institution	Date	Title
Amanda Jalgén	Master	LTH	September 12, 2017	Initial Characterizations of a Pixelated Thermal-Neutron Detector
Laura Boyd	Summer	University of Glasgow	September 8, 2017	Initial Testing of the Response of a Pixelated Thermal-Neutron Detector
Mohamad Akkawi	Summer	University of Toronto	June 13, 2017	Photon Detection Using Cerium Bromide Scintillation Crystals
Nicholai Mauritzson	Master	LU	June 9, 2017	Design, Construction and Characterization of a Portable Fast-Neutron Detector
Henrik Söderhielm	Under-graduate	LU	February 3, 2017	Two-Dimensional Radiation Field Map of a Be-based Source
Julius Scherzinger	PhD	LU	December 16, 2016	Neutron Irradiation Techniques
Emil Rofors	Master	LTH	March 14, 2016	Fast Photoneutron Production
Sharareh Koufigar	Under-graduate	LU	October 21, 2015	The Radiological Footprint of a Be-based Source
Julius Scherzinger	Licentitate	LU	March 20, 2015	A Source-Based Testbed for Fast-Neutron Irradiation

Table 1: STF theses. (for a complete description, please visit http://www.nuclear.lu.se/english/research/neutronfysik/).

5.   SUMMARY

Located at the Department of Physics of Lund University, the Source-Testing Facility has been designed for advanced detector and material diagnostics. Being a user facility, the STF offers a complete set of infrastructure, including gamma-ray and neutron sources, shielding, detectors, computers and IT. Furthermore, acquisition, analysis, and simulation software, and support are offered by the SONNIG group, who operate the facility. Until now, the STF has been used almost exclusively for the development of He-3 free neutron detectors and the study of advanced neutron shielding. The STF offers the potential of a low cost, low barrier to entry, and low flux neutron source, that has potential applications beyond those utilised presently. The hands-on training of the next generation of neutron scientists is a high priority. If you are in need of neutrons, contact us. We are happy to provide access to the STF and support your measurements with consultations and hands-on support during beam-time.

- http://www.nuclear.lu.se/english/research/neutronfysik/
- https://europeanspallationsource.se/workshops-facilities#source-testing-facility
- stf@nuclear.lu.se
- Source Testing Facility c/o
  Lund University
  Department of Physics
  Division of Nuclear Physics
  P.O Box 118
  SE-221 00 Lund
  Sweden

REFERENCES

[1] SHEA D.A. and MORGAN D., "The Helium-3 shortage: supply, demand, and options for congress", Technical Report R41419, Congressional Research Service, (2010).

[2] KOUZES RT., "The 3He Supply Problem." PNNL-18388 Pacific Northwest National Laboratory, Richland, WA, (2009).

[3] LINDROOS M. et al., "The European Spallation Source", In Nuclear Instruments and Methods in Physics Research Section B, Volume 269, Issue 24 (2011), Pages 3258-3260, ISSN 0168-583X, https://doi.org/10.1016/j.nimb.2011.04.012. (http://www.sciencedirect.com/science/article/pii/S0168583X11003636)

[4] PEGGS S. et al., "European Spallation Source Technical Design Report", ESS-2013-001

[5] HALL-WILTON R. et al, "Detectors for the European spallation source", IEEE Nuclear Science Symposium Conference Record, 4283-4289, (2012). doi:10.1109/NSSMIC.2012.6551977 url: http://ieeexplore.ieee.org/document/6551977/

[6] KIRSTEIN O. et al., "Neutron Position Sensitive Detectors for the ESS", (2014), PoS (Vertex2014) 029 arXiv:1411.6194

[7] CHERKASHYNA N. et al., "High energy particle background at neutron spallation sources and possible solutions", Journal of Physics: Conference Series 528, (2014), doi:10.1088/1742-6596/528/1/012013.

[8] http://www.nuclear.lu.se/english/

[9] https://europeanspallationsource.se/workshops-facilities#source-testing-facility

[10] https://confluence.esss.lu.se/display/DG/Detector+Group

[11] http://www.nuclear.lu.se/english/research/neutronfysik/

[12] BRUN R. and RADEMAKERS F., "ROOT - An Object Oriented Data Analysis Framework", Nucl. Instr. Meth. A, (1996) url: http://root.cern.ch/

[13] AGOSTINELLI S. et al, "Geant4 - a simulation toolkit", Nucl. Instr. Meth. A, (2003) url: http://www.sciencedirect.com/science/article/pii/S0168900203013688

[14] KITTELMANN T. et al, "Geant4 Based Simulations for Novel Neutron Detector Development", 20th International Conference on Computing in High Energy and Nuclear Physics (CHEP), (2013) doi:10.1088/1742-6596/513/2/022017; arXiv:1311.1009v1.

[15] KITTELMANN T. and BOIN M., "Polycrystalline neutron scattering for Geant4: NXSG4", Computer Physics Communications 189, 114-118; (2015). doi:10.1016/j.cpc.2014.11.009.

[16] CAI XX and KITTELMANN T., "NCrystal : A library for thermal neutron transport in crystals", http://mctools.github.io/ncrystal/ v0.9.1, https://doi.org/10.5281/zenodo.855292

[17] SCHERZINGER J., "Neutron Irradiation Techniques", Lund University, Faculty of Science, Department of Physics, (2016) url = http://portal.research.lu.se/portal/en/publications/neutron-irradiation-techniques(d4c447d5-ee52-49a9-ad55-4669aed57e32).html

[18] SCHERZINGER J. et al, "The light-yield response of a NE-213 liquid-scintillator detector measured using 2–6 MeV tagged neutrons", (2016) url = http://www.sciencedirect.com/science/article/pii/S0168900216310361

[19] NILSSON B., "High-resolution Measurement of the ^{4}He (γ, n) Reaction in the Giant Resonance Region", Lund University, Faculty of Science, Department of Physics, (2003) url = http://portal.research.lu.se/portal/en/publications/highresolution-measurement-of-the-4hegn-reaction-in-the-giant-resonance-region(f9873930-d37b-4e4b-b6d0-1acba29ee46e).html

[20] SCHERZINGER J. et al, "Tagging fast neutrons from an ^{241}Am/^{9}Be source", (2015) url = http://www.sciencedirect.com/science/article/pii/S0969804315000044

[21] SCHERZINGER J. et al, "A comparison of untagged gamma-ray and tagged-neutron yields from ^{241}AmBe and ^{238}PuBe sources", (2017) url = http://www.sciencedirect.com/science/article/pii/S0969804316309861

[22] SCHERZINGER J. et al, "Tagging fast neutrons from a ^{252}Cf fission-fragment source", (2017) url = http://www.sciencedirect.com/science/article/pii/S0969804316310521

[23] KHAPLANOV A. et al, "10B multi-grid proportional gas counters for large area thermal neutron detectors", Nucl. Instr. Meth. A, Vol 720, Pag 116-121, (2013), ISSN 0168-9002, https://doi.org/10.1016/j.nima.2012.12.021.

[24] ISSA F. et al, "Characterization of Thermal Neutron Beam Monitors", Phys. Rev. Accel. Beams 20, 092801 (2017) url = https://arxiv.org/abs/1702.01037

[25] PISCITELLI F. et al., "The Multi-Blade Boron-10-based neutron detector for high intensity neutron reflectometry at ESS", JINST, (2017) url = http://iopscience.iop.org/article/10.1088/1748-0221/12/03/P03013/meta;jsessionid=ADCECAD7D2492490212685E84DC81C65.c4.iopscience.cld.iop.org#references

[26] JAKSCH S. et al, "Cumulative Reports of the SoNDe Project July 2017", arXiv preprint arXiv:1707.08679 (2017), url = http://www.fz-juelich.de/jcns/jcns-2/EN/Forschung/Instruments-for-ESS/SoNDe-Projekt/_node.html

[27] MESSI F. et al, "Gamma- and Fast Neutron- Sensitivity of 10B-based Neutron Detectors at ESS", 2017 IEEE Nuclear Science Symposium and Medical Imaging Conference (2017 NSS/MIC)

[28] DIJULIO D. et al, "A polyethylene-B$_4$C based concrete for enhanced neutron shielding at neutron research facilities", (2017) url = http://www.sciencedirect.com/science/article/pii/S0168900217304151
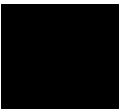
Paper II

Geant4-based calibration of an organic liquid scintillator☆

N. Mauritzson [a], K.G. Fissum [a,*], H. Perrey [a], J.R.M. Annand [c], R.J.W. Frost [a], R. Hall-Wilton [b,c,d], R. Al Jebali [b,c], K. Kanaki [b], V. Maulerova-Subert [a,b,1], F. Messi [a,2], E. Rofors [a]

[a] Division of Nuclear Physics, Lund University, SE-221 00, Lund, Sweden
[b] Detector Group, European Spallation Source ERIC, SE-221 00, Lund, Sweden
[c] SUPA School of Physics and Astronomy, University of Glasgow, Glasgow G12 8QQ, Scotland, UK
[d] Dipartimento di Fisica "G. Occhialini", Università degli Studi di Milano-Bicocca, Piazza della Scienza 3, 20126 Milano, Italy

ARTICLE INFO

ABSTRACT

A light-yield calibration of an NE 213A organic liquid scintillator detector has been performed using both monoenergetic and polyenergetic gamma-ray sources. Scintillation light was detected in a photomultiplier tube, and the corresponding pulses were subjected to waveform digitization on an event-by-event basis. The resulting Compton edges have been analyzed using a GEANT4 simulation of the detector which models both the interactions of the ionizing radiation as well as the transport of scintillation photons. The simulation is calibrated and also compared to well-established prescriptions used to determine the Compton edges, resulting ultimately in light-yield calibration functions. In the process, the simulation-based method produced information on the gain and intrinsic pulse-height resolution of the detector. It also facilitated a previously inaccessible understanding of the systematic uncertainties associated with the calibration of the scintillation-light yield. The simulation-based method was also compared to well-established numerical prescriptions for locating the Compton edges. Ultimately, the simulation predicted as much as 17% lower light-yield calibrations than the prescriptions. These calibrations indicate that approximately 35% of the scintillation light associated with a given gamma-ray reaches the photocathode. It is remarkable how well two 50 year old prescriptions for calibrating scintillation-light yield in organic scintillators have stood the test of time.

1. Introduction

Due to relatively high detection efficiency, strong inherent gamma-ray rejection properties, and fast scintillation pulses, organic liquid scintillators are typically employed to detect fast (MeV) neutrons in mixed neutron and gamma-ray fields. The aromatic organic liquid scintillator NE 213 [1] was originally introduced in the 1960s [2] and poses a non-negligible health risk. However, the excellent intrinsic neutron/gamma-ray pulse-shape discrimination characteristics and high fast-neutron detection efficiency continue to make NE 213 an excellent choice for fast-neutron applications. In this paper, the scintillation-light yield of the more recent NE 213 A version of the liquid is calibrated using the Compton edges in measured energy distributions from a set of gamma-ray sources. This effort has been undertaken as the first step in a systematic program of parametrizing the scintillation-light yields of some recently developed organics and oils.

The analysis of the data has been greatly facilitated by a GEANT4 simulation of the detector apparatus which models the interactions of gamma-rays and secondary electrons as well as the scintillation photon transport.

2. Apparatus

2.1. Gamma-ray sources

Above gamma-ray energy $E_\gamma \sim 100$ keV, the scintillation-light yield produced in organic liquids by atomic electrons freed by interactions with incident gamma-rays is very close to linear [3,4]. The low average Z value typical for organics results in the gamma-ray/electron interactions being dominated by Compton scattering. Above $E_\gamma = 1.022$ MeV, pair production takes over and dominates by ~5 MeV. Measured Compton edges located at energy E_{CE} may be evaluated to calibrate the

Table 1

Gamma-ray sources. "Single" refers to sources where a single gamma-ray was considered, while "double" refers to sources where two gamma-rays were considered.

Source	E_γ [MeV]	E_{CE} [MeV$_{ee}$]	Type
^{22}Na	0.51	0.34	Double
^{137}Cs	0.66	0.48	Single
^{60}Co	1.17	0.96	Double
^{22}Na	1.28	1.06	Double
^{60}Co	1.33	1.12	Double
^{232}Th	2.62	2.38	Single
AmBe	4.44	4.20	Single

Table 2

Properties of NE 213A.

Solvent	Pseudocumene (C_9H_{12})
Flash point	~54 °C
Density	~0.9 g/cm^3
Light output	~75% of anthracene (pristine)
Decay times	~3, ~32, ~270 ns
Wavelength of maximum emission	~420 nm

scintillation-light yield of a detector. Table 1 summarizes the radioactive sources used in this work.

2.2. NE 213 A liquid-scintillator detector

The volatile, corrosive, toxic, pungent, xylene-based scintillator NE 213 has long served as the baseline organic liquid against which all other organics are judged. In this work, the derivative pseudocumene-based scintillator NE 213 A was employed [5]. Table 2 presents some of the well-known properties of NE 213 A.

Fig. 1 shows sketches of the liquid-scintillator detector. The scintillator housing was a 3 mm thick cylindrical aluminum cup 62 mm deep by 94 mm in diameter coated internally with the TiO$_2$-based reflective paint EJ 520 [6]. A 5 mm thick borosilicate glass optical window [7] was attached to the aluminum cell using Araldite 2000+ glue [8]. Together, the cup and the window formed a cell. A ~430 cm^3 volume of NE 213 A was first flushed with nitrogen and then pushed into the cup using a pressurized nitrogen gas-transfer system. Viton O-rings [9] were used to seal the filling penetrations. The filled cell was joined without any optical coupling medium to a 57 mm long by 72.5 mm diameter cylindrical lightguide made from PMMA UVT [10] coated externally with the TiO$_2$-based reflector EJ 510 [11]. The cell/lightguide assembly was joined without any optical coupling medium to an ET type 9821K 3 inch diameter photomultiplier tube (PMT) with a type B voltage divider [12] equipped with a mu-metal magnetic shield and a spring to hold the PMT and PMMA faces in close contact.

2.3. Signals, electronics, and data acquisition

The operating voltage of the detector was set at −2 kV, a voltage employed for this detector in previous VME setups [13–17]. At this voltage, a 1 MeV$_{ee}$ signal had a risetime of ~5 ns, an amplitude of ~900 mV and a falltime of ~60 ns. The data-acquisition system was based on a CAEN VX1751 Waveform Digitizer [18] with a 10 bit ADC and an analog input bandwidth of 500 MHz. The digitizer was configured for a 1 μs acquisition window with 10^9 samples per second over a −1 V dynamic input range. The voltage resolution was ~1 mV. In order to preserve the −2 kV operating voltage used in the previous investigations, it was necessary to attenuate the analog signals from the detector by 16 dB using a CAEN N858 dual attenuator module [19]. Fig. 2 shows a typical waveform. The internal falling-edge threshold was set to −25 mV. The waveform of each pulse was analyzed using a suite of analysis software [20] developed in-house. Analysis of the data was performed using the Python-based [21] code libraries

pandas [22], SciPy [23,24], and numpy [25], where the signal baseline was first subtracted so that the charge corresponding to each scintillation pulse could be determined by integration. The event-timing marker was obtained using a standard zero-crossover method [4]. Voltage sampling was started 25 ns before the event-timing marker and extended to 475 ns after the event-timing marker. Integration was performed offline over this 500 ns window which will be required for neutron/gamma-ray pulse-shape discrimination, resulting in an offline software-based charge-to-digital conversion. The conversion was calibrated to 6.35 ± 5.5% fC/QDC channel using a charge-injection circuit.

2.4. GEANT4 simulation

The response of the detector to gamma-rays was simulated using a C++ Monte Carlo model developed with the GEANT4 toolkit [26]. GEANT4 version 4.10.04 [27] patch 03 (8 February 2019) was employed, with a physics list based on the hadronic class FTFP_BERT_HP and electromagnetic physics classes G4EmStandardPhysics and G4EmExtraPhysics, using a procedure similar to that reported in Ref. [28]. The resulting model was used to simulate the gamma-ray response by modeling the gamma-ray interactions in the detector and tracking the secondary electrons and scintillation photons [29] that they produced. The NE 213 A scintillator was attributed a scintillation light-yield gradient of 1700 scintillation photons per MeV$_{ee}$ (~10% of anthracene) and a Birks parameter of 0.126 mm/MeV. This low scintillation light yield resulted from the work of Scherzinger et al. [15] simulating a NE 213 filled detector. The reduced scintillation-light yield includes scintillator-aging effects, PMT gain, and PMT-aging effects. These photons were then tracked using the optical properties (refractive index, reflectivity, attenuation length) of the components, where they underwent scattering, absorption, and boundary transitions on the journey towards the photocathode. The optical surface model 'glisur' [30,31] was used. The boundaries between the NE 213 A scintillator and the borosilicate glass window of the cup, the glass window and the PMMA UVT lightguide, the lightguide and the PMT window, and the PMT window and the curved photocathode were all assumed to be polished resulting in specular reflection. Scintillation photons that penetrated into the photocathode were converted into photoelectrons (see below). A dielectric-to-dielectric interface was employed at each to account for refraction. In contrast, for the reflective-painted boundary between the scintillator and the aluminum cup as well as the external cylindrical surface of the lightguide, a dielectric-to-metal interface was employed. For the cup, the 'metal' was attributed the optical properties of the reflective paint used. For the lightguide, a 110 μm layer of the paint (corresponding to 3 coats, as per manufacturer specifications) was modeled. Surface irregularities in the paints were addressed using an optical surface model with a 'SetPolish' parameter of 0.1. The dry-fitted boundaries between the cup window and the lightguide as well as the lightguide and the PMT window were taken to be air gaps of 100 μm to account for surface non-planarities. Photon transmission was sensitive to the existence of the air gaps, but relatively insensitive to their widths. When the gap widths were varied from 100 μm to 300 μm, the scintillation-light yield varied by ~1%. At the photocathode, photoelectrons were generated based on the wavelength-dependent quantum efficiency [12], average ~23%. The PMT gain was defined as the scale factor necessary to match the simulated-photoelectron distributions to the measured spectra and was treated as a free parameter. Smearing was applied to match the simulated photoelectron distributions to the measured data in the vicinity of the Compton edge using a least-squares method (see below). It ranged from ~23% at 0.34 MeV$_{ee}$ (^{22}Na) to ~12% at 4.20 MeV$_{ee}$ (AmBe), with an inverse dependence on energy. It includes non-pointlike source, signal-propagation, and electronic noise effects and agrees well with that observed for a very similar detector by Scherzinger et al. [15]
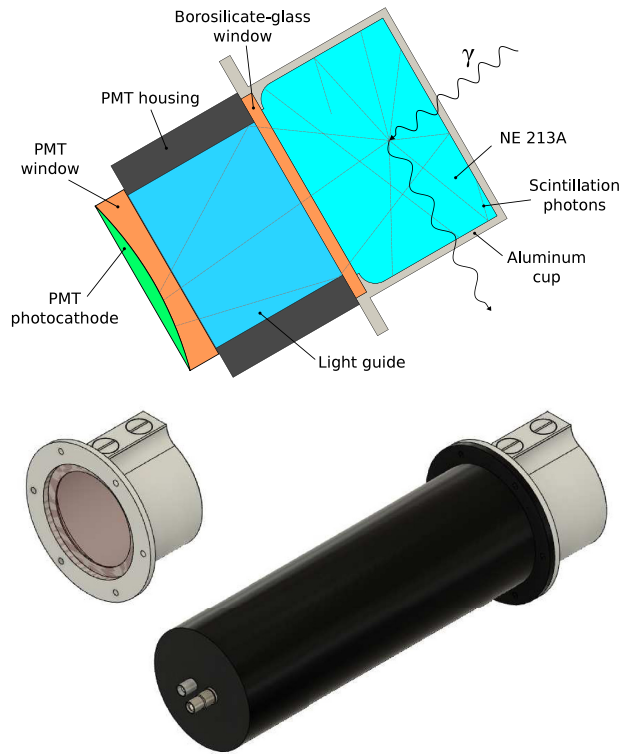
2

Fig. 1. The NE 213 A detector. Top: the cell, lightguide, PMT window, and photocathode. From the right, the NE 213 A scintillator (cyan) was housed inside an aluminum cup (light gray) sealed with a borosilicate-glass window (orange). This window contacted a light guide (light blue) within the PMT housing (black), which in turn contacted the PMT window (orange) and photocathode (green). Middle left: oblique view of the scintillator cell. From the right, the cylindrical cup (light gray) and the circular borosilicate-glass window (light brown). The screws shown on top of the cup facilitated the filling. Bottom right: oblique view of the entire detector. From the right, the cell (light gray) and the μ-metal shielded PMT and base housing (black). Contacts for signal and high voltage (gray) extend to the left from the base of the housing. (For interpretation of the references to color in this figure caption, the reader is referred to the web version of this article.).

3. Measurement

The calibration sources were systematically placed in front of the NE 213 A detector which was aligned so that the cylindrical symmetry axis of the detector pointed at the source. Sources with an activity below 1 MBq (^{22}Na, ^{137}Cs, ^{232}Th) were placed at a distance of 45 cm from the face of the unshielded detector, while the distance was increased to 200 cm for sources with an activity above 1 MBq (^{60}Co, AmBe). Hydrogen-rich materials were removed from the vicinity of the setup to minimize the production of 2.22 MeV gamma-rays from neutron capture during the AmBe irradiations. A typical run time was 1 h. Prior to data collection, background was investigated using a 1.5 inch LaBr^3(Ce) gamma-ray detector. Gamma-rays from the de-excitations of ^{40}K (1.46 MeV) and ^{208}Tl (2.61 MeV, 583 keV, 511 keV) were observed. As count rates were on the order of a few 100 Hz, deadtime was very

low, so that the room background could be subtracted from the source measurement after a straightforward realtime normalization.

4. Results

Fig. 3 compares the GEANT4 simulations and the data in the vicinity of the Compton edges measured from three different sources, each emitting a single, well-defined gamma-ray. As previously mentioned, the gain of the PMT was treated as a free parameter (see Fig. 4), and the simulated photoelectron distribution was matched to the measured data by applying an additional phenomenological smearing, all within a least-squares minimization. Agreement between the simulation and the data for each of the sources is excellent.

Fig. 4 shows the relative PMT gain inferred from matching the GEANT4 simulations obtained with the 1700 scintillation photon per

3
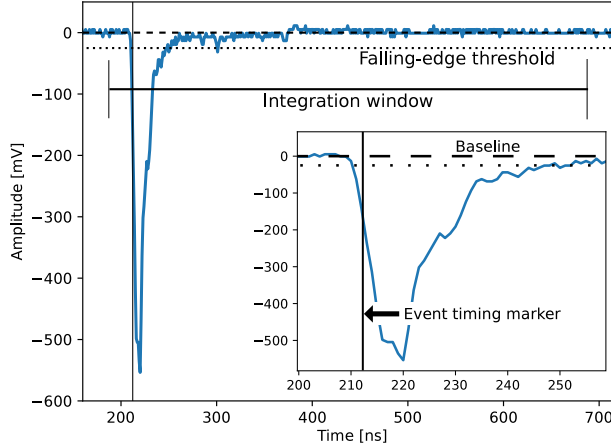
Fig. 2. Signal waveform. The event pulse has a risetime of ~5 ns, an amplitude of ~550 mV and a falltime of ~50 ns. Illustrated are the event-timing marker, the 500 ns integration window opening 25 ns before the event-timing marker, and the −25 mV falling-edge threshold.
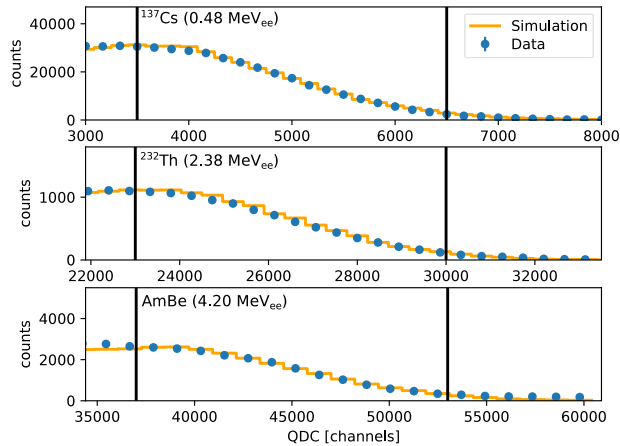
Fig. 3. Replicating Compton edges. Data (filled points) and simulations (open histograms) are shown for three single-energy gamma-ray sources. The solid vertical bars in each panel denote the regions over which the agreement between the simulations and the data was optimized. The statistical uncertainties associated with the data points are smaller than the data points themselves.

MeV_{ee} light-yield gradient and the offline QDC calibration to the data in the vicinity of the Compton edges. The gain of the PMT was taken to be $4 \cdot 10^6$ as per the data sheet. The two close-lying peaks from ^{60}Co are shown as a single data point at an energy of 1.25 MeV_{ee} with an uncertainty (the horizontal error bar) of 80 keV$_{ee}$. The uncertainty in the average relative gain has been taken from the uncertainty produced by the least-squares fitting algorithm. Over the ~5 MeV_{ee} energy region

investigated here, an average relative gain of $(3.27 \pm 0.07) \cdot 10^6$, corresponding to (1388 ± 31) scintillation photons per MeV_{ee}, does a very good job of representing the results. This average gain corresponds to roughly 80% of the 1700 scintillation photon per MeV_{ee} used in the GEANT4 model.

Fig. 5 re-presents the data shown in Fig. 3, but this time in the context of Compton-edge analyses. Here, the well-known prescriptions
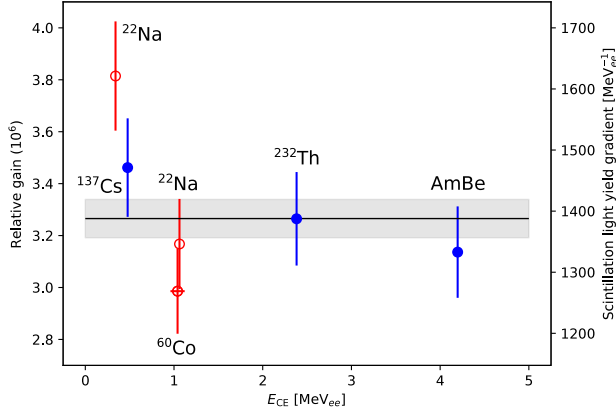
Fig. 4. Inferred relative PMT gain. Gains extracted from matching the GEANT4 simulations to the Compton edges as detailed in Fig. 3 using the 1700 scintillation photon per MeV$_{ee}$ light-yield gradient. Left axis, photoelectron multiplication, right axis, scintillation-light yield. Gains determined from both single-energy (filled circles) and double-energy (open circles) gamma-ray sources are shown (Table 1). The error bars on the data points are dominated by the uncertainty in the QDC charge calibration. The solid line indicates the average relative gain, while the uncertainty in the average value is represented by the shaded band.

for the locations of the Compton edges of Knox and Miller [3] and Flynn et al. [32] are applied directly to the data. Both require that a Gaussian function be fitted to the high-energy side of the measured Compton edge. Flynn et al. associate the location of the half height of the distribution with 104% of E_{CE} while Knox and Miller associate 89% of the full height with 100% of E_{CE}. Note that with more recent input from Monte Carlo simulations, it has become generally accepted that these prescriptions are approximations to the actual location of the Compton edge [15,33–36]. Also shown are the GEANT4 simulations. For each, the same individual PMT gains and phenomenological smearings used to produce Fig. 3 have been employed. Further, a very restrictive cut where only those events with the recoiling electron receiving within 2 keV of the maximum Compton-edge energy has been applied, resulting in an almost pure Compton-edge simulated data set. Gaussian functions were fitted to the entire simulated distributions and the widths of these functions were used to determine the $\pm 3\sigma$ event-summing region used for the calculation of the average peak position. The fitted Gaussians demonstrated the existence of tails in the distributions to lower QDC channels. These tails were energy dependent, ranging from ~0% of the integrated distribution below 1.12 MeV$_{ee}$ to ~14% at 4.20 MeV$_{ee}$. The tails resulted in an energy-dependent percentage difference between the fitted Gaussian mean and the average peak position of up to ~4% at 4.20 MeV$_{ee}$. The locations of the simulated Compton-edge peaks relative to the locations of the Compton edges predicted by the Knox and Miller and Flynn et al. prescriptions are not constant offsets. They vary as a function of gamma-ray energy.

Fig. 6 presents the intrinsic detector resolution extracted from the results of the GEANT4 simulations. The restrictive 2 keV full Compton-edge energy cut is in place. If scintillation-photon statistics dominates the falloff in the energy resolution, the $1/\sqrt{E_{CE}}$ dependence shown is anticipated.

Fig. 7 shows the application of the simulation-based calibration to non-monoenergetic sources. Results obtained for ^{22}Na and ^{60}Co, two sources each emitting two relatively close-lying gamma-rays (759 keV separation for ^{22}Na and 160 keV for ^{60}Co) are shown. The ~22% energy resolution of the detector at these energies renders the methods of Knox and Miller and Flynn et al. difficult to apply, especially in the case of ^{60}Co. By employing the GEANT4 based-calibration method, measured

spectra obtained with these sources may be interpreted in a relatively straightforward manner. In each case, a single simulation of the source employing well-known gamma-ray branching ratios was performed in exactly the method described earlier. For ^{22}Na, 90.2% of decays yield both a 1.27 MeV gamma-ray and a 511 keV gamma-ray whereas 9.7% yield only the 1.27 keV gamma-ray. For ^{60}Co, 99.88% of decays yield both a 1.17 MeV and a 1.33 MeV gamma-ray whereas 0.12% of decays yield only a 1.33 MeV gamma-ray. Agreement between the branched double-energy gamma-ray simulations and the data is again excellent. The corresponding gains and resolutions have already been reported as open circles in Figs. 4 and 6, respectively.

Fig. 8 presents light-output calibrations obtained with linear fits to the data which are summarized in Table 3. The fitted functions shown have been constrained to pass through the origin. The fits do a very good job of linearly replicating the simulated Compton-edge locations as a function of energy. The dominant systematic uncertainty in the data contributing to the uncertainty in the light-output calibration was the ~5.5% uncertainty in the charge calibration of the QDC. Systematic uncertainties arising from the analysis of the simulations included uncertainties arising from the fitted parameters (<3%) and the effects of the various cuts employed in the analysis. The uncertainty due to the various cuts (<1%) was addressed by systematically varying the windows employed. No clear consensus regarding the systematic uncertainty associated with the Knox and Miller and Flynn et al. approaches exists. Systematic uncertainties arising from the fitted parameters and cuts, again <3% and <1% respectively, were consistent with those obtained with the GEANT4 simulations.

Table 4 shows the number of scintillation photons per MeV$_{ee}$ reaching the photocathode unfolded for the three methods for linear fits where the line was constrained to pass through the origin. The Knox and Miller prescription is ~2% larger than the simulated average-value light yield. The Flynn et al. light prescription is ~17% larger than the simulated average-value light yield. Based upon the 1700 scintillation photons per MeV$_{ee}$ light-yield gradient employed in the GEANT4 simulation and the ~80% relative gain, ~35% of the scintillation light produced by a gamma-ray reaches the photocathode.

5
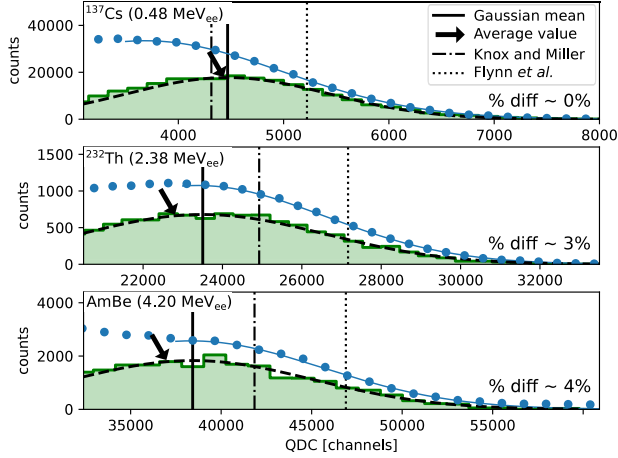
Fig. 5. Scintillation-light yields for three single-energy gamma-ray emitters. Data (filled points) are shown for three single-energy gamma-ray sources together with simulations (shaded histograms) having a restrictive Compton-edge cut. Vertical solid lines illustrate the means of Gaussian distributions (dashed black curves) fitted to the simulated Compton-edge locations. The average values of the shaded histograms are indicated with angled arrows. Vertical dot-dashed lines (Knox and Miller, leftmost) and dotted lines (Flynn et al. rightmost) illustrate the Compton-edge locations extracted from the Gaussian functions fitted directly to the data over the optimization region (thin blue line). The statistical uncertainties associated with the data points are smaller than the data points themselves. (For interpretation of the references to color in this figure caption, the reader is referred to the web version of this article.).
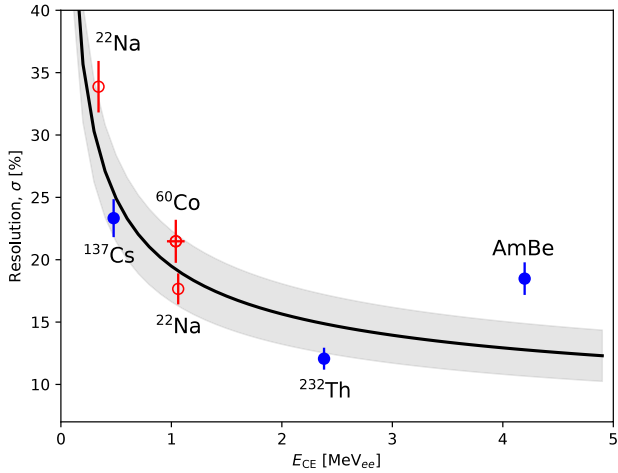
Fig. 6. Resolution (σ). The energy resolution extracted from Gaussian functions fitted to the restrictively cut GEANT4 simulations. Results for single-energy (filled symbols) and double-energy (open symbols) gamma-ray sources are shown. The two close-lying peaks from ^{60}Co are shown as a single data point as in Fig. 4. The error bars on the data points correspond to the quadratic sum of the uncertainties in the mean value and deviation of the fitted functions and the gains. A fitted $1/\sqrt{E_{CE}}$ trend (solid line) is also shown. The uncertainty in this trend is represented by the shaded band.
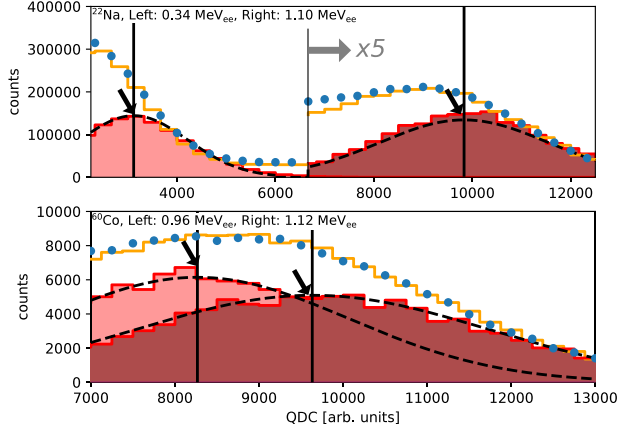
Fig. 7. Scintillation-light yield for multiple gamma-ray emitters. Data (filled points), gain-matching simulations (open histograms) and very restrictively cut Compton-edge histograms (shaded) are shown. Vertical solid lines illustrate the means of Gaussian distributions (dashed black curves, drawn to guide the eye) fitted to the simulated Compton-edge locations. The average values are indicated with angled arrows. The statistical uncertainties associated with the data points are smaller than the data points themselves. Note the ×5 in the middle of the upper panel.
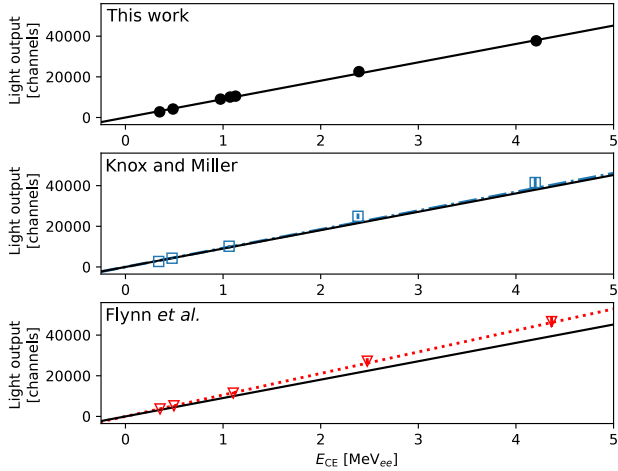
Fig. 8. Light-output calibrations. Top panel: This work, average values (filled circles, solid line) of the restrictively cut GEANT4 simulations. The solid average-value line shown in this panel appears in all panels to facilitate comparison between approaches. Middle panel: Knox and Miller approach (open squares, dot-dashed line). Bottom panel: Flynn et al. approach (open triangles, dotted line). Due to insufficient detector energy resolution, ^{60}Co results are not shown for the Knox and Miller or Flynn et al. analyses. The uncertainties are smaller than the data points themselves.

5. Summary and discussion

A scintillation light-yield calibration of an NE 213 A organic liquid scintillator detector (Fig. 1) has been performed using single-energy and double-energy gamma-ray sources. An event-by-event waveform-digitization (Fig. 2) of the scintillation signals resulted in measured Compton-edge distributions. Interpretation of the Compton-edge distributions used a GEANT4-based simulation which models the interactions of ionizing radiation and the transport of scintillation photons produced

Table 3
Linear fitted light-output calibrations.

Method	Zero unenforced			Zero enforced	
	Slope [$\frac{\text{channels}}{\text{MeV}_{ee}}$]	Offset [channels]	χ_v^2	Slope [$\frac{\text{channels}}{\text{MeV}_{ee}}$]	χ_v^2
GEANT4 (average value)	9612 ± 326	-434 ± 203	0.4	9049 ± 190	1.3
Knox and Miller	10443 ± 399	-803 ± 215	0.4	9222 ± 229	5.1
Flynn et al.	10767 ± 426	-147 ± 260	0.1	10576 ± 258	0.3

Table 4
Scintillation photons reaching the photocathode.

Method	Photons per MeV_{ee} reaching the photocathode
GEANT4 (average value)	$483 \pm 2.1\%$
Knox and Miller	$493 \pm 2.5\%$
Flynn et al.	$565 \pm 2.4\%$

along particle tracks. Simulations employed a 1700 photon per MeV_{ee} light-yield gradient, tuned to the data using relative PMT gain as a scaling parameter, and matched to the Compton edges by applying an additional smearing (Fig. 3). The relative gain function determined in this manner was linear over the $\sim$5 MeV_{ee} range considered at a photoelectron multiplication of $(3.27 \pm 0.07) \cdot 10^6$, corresponding to a (1388 ± 31) scintillation photon per MeV_{ee} light-yield gradient (Fig. 4). Charge distributions were determined as a function of electron energy by enforcing very strict cuts in the simulation around the upper edge of the recoiling electron energy-loss spectrum as well as considering the well-established prescriptions of Knox and Miller and Flynn et al. (Fig. 5) These restricted simulated distributions facilitated an evaluation of the intrinsic detector resolution, which was determined to be $\sim$18% at $\sim$1 MeV_{ee} and to fall off $\sim 1/\sqrt{E_{CE}}$ (Fig. 6). An advantage of the simulation approach over the prescriptions is that it allows for the unfolding of spectra from radioactive sources emitting more than one gamma-ray, even if the energy separation of the gamma-rays is small. To demonstrate this advantage, the entire simulation and analysis procedure was successfully repeated for two such sources, ^{22}Na (759 keV gamma-ray separation) and ^{60}Co (160 keV gamma-ray separation) (Fig. 7). Linear light-output calibrations were then determined (Fig. 8). The GEANT4-based method developed here was chosen as a benchmark. The prescriptions, while also linear, were $\sim$2% (Knox and Miller) and $\sim$17% larger (Flynn et al.) than the benchmark. The functions indicate that $\sim$35% of the scintillation light associated with a given gamma-ray reaches the photocathode. It is remarkable how well two 50 year old prescriptions for calibrating scintillation-light yield have stood the test of time.

Declaration of competing interest

The authors declare that they have no known competing financial interests or personal relationships that could have appeared to influence the work reported in this paper.

Acknowledgments

References

[1] NE213 is no longer produced. Eljen Technologies EJ-301, 2021, http://www.eljentechnology.com/index.php/products/liquid-scintillators/71-ej-301. (Accessed 24 September 2021), or Saint Gobain BC-501 https://www.crystals.saint-gobain.com/products/bc-501a-bc-519. (Accessed 24 September 2021) are very similar.

[2] R. Batchelor, et al., Nucl. Instrum. Methods 13 (1961) 70, http://dx.doi.org/10.1016/10.1016/0029-554X(61)90171-9.

[3] H.H. Knox, et al., Nucl. Instrum. Methods 101 (1972) 519, http://dx.doi.org/10.1016/0029-554X(72)90040-7.

[4] G.F. Knoll, Radiation Detection and Measurement, second ed., Wiley, New York, U.S.A., ISBN: 9780471815044, 1989, p. 222.

[5] J.R.M. Annand, et al., Nucl. Instrum. Methods Phys. Res. A 400 (1997) 344, http://dx.doi.org/10.1016/S0168-9002(97)01021-8.

[6] http://www.ggg-tech.co.jp/maker/eljen/ej-520.html. (Accessed 24 September 2021).

[7] See http://www.us.schott.com/borofloat/english/index.html. (Accessed 24 September 2021). Supplied by Glasteknik i Emmaboda AB, Utvägen 6 SE-361 31 Emmaboda, Sweden.

[8] Araldite is a registered trademark of huntsman, 2021, See http://www.araldite2000plus.com. (Accessed 24 September 2021).

[9] Viton is a registered trademark of DuPont Performance Elastomers LLC.

[10] Poly-methyl-methacrylate, also known as PMM, acrylic, plexiglass, and lucite. Supplied by Nordic Plastics Group AB, Bronsyxegatan 6, SE-213 75 Malmoe, Sweden.

[11] See https://eljentechnology.com/products/accessories/ej-510. (Accessed 24 September 2021).

[12] See https://et-enterprises.com/images/data_sheets/9821B.pdf. (Accessed 24 September 2021).

[13] J. Scherzinger, et al., Appl. Radiat. Isop. 98 (2015) 74, http://dx.doi.org/10.1016/j.apradiso.2015.01.003.

[14] R. Jebali, et al., Nucl. Instrum. Methods Phys. Res. A 794 (2015) 102, http://dx.doi.org/10.1016/j.nima.2015.04.058.

[15] J. Scherzinger, et al., Nucl. Instrum. Methods Phys. Res. A 840 (2016) 121, http://dx.doi.org/10.1016/j.nima.2016.10.011.

[16] J. Scherzinger, et al., Appl. Radiat. Isop. 127 (2017) 98, http://dx.doi.org/10.1016/j.apradiso.2017.05.014.

[17] J. Scherzinger, et al., Appl. Radiat. Isop. 128 (2017) 270, http://dx.doi.org/10.1016/j.apradiso.2017.05.022.

[18] See https://www.caen.it/products/vx1751/. (Accessed 24 September 2021).

[19] See https://www.caen.it/products/n858/. (Accessed 24 September 2021).

[20] H. Perrey, et al., 2021, Nuclear Physics Pulse Processing Library, available at https://gitlab.com/ANPLU/nppp. (Accessed 24 September 2021).

[21] G. van Rossum, F.L. Drake (Eds.), Python Reference Manual, PythonLabs, 2001, Python 3.8.5 available at https://www.python.org/. (Accessed 24 September 2021).

[22] The Pandas Development Team, pandas 1.2.3 available at https://pandas.pydata.org/. (Accessed 24 September 2021), http://dx.doi.org/10.5281/zenodo.4572994.

[23] https://www.scipy.org/. (Accessed 24 September 2021), http://dx.doi.org/10.5281/zenodo.4547611.

[24] W. McKinney, Proceedings of the 9th Python in Science Conference, vol. 445, 2010, p. 56, http://dx.doi.org/10.25080/Majora-92bf1922-00a.

[25] numpy 1.20.3 available at https://pypi.org/project/numpy/. (Accessed 24 September 2021).

[26] S. Agostinelli, et al., Nucl. Instrum. Methods Phys. Res. A 506 (2003) 250, http://dx.doi.org/10.1016/S0168-9002(03)01368-8.

[27] J. Allison, et al., IEEE Trans. Nucl. Sci. 53 (2006) 270, http://dx.doi.org/10.1109/TNS.2006.869826.

[28] L. Boyd, et al., Nucl. Instrum. Methods Phys. Res. A 998 (2021) 165174, http://dx.doi.org/10.1016/j.nima.2021.165174.

[29] Geant4 physics reference manual, 2020, Release 10.6 available at http://geant4-userdoc.web.cern.ch/geant4-userdoc/UsersGuides/PhysicsReferenceManual/fo/PhysicsReferenceManual.pdf.

[30] Geant4 book for application developers, 2020, Release 10.6 available at http://geant4-userdoc.web.cern.ch/geant4-userdoc/UsersGuides/ForToolkitDeveloper/fo/BookForToolkitDevelopers.pdf.

[31] P. Gumplinger, Optical photon processes in Geant4, Users' Workshop at CERN, Nov. 2002.

[32] K.F. Flynn, et al., Nucl. Instrum. Methods 27 (1964) 13, http://dx.doi.org/10.1016/0029-554X(64)90129-6.

[33] L.E. Beghian, et al., Nucl. Instrum. Methods 35 (1965) 34, http://dx.doi.org/10.1016/0029-554X(65)90004-2.

[34] G. Dietze, et al., Nucl. Instrum. Methods 139 (1982) 549, http://dx.doi.org/10.1016/0029-554X(82)90249-X.

[35] F. Arnedodo, et al., Nucl. Instrum. Methods Phys. Res. A 418 (1998) 285, http://dx.doi.org/10.1016/S0168-9002(98)00679-2.

[36] C. Matei, et al., Nucl. Instrum. Methods Phys. Res. A 676 (2012) 135, http://dx.doi.org/10.1016/j.nima.2011.11.076.

Paper III

Technique for the measurement of intrinsic pulse-shape discrimination for organic scintillators using tagged neutrons

N. Mauritzson [a], K.G. Fissum [a,b,*], J.R.M. Annand [c], H. Perrey [a], R.J.W. Frost [a], R. Al Jebali [b,c], A. Backis [b,c], R. Hall-Wilton [b,c,d,1], K. Kanaki [b], V. Maulerova-Subert [a,b,2], C. Maurer [a], F. Messi [a,3], E. Rofors [a]

[a] Division of Nuclear Physics, Lund University, SE-221 00, Lund, Sweden
[b] Detector Group, European Spallation Source ERIC, SE-221 00, Lund, Sweden
[c] School of Physics and Astronomy, University of Glasgow, Glasgow G12 8QQ, Scotland, UK
[d] Dipartimento di Fisica "G. Occhialini", Università degli Studi di Milano-Bicocca, Piazza della Scienza 3, 20126 Milano, Italy

ARTICLE INFO

ABSTRACT

Fast-neutron/gamma-ray pulse-shape discrimination has been performed for the organic liquid scintillators NE 213A and EJ 305 using a time-of-flight based neutron-tagging technique and waveform digitization on an event-by-event basis. Gamma-ray sources and a Geant4-based simulation were used to calibrate the scintillation-light yield. The difference in pulse shape for the neutron and gamma-ray events was analyzed by integrating selected portions of the digitized waveform to produce a figure-of-merit for neutron/gamma-ray separation. This figure-of-merit has been mapped as a function of detector threshold and also of neutron energy determined from time-of-flight. It shows clearly that the well-established pulse-shape discrimination capabilities of NE 213A are superior to those of EJ 305. The extra information provided by the neutron-tagging technique has resulted in a far more detailed assessment of the pulse-shape-discrimination capabilities of these organic scintillators.

1. Introduction

Organic liquid scintillators are commonly used to detect fast neutrons in fields of gamma-rays. The main scintillation decay time constant for organic materials is generally of the order of a few ns. Several organics also have much longer decay components. The fast components are preferentially excited by relativistic particles, which are close to minimum ionizing, while slower components are excited by non-relativistic particles which ionize more heavily along their tracks. For example, NE 213A has 3 components with mean decay times of 3.2, 32.3, and 270 ns. Secondary electrons produced by gamma-rays are close to minimum ionizing and thus give a fast signal. Protons produced after neutron scattering from scintillator hydrogen are heavily ionizing and produce more of the slow scintillation components. Thus, analysis of the fall time of the scintillation signal may be used to differentiate incident gamma-rays from neutrons. This technique is known as pulse-shape discrimination (PSD).

Due to excellent PSD capabilities, the organic liquid scintillator NE 213 [1] and the more recent derivative NE 213A [2] have long

been used widely [3], and provide a performance benchmark for newly developed fast-neutron detector materials [4–7]. A more recent organic liquid EJ 305 [8] developed for a very high scintillation-light yield is anticipated to have poorer PSD capabilities. In this paper, tagged neutrons from ~1.5–6 MeV are employed to investigate the PSD capabilities of these neutron-sensitive scintillators. Evaluation of the PSD performance is performed both with and without the neutron-tagging technique, and in a situation where PSD is not optimum.

2. Apparatus

2.1. PuBe-Based neutron and gamma-ray mixed-field source

Fast neutrons were provided by a ^{238}Pu/^{9}Be (PuBe) source. ^{238}Pu decays to ^{234}U via α-particle emission (14 branches, weighted mean energy 5.4891 MeV [9]), and almost simultaneously, a cascade of low-energy gamma-rays results from the de-excitation of ^{234}U. Fast neutrons produced by the reaction $\alpha + {}^9\text{Be} \rightarrow {}^{12}\text{C} + \text{n}$ have a maximum kinetic energy of ~11 MeV. When the final-state ^{12}C is left in the
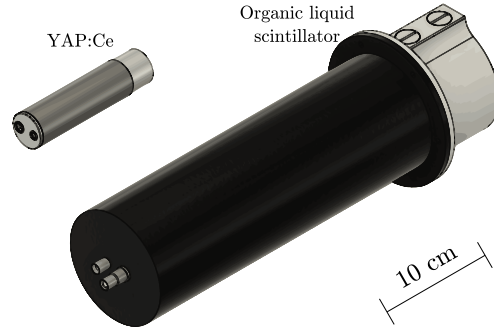
Fig. 1. CAD representations of the detectors (to scale). The PMTs lie to the left while the scintillator enclosures lie to the right.

first-excited state (with ∼50% probability), it promptly de-excites by the isotropic emission of a 4.44 MeV gamma-ray. The total radiation field associated with the PuBe source thus consists of a low-energy cascade gamma-rays, fast neutrons with energies up to ∼11 MeV, and a sub-field of particular interest: 4.44 MeV gamma-rays in coincidence with fast neutrons of energy up to ∼6 MeV. This sub-field was used to produce tagged-neutron beams, where detection of the 4.44 MeV gamma-rays gave a reference time for neutron time-of-flight (TOF) measurements. The PuBe source was a blend of plutonium oxide and beryllium metal sealed in an X.3 capsule which emitted approximately 2.9×10^6 neutrons per second [10] nearly isotropically. See Ref. [11] for further details.

2.2. Detectors

Fig. 1 shows CAD representations of two types of scintillation counters employed in this investigation. Cells of organic liquid detected fast neutrons and gamma-rays. They provided the start signal for TOF measurements as well as the pulse-shape information used to discriminate neutrons from gamma-rays (PSD). YAP:Ce crystals detected gamma-rays and provided the stop signal for TOF measurements.

2.2.1. Gamma-ray trigger detectors

Yttrium Aluminum Perovskit:Cerium (Ce^+ doped $YAlO_3$, YAP:Ce) inorganic crystals [12] have good gamma-ray detection efficiency and low efficiency for neutrons in the energy range investigated here. Four YAP:Ce detectors were used to detect both actinide-cascade and 4.44 MeV gamma-rays in the presence of the intense fast-neutron field of the PuBe source. Provided by Scionix [13], they consisted of a cylindrical 1 in. × 1 in. (diameter × height) crystal mounted on a 1 in. Hamamatsu Type R1924 PMT [14]. A ^{22}Na gamma-ray source (E_γ = 1.28 MeV) was used to set the YAP:Ce gains with HV values of ∼ −750 V. The YAP:Ce detectors, with minimal sensitivity to the fast neutrons from the PuBe source, provided the gamma-ray tags.

2.2.2. Fast-neutron/gamma-ray detector

Cylindrical aluminum cups, 94 mm in diameter by 62 mm deep with a thickness of 3 mm, contained the liquid scintillators. The inside of each cup was painted with EJ 520 [15], a TiO_2-based reflector. A 5 mm thick borosilicate glass window [16] was glued to each cup using Araldite 2000+ [17]. For each detector, the cup/window assembly constituted a ∼430 cm^3 liquid-scintillator cell. The liquid scintillators were first flushed with nitrogen and then pushed into the cells with a nitrogen gas-transfer system. The entrance/exhaust ports were sealed with screws and Viton O-rings [18]. Filled cells were fitted without

Table 1
Selected scintillator properties.

Scintillator	NE 213A	EJ 305
Base	Pseudocumene	Pseudocumene
Flash point (°C)	∼54	∼45
Density (g/cm³)	∼0.9	∼0.89
Pristine light output (% anthracene)	∼75%	∼80%
Decay times (short, ns)	∼3	∼2.7
Peak emission wavelength (nm)	∼420	∼425

optical coupling grease (dry fitted) to 57 mm long by 72.5 mm diameter cylindrical lightguide made from PMMA UVT [19]. The lightguides were coated externally with EJ 510 [20], a TiO_2-based reflector. These cell/lightguide assemblies were dry fitted to 3 in. diameter Electron Tubes type 9821KB PMTs [21]. The assemblies were placed within mu-metal magnetic shields and a spring was used to hold the cell, PMMA, and PMT faces tightly together. The operating voltage of the detector was set at −2 kV, as employed in previous investigations of similar detectors [7,11,22,23]. HV was not tuned to match the gains of the detectors, but variable attenuators (CAEN type N858 [24]) were inserted to equalize the signal amplitudes passed to a waveform digitizer. After matching, typical 1 MeV_{ee} signals had amplitudes of ∼700 mV, with risetimes of ∼5 ns and falltimes of ∼60 ns. The cells were filled with two different liquid scintillators developed for fast-neutron detection. These were NE 213A [2] (a pseudocumene-based variant of NE 213 [1]) possessing excellent fast neutron PSD properties and EJ 305 [8], a pseudocumene-based organic scintillator with one of the highest scintillation-light yield outputs of any liquid scintillator. EJ 305 has a long optical attenuation length but poorer PSD properties compared to NE 213A. Selected scintillator properties are presented in Table 1.

2.3. Configuration

Fig. 2 shows a sketch of the experimental setup. The PuBe source was placed so that its cylindrical-symmetry axis corresponded to the vertical direction in the lab. Four YAP:Ce detectors were also placed with the cylindrical-symmetry axes in the vertical direction, each approximately 10 cm from the PuBe source, with slightly varying out-of-plane positions. These detectors measured low-energy cascade gamma-rays from ^{234}U as well as the energetic 4.44 MeV gamma-rays coming from α + ^{9}Be → ^{12}C + n + γ. The PuBe source and four YAP:Ce detectors were encased in a water-filled shielding cube known as the "Aquarium" [25] with a water-filled wall thickness of ∼50 cm. A
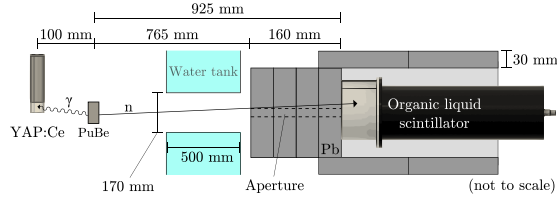
Fig. 2. Experimental setup (not to scale). Conceptually, the PuBe source positioned at the center of a water tank emitted correlated 4.44 MeV gamma-ray/fast-neutron pairs. The neutrons were detected in a Pb-shielded liquid-scintillator detector located outside the water tank to trigger the TOF measurement. The corresponding gamma-rays were detected in a YAP:Ce detector located inside the water tank to stop the TOF measurement. A small aperture was left in the shielding house to facilitate the gamma-flash measurements necessary to calibrate TOF.

~17 cm diameter penetration in each of the four walls of the Aquarium allowed gamma-rays and fast neutrons to escape the shielding confinement, defining beams. At one beam-port exit, a Pb castle was constructed to encase the liquid-scintillator detectors and facilitate the reproducibility of the positioning of the detector. Room background measured inside the castle using a 1.5 in. CeBr$_3$ detector with a -50 mV threshold was <1 Hz. The NE 213A detector with a −25 mV threshold showed a background rate of ~50 Hz. As shown in Fig. 2, the liquid-scintillator detectors were placed in the castle with the upstream face of the cell at a distance of 92.5 cm from the center of the PuBe source and at source height. The cylindrical symmetry axis of this detector pointed directly at the center of the source. A ~10 × 10 mm^2 aperture in the 16 cm thick face of the Pb castle allowed this detector to measure source-related low-energy cascade gamma-rays and energetic 4.44 MeV gamma-rays. Two types of coincidence events were of special interest:

1. a fast neutron detected in the liquid-scintillator detector in co-incidence with a 4.44 MeV gamma-ray detected in a YAP:Ce detector (a "tagged-neutron" event).
2. prompt, time-correlated gamma-ray pairs emitted from the PuBe source detected in the liquid-scintillator detector and a YAP:Ce detector (a "gamma-flash" event).

See Ref. [22] for further details.

2.4. Electronics and data acquisition

A CAEN VX1751 Waveform Digitizer [26] (10 bit, 500 MHz analog bandwidth) was employed for data acquisition. The dynamic range was −1 V and 10^3 samples were taken during the 1 μs acquisition window. A −25 mV internal falling-edge trigger threshold was used. The software [27] employed to analyze the waveform of each pulse included Python-based [28] code libraries pandas [29], SciPy [30], and numpy [31]. The liquid-scintillator event timing was determined using an interpolating zero-crossover method [32] which reduced the time walk associated with the internal hardware trigger of the digitizer. For each scintillation pulse, the signal baseline was subtracted and the resulting waveform (see Fig. 3) was integrated, effectively giving the signal charge. This charge integration (6.35 ± 5.5% fC/channel) was started 25 ns before the event-timing marker, and the integration gate length was set to 60 ns for a short-gate (SG) integration and 500 ns for a long-gate (LG) integration. Pulse shape (PS) was parametrized using the "tail-to-total" method [6,33,34] (Eq. (1)) where the difference in the signals registered by the LG and SG integrations was normalized to the signal registered by the LG integration.

$$PS = \frac{LG - SG}{LG} \tag{1}$$

Table 2
Gamma-ray sources. The gamma-ray energies and recoiling electron energies at the Compton edges E_{CE} are shown.

Source	E_γ [MeV]	E_{CE} [MeV$_{ee}$]
^{137}Cs	0.66	0.48
^{232}Th	2.62	2.38
^{241}Am/^{9}Be (AmBe)	4.44	4.20

2.5. Energy calibration

The scintillation-light yield produced by incident gamma-rays in organic liquids is almost linear above ~100 keV [32,35]. Below pair-production threshold, Compton scattering dominates because of the low average Z value of the scintillator. Compton edges were measured with the gamma-ray sources listed in Table 2 and the results are displayed in Fig. 4.

Each detector was aligned so that the cylindrical symmetry axis pointed at the calibration source. ^{137}Cs and ^{232}Th were placed at a distance of 50 cm from the face of the detector, while the stronger AmBe was placed at a distance of 200 cm. A typical run lasted one hour. Count rates were <1 kHz and thus pileup and dead time were negligible. Room background was subtracted from each spectrum using a real-time normalization. Gain drift in the YAP:Ce was determined to be negligible. Gain drift in the liquid-scintillator detectors was corrected for by aligning the 4.44 MeV Compton edge in software on a run-by-run (hourly) basis. This correction did not exceed ~1%. The response of the detectors to the gamma-rays was simulated using GEANT4 [36] version 4.10.04 [37] patch 03 (8 February 2019) with a physics list based on the electromagnetic physics classes G4EmStandardPhysics, G4EmExtraPhysics and including the hadronic interaction class FTFP_BERT_HP. Gamma-ray response was simulated by tracking secondary electrons and the resulting scintillation photons, which were followed to the photocathode. Here, the wavelength-dependent quantum efficiency [21] gave the probability of a photon producing a photoelectron. The scale factor necessary to match the number of simulated photoelectrons at the photocathode to the measured signal charge was the only free parameter. The positions of the Compton edges were determined from the simulations by placing a tight cut around the electron energy very close to the edge, as described in Ref. [38]. The result of the energy calibration is presented in Fig. 4.

Fig. 5 shows the typical correlation between the energy deposited in the YAP:Ce detector and the energy deposited in the NE 213A liquid-scintillator detector. The YAP:Ce energy calibration employed the Compton edge of the 4.44 MeV gamma-ray, which does not produce a full-energy peak in the 1 in. crystal, and the full-energy peak from the 1.28 MeV gamma-ray of ^{22}Na. The linear fit is constrained to pass through the origin. Events above the YAP:Ce detector threshold of 3 MeV$_{ee}$ result from the 4.44 MeV gamma-ray and thus correspond to
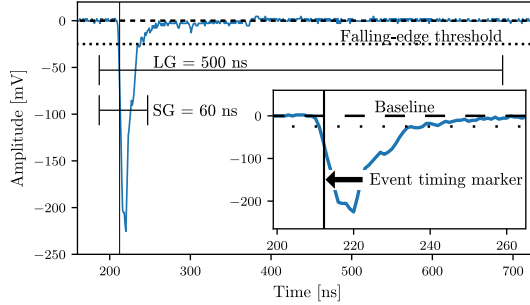
Fig. 3. Signal waveform. Typical signals had a ~5 ns risetime, a ~ −230 mV amplitude, and a ~50 ns falltime. The falling-edge threshold was set to −25 mV. Also illustrated are the event-timing marker and both the 500 ns long-gate (LG) and 60 ns short-gate (SG) integration windows, each opening 25 ns before this marker.
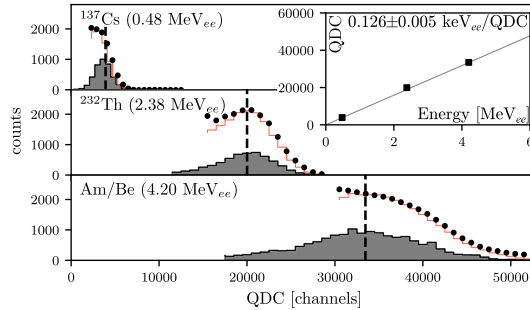

Fig. 4. Energy calibration. Measured and simulated Compton distributions for three gamma-ray energies incident on the NE 213A scintillator. Measurement: filled circles; simulation: orange histograms; simulation with tight cut on maximum electron energy: gray shaded histograms. The dashed lines show the mean values of the gray distributions. The inset plots these mean values against the gamma-ray energies along with a linear fit. For interpretation of the references to color in this figure caption, the reader is referred to the web version of this article.

candidate tagged-neutrons events. This threshold was held fixed during the analysis. Events below the YAP:Ce detector threshold correspond overwhelmingly to lower energy gamma-rays, but may include the occasional neutron (YAP:Ce is largely insensitive to neutrons). The subset of these events which produce a coincident signal in the liquid scintillator are gamma-flash events, corresponding to time-correlated gamma-rays being detected in both detectors.

3. Results

Fig. 6 presents a representative TOF distribution obtained for an average neutron drift distance of 96 cm. The vertical dashed line located at 0 ns and labeled T_0 locates the time of particle production in the PuBe source. It is inferred from the gamma flash timing, which is given by the sharp peak to the right of T_0 at ~2.9 ns. The gamma flash corresponds overwhelmingly to one of the correlated gamma-rays being detected in a YAP:Ce detector and the other in the liquid-scintillator detector. The ~1 ns width of the gamma flash is due to a combination of electronic jitter and finite detector volumes. The broader peak to the right of the gamma flash is due to tagged neutrons, and corresponds to a 4.44 MeV gamma-ray being detected in a YAP:Ce detector while the corresponding fast neutron is detected in the liquid-scintillator detector.

The gamma-flash and tagged fast-neutron distributions are clearly separated. A flat distribution of random-coincidence events spans the entire TOF distribution. These random events arise from uncorrelated signals in the YAP:Ce and liquid scintillators which fall randomly within the acquisition window. Since the counting rates were relatively low, the random distribution is flat and straightforward to subtract from under the correlated distributions [39].

Fig. 7 shows PS versus energy deposited in the liquid-scintillator detectors for singles and tagged data. The tagged data are kinematically restricted to neutron kinetic energies below ~6 MeV due to energy taken by the 4.44 MeV gamma-ray. For both scintillators, neutrons result in larger PS values as they produce more of the slower scintillation component. The separation between the neutron distributions and the gamma-ray distributions is considerably larger for NE 213A where the optimum cut for neutron/gamma-ray separation sits at PS = 0.3. For EJ 305, the corresponding cut would be at PS = 0.2. NE 213A clearly provides superior PSD.

Fig. 8 shows PS data from the detectors produced with a 2 MeV$_{ee}$ detector threshold. Overlap at the 10% level between the gamma-ray and neutron distributions is displayed for the singles data for NE 213A shown in the top panel. In contrast, much cleaner separation is shown in the tagged, random-subtracted distributions for NE 213A

4
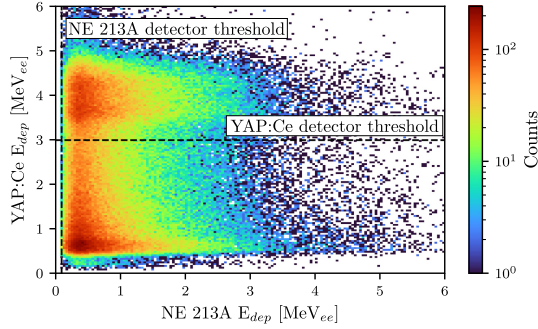
Fig. 5. Energy correlation. Energy deposited in the YAP:Ce gamma-ray detector versus energy deposited in NE 213A liquid-scintillator detector. The dashed lines indicate the threshold used for each detector, 100 keV$_{ee}$ for the NE 213A and 3 MeV$_{ee}$ for the YAP:Ce. The structure lying above the YAP:Ce threshold corresponds to candidate tagged-neutron events.
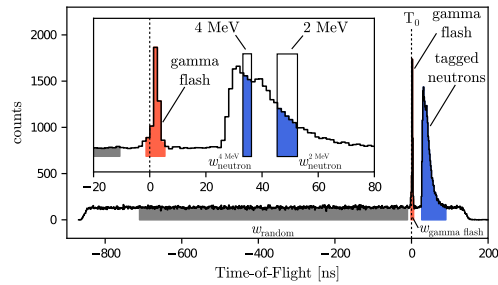
Fig. 6. TOF spectrum. The full range of the acquisition window (including the flat random region) and an expanded view of the region of main interest are shown. The boxes illustrate the TOF ranges of 500 keV wide bins of neutron kinetic energy centered at 2 and 4 MeV.
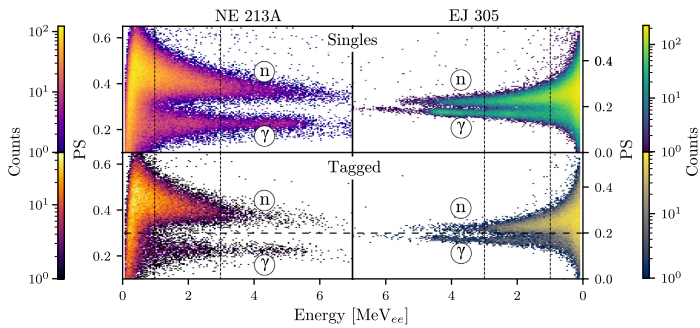
Fig. 7. Pulse shape versus energy. A software threshold of 100 keV$_{ee}$ has been applied to the data from both scintillators. The dashed vertical lines at 1 and 3 MeV$_{ee}$ are representative of the systematic series of threshold cuts applied in the subsequent data analysis. The long-dashed horizontal line indicates the boundary between neutron (above) and gamma-ray (below) events. Note the y-axes and color scales are different for NE 213A and EJ 305.
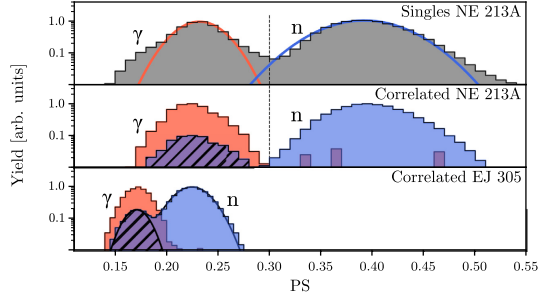
Fig. 8. Non-prompt gamma-rays (NPGs). PS spectra for an energy threshold of 2 MeV$_{ee}$. Top: NE 213A singles data where there is no coincidence with the YAP:Ce detectors. The red and blue curves are Gaussian fits to the gamma-ray and neutron distributions. Middle: correlated NE 213A data where there is a coincidence. Gamma-ray and neutron distributions are completely separated using TOF. Neutron and NPG distributions are separated by PS. Bottom: correlated EJ 305 data where there is a coincidence. The diagonally hatched areas show the NPG contributions. For interpretation of the references to color in this figure caption, the reader is referred to the web version of this article.

presented in the middle panel. In fact, the particle identification in these correlated results, produced using the tagging technique, is sufficient to separate gamma-rays, neutrons, and non-prompt gamma-rays (NPGs). NPGs are source-related, tagged events which have the non-relativistic TOF signature of a fast neutron but the PS signature of a gamma-ray. They are due to tagged fast neutrons scattering inelastically, predominantly from the lead shielding, or much less frequently from the materials from which the neutron detector was constructed. The resulting de-excitation gamma-rays are then detected in the liquid-scintillator detector. As NPGs are tagged and not random, they appear very clearly in the correlated PS spectra, and a PS > 0.3 cut is sufficient to remove them. As shown in the bottom panel, the separation between gamma-rays and neutrons is substantially smaller for EJ 305, and significant overlap between the distributions exists. Thus a PS cut does not remove NPGs cleanly and a Gaussian fit to the left side of the NPG/neutron distribution has been employed to estimate their contribution.

A Canberra [40] model GC2018 HPGe gamma-ray detector with a 7935SL-2 cryostat and 2002CSL preamp was placed inside the Pb shielding house (no aperture) to measure the NPG spectrum. The detected gamma-rays are overwhelmingly due to the de-excitation of low-lying excited states of the isotopes of ^{nat}Pb, dominated by the 2615 keV line from the first excited state of ^{208}Pb. The indicated PS > 0.3 cut was applied to the correlated neutron data obtained with NE 213A to remove the NPG-related contamination.

Fig. 9 shows the PS distributions for the correlated data from NE 213A and EJ 305, for a software threshold that has been increased from 0.25 to 3.75 MeV$_{ee}$ in steps of 0.25 MeV$_{ee}$. The gamma-ray distributions have been scaled to match the heights of the neutron distributions for purposes of visualization. These scaling factors ranged from ~11 (0.25 MeV$_{ee}$) to ~0.5 (3.75 MeV$_{ee}$) for NE 213A and from ~4 (0.25 MeV$_{ee}$) to ~0.7 (2.75 MeV$_{ee}$) for EJ 305. NPGs have been identified using TOF and PS. For NE 213A, they have been removed with a PS > 0.3 cut. For EJ 305 the NPG contribution was estimated from a Gaussian fit (Fig. 8) and subtracted. The tagging approach facilitates the unambiguous identification of gamma-rays and neutrons. The gamma-ray peak locations do not change as the threshold is varied and sit at PS ~0.22 for NE 213A and ~0.18 for EJ 305. The peak locations of the neutron PS distributions decrease linearly with increasing threshold, so that the separation between the gamma-ray and neutron peak locations is largest for the lowest threshold and decreases as the applied threshold increases. However the widths of the PS distributions also decrease with increasing threshold, so that neutron/gamma-ray separation actually improves significantly.

The Figure-of-Merit (FOM) used to characterize the quality of PSD in organic scintillators is commonly defined as

$$FOM = \frac{|\mu_n - \mu_\gamma|}{\delta_n + \delta_\gamma}, \qquad (2)$$

where $\mu_{n,\gamma}$ and $\delta_{n,\gamma}$ are the mean positions and Full-Widths-at-Half-Maximum (FWHM) of the gamma-ray and neutron PS distributions respectively. The larger the FOM, the better the PSD. Fig. 10 shows the intrinsic FOM as a function of software threshold. The excellent separation of the gamma-ray and neutron PS distributions facilitated a numerical analysis of peak locations and widths over $\pm 3\sigma$ of the respective distributions. The uncertainties in the resulting FOM values were established from a error analysis which considered both linear and quadratic propagation of the uncertainties from the numerical approach, with the relative uncertainty in the standard deviation was estimated to be ~5%. For both NE 213A and EJ 305, the uncertainties were ~10%. For both NE 213A and EJ 305, the intrinsic FOM values increase with increasing detector threshold. NE 213A demonstrates superior FOM for all thresholds.

Fig. 11 shows the evolution of PS spectra for the correlated gamma-ray and neutron data for both NE 213A and EJ 305 as the average neutron kinetic energy obtained from TOF is raised from 1.50 to 6.00 MeV in 0.25 MeV steps. A 0.5 MeV$_{ee}$ software threshold was employed. The gamma-ray distributions have been scaled to match the heights of the neutron distributions for purposes of visualization. These scaling factors ranged from ~0.3 (1.50 MeV) to ~0.1 (6.00 MeV) for NE 213A and from ~0.02 (1.50 MeV) to ~0.2 (6.00 MeV) for EJ 305. NPGs have been identified using TOF and PS and removed or corrected for as described previously. The peak locations of the gamma-ray distributions do not change with neutron kinetic energy and sit at PS ~0.22 for NE 213A and ~0.18 for EJ 305. Again, the peak locations of the neutron distributions decrease linearly with increasing neutron kinetic energy. The separation between the gamma-ray and neutron peaks is largest for the lowest energy and decreases as the kinetic energy increases, but this is offset by the increase in distribution widths as energy decreases.

Fig. 12 shows the intrinsic FOM values extracted from the data displayed in Fig. 11 as a function of neutron kinetic energy using the same methods as for the data of Figs. 9 and 10. For both NE 213A and EJ 305, the uncertainties were ~10%. The neutron-energy dependencies of the FOM distributions are quite similar, but clearly the NE 213A values are considerably larger than EJ 305.
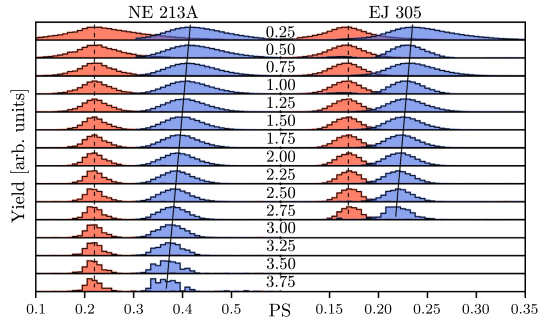
Fig. 9. Intrinsic threshold-dependent pulse shape. Correlated gamma-ray distributions are shown in red and neutron distributions are shown in blue. TOF cuts together with PS cuts (NE 213A) or fitting (EJ 305) have been employed to remove NPGs. The threshold in MeV_{ee} for each pad is shown in the center of the plot. Lines show linear fits to the means of the distributions, dashed for gamma-rays and solid for neutrons. For interpretation of the references to color in this figure caption, the reader is referred to the web version of this article.
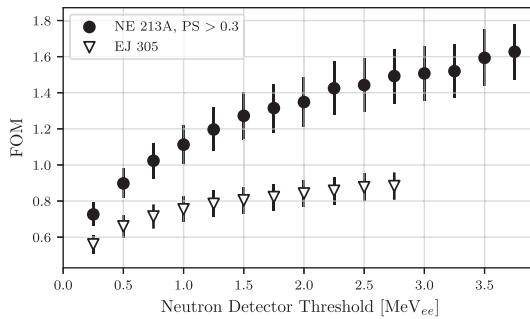

Fig. 10. Threshold-dependent figures-of-merit. Numerically evaluated intrinsic FOM resulting from the correlated data presented in Fig. 9 for NE 213A (black dots) and EJ 305 (open triangles). Derivation of the uncertainties is detailed in the text.

4. Summary and discussion

A systematic quantification of neutron/gamma-ray PSD has been performed for the organic liquid scintillators NE 213A and EJ 305 using energy-tagged neutrons from ∼1.5–6 MeV provided by a PuBe source. Tagging relies on the α + ^{9}Be → ^{12}C + n + γ reaction, where the neutron and gamma-ray are detected in coincidence and the gamma-rays provide a time reference for neutron TOF measurement. YAP:Ce crystals were used to detect these 4.44 MeV gamma-rays, and liquid-scintillator cells were employed to detect the corresponding neutrons (Fig. 1). The source and YAP:Ce detectors were located inside a water-filled shielding cube, which had cylindrical penetrations to allow for the passage of fast neutrons. Pb was used to shield the liquid scintillators from the direct gamma-ray field from the source and also the 2.22 MeV gamma-rays resulting from neutron capture by H in the water (Fig. 2). Event-by-event waveform digitization of the detector signals (Fig. 3) was employed. Measured spectra were calibrated using the Compton edges from gamma-ray sources, whose pulse-height positions were established using a Geant4-based simulation (Fig. 4). The correlation between the gamma-ray energy in the YAP:Ce detector and the neutron energy deposited in the liquid-scintillator cells (Fig. 5) facilitated the selection of neutron-tagging

events. Time-of-flight was employed to determine neutron energy. The measurement time window of length 1 μs allowed accurate determination of random-coincidence background, which was then subtracted (Fig. 6). PS was evaluated using the tail-to-total method and resulted in excellent separation of gamma-ray and neutron distributions (Fig. 7) when neutron tagging with random subtraction and removal of NPGs (Fig. 8) was employed. Untagged PS distributions show significantly poorer neutron/gamma-ray separation.

The evolution of the correlated gamma-ray and neutron PS distributions was investigated as the software threshold was raised from 0.25 to 3.75 MeV_{ee} (Fig. 9). The resulting FOM values (Fig. 10) show clearly that NE 213A has superior PSD to EJ 305. NE 213A FOM values improve significantly as the pulse-height threshold is increased, while EJ 305 showed a weaker dependence of FOM on threshold. This level of detail for the PSD performance is only possible when the extra information provided by the tagging technique is obtained. The correlated gamma-ray and neutron PS distributions were also investigated for neutron kinetic energy (TOF) cuts (Fig. 11) ranging from 1.50 to 6.00 MeV. While both NE 213A and EJ 305 demonstrated FOM values that are more or less constant as a function of energy (Fig. 12), NE 213A is again clearly superior to EJ 305.
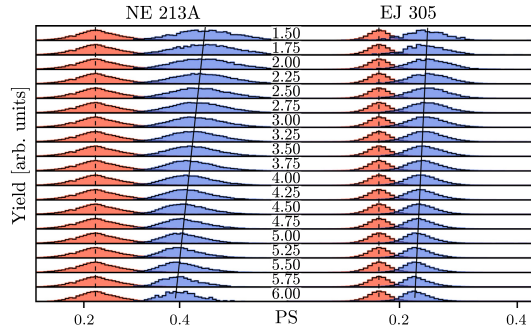
Fig. 11. Intrinsic neutron kinetic-energy dependent pulse shape. Correlated gamma-ray distributions are shown in red and neutron distributions are shown in blue. TOF cuts together with PS cuts (NE 213A) or fitting (EJ 305) have been employed to remove NPGs. The neutron kinetic energies in MeV (±0.125 MeV) for each plot are shown in the center of the figure. The lines show linear fits to the mean values of the distributions, dashed for gamma-rays and solid for neutrons. For interpretation of the references to color in this figure caption, the reader is referred to the web version of this article.
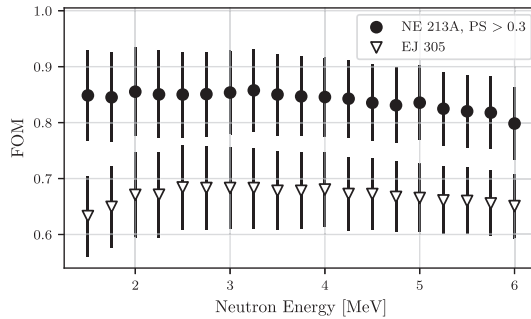

Fig. 12. Energy-dependent figures-of-merit. FOM extracted from the correlated data presented in Fig. 11 for NE 213A (black dots) and EJ 305 (open triangles). Derivation of the uncertainties is detailed in the text.

With the PuBe source, the tagged-energy range is relatively small and extension would require an accelerator-based neutron generator. While the neutron-tagging technique offers increased insight into threshold-dependent scintillator response, a clear advantage of the technique lies in the measurement of scintillator response as a function of incident neutron energy using polychromatic neutron sources. Such information is crucial, for example, to the validation of simulation efforts.

CRediT authorship contribution statement

N. Mauritzson: Conceptualization, Methodology, Software, Validation, Formal analysis, Investigation, Data curation, Writing – original draft, Writing – review & editing, Visualization, Project administration. **K.G. Fissum:** Conceptualization, Methodology, Validation, Formal analysis, Investigation, Resources, Writing – original draft, Writing – review & editing, Visualization, Supervision, Project administration, Funding acquisition. **J.R.M. Annand:** Conceptualization, Methodology, Software, Validation, Formal analysis, Writing – original draft, Writing – review & editing, Visualization, Supervision. **H. Perrey:** Software, Investigation, Data curation, Writing – review & editing, Visualization, Supervision. **R.J.W. Frost:** Supervision, Writing – review & editing. **R. Al Jebali:** Supervision. **A. Backis:** Software, Supervision. **R. Hall-Wilton:** Conceptualization, Resources, Supervision, Project administration, Funding acquisition. **K. Kanaki:** Conceptualization, Software, Resources, Supervision, Funding acquisition. **V. Maulerova-Subert:** Conceptualization, Software, Investigation, Supervision. **C. Maurer:** Investigation, Data curation. **F. Messi:** Investigation, Writing – review & editing, Supervision. **E. Rofors:** Supervision.

Declaration of competing interest

The authors declare that they have no known competing financial interests or personal relationships that could have appeared to influence the work reported in this paper.

Data availability

The data set doi:10.5281/zenodo.6611420 is available for download from https://zenodo.org/record/6611420

8

Acknowledgments

References

[1] NE 213 is no longer produced. Eljen Technologies EJ-301 (https://eljentechnology.com/products/liquid-scintillators/ej-301-ej-309 [Accessed 1 June 2022] or Saint Gobain BC-501 (https://www.crystals.saint-gobain.com/products/bc-501a-bc-519 [Accessed 1 Jun. 2022] are very similar.

[2] J.R.M. Annand, et al., Nucl. Instrum. Methods Phys. Res. A. 400 (1997) 344, http://dx.doi.org/10.1016/S0168-9002(97)01021-8.

[3] R. Batchelor, et al., Nucl. Instrum. Methods Phys. Res. A. 13 (1961) 70, http://dx.doi.org/10.1016/0029-554X(61)90171-9.

[4] E. Bayat, et al., Radiat. Phys. Chem. 81 (3) (2012) 217, http://dx.doi.org/10.1016/j.radphyschem.2011.10.016.

[5] J. Iwanowska, et al., Nucl. Instrum. Methods Phys. Res. A. 712 (2013) 34, http://dx.doi.org/10.1016/j.nima.2013.01.064.

[6] I.A. Pawełczak, et al., Nucl. Instrum. Methods Phys. Res. A. 711 (2013) 21, http://dx.doi.org/10.1016/j.nima.2013.01.028.

[7] R. Jebali, et al., Nucl. Instrum. Methods Phys. Res. A. 794 (2015) 102, http://dx.doi.org/10.1016/j.nima.2015.04.058.

[8] EJ 305 Highest Light output Liquid Scintillator, http://www.ggg-tech.co.jp/maker/eljen/ej-305.html [Accessed 1 Jun 2022].

[9] NuData 3.0, National Nuclear Data Center, Brookhaven National Laboratory, http://www.nndc.bnl.gov/nudat2/ [Accessed 1 Jun 2022].

[10] Exactly 4.26 × 10⁶ neutrons per second. Calibration certified at The Radiochemical Centre, Amersham, England HP7 9LL on 3 1973.

[11] J. Scherzinger, et al., Appl. Radiat. Isop. 127 (2017) 98, http://dx.doi.org/10.1016/j.apradiso.2017.05.014.

[12] M. Moszyński, et al., Nucl. Instrum. Methods Phys. Res. A. 101 (1972) 519, http://dx.doi.org/10.1016/S0168-9002(97)01115-7.

[13] Scionix Holland BV, http://www.scionix.nl [Accessed 1 June 2022].

[14] Hamamatsu Photonics, http://www.hamamatsu.com [Accessed 1 June 2022].

[15] EJ 520 reflective paint, http://www.ggg-tech.co.jp/maker/eljen/ej-520.html [Accessed 1 June 2022].

[16] Borofloat, https://www.schott.com/en-us/products/borofloat [Accessed 1 June 2022], supplied by Glasteknik i Emmaboda AB, Utvägen 6 SE-361 31 Emmaboda, Sweden.

[17] Araldite is a registered trademark of Huntsman, http://www.araldite2000plus.com [Accessed 1 June 2022].

[18] Viton is a registered trademark of DuPont Performance Elastomers LLC.

[19] Poly-methyl-methacrylate, also known as PMM, acrylic, plexiglass, and lucite. Supplied by Nordic Plastics Group AB, Bronsyxegatan 6, SE-213 75 Malmoe, Sweden.

[20] EJ 510 reflective paint, https://eljentechnology.com/products/accessories/ej-510 [Accessed 1 June 2022].

[21] Electron Tubes type 9821KB, https://et-enterprises.com/products/photomultipliers/product/p9821b-series [Accessed 1 June 2022].

[22] J. Scherzinger, et al., Appl. Radiat. Isop. 98 (2015) 74, http://dx.doi.org/10.1016/j.apradiso.2015.01.003.

[23] J. Scherzinger, et al., Nucl. Instrum. Methods Phys. Res. A. 840 (2016) 121, http://dx.doi.org/10.1016/j.nima.2016.10.011.

[24] CAEN N858 dual attenuator, https://www.caen.it/products/n858/ [Accessed 1 June 2022].

[25] Modern Neutron Detection, TECDOC Series (1935), International Atomic Energy Agency, Vienna, Austria, 2020, ISBN 978-92-0-126520-3.

[26] CAEN VX1751 Waveform Digitizer, https://www.caen.it/products/vx1751/ [Accessed 01 June 2022].

[27] H. Perrey, et al., Nuclear Physics Pulse Processing Library, available at https://gitlab.com/ANPLU/nppp [Accessed 01 June 2022].

[28] G. van Rossum, F.L. Drake (Eds.), Python Reference Manual, PythonLabs, 2001, Python 3.8.5 available at https://www.python.org/ [Accessed 1 June 2022].

[29] The Pandas Development Team, Pandas 1.2.3 available at https://pandas.pydata.org/, https://doi.org/10.5281/zenodo.4572994 [Accessed 01 June 2022].

[30] SciPy 1.6.1 available at https://www.scipy.org/, https://doi.org/10.5281/zenodo.4547611 [Accessed 2022, Jun. 01].

[31] numpy 1.20.3 available at https://pypi.org/project/numpy/ [Accessed 01 June 2022].

[32] G.F. Knoll (Ed.), Radiation Detection and Measurement, second ed., Wiley, New York, U.S.A, 1989, p. 222, ISBN 9780471815044.

[33] A. Jhingan, et al., Nucl. Instrum. Methods Phys. Res. A. 585 (2008) 165, http://dx.doi.org/10.1016/j.nima.2007.11.013.

[34] A. Lavagno, et al., Nucl. Instrum. Methods Phys. Res. A. 617 (2010) 492, http://dx.doi.org/10.1016/j.nima.2009.10.111.

[35] H.H. Knox, et al., Nucl. Instrum. Methods Phys. Res. A. 101 (1972) 519, http://dx.doi.org/10.1016/0029-554X(72)90040-7.

[36] S. Agostinelli, et al., Nucl. Instrum. Methods Phys. Res. A. 506 (2003) 250, http://dx.doi.org/10.1016/S0168-9002(03)01368-8.

[37] J. Allison, et al., IEEE Trans. Nucl. Sci. 53 (2006) 270, http://dx.doi.org/10.1109/TNS.2006.869826.

[38] N. Mauritzson, et al., Nucl. Instrum. Methods Phys. Res. A. 1023 (2022) 165962, http://dx.doi.org/10.1016/j.nima.2021.165962.

[39] R.O. Owens, Nucl. Instrum. Methods Phys. Res. A. 288 (1990) 574, http://dx.doi.org/10.1016/0168-9002(90)90154-X.

[40] Canberra model GC2018 HPGe, https://www.canberra.com [Accessed 01 June 2022].

Paper IV

Light-yield response of liquid scintillators using $2 - 6$ MeV tagged neutrons

N. Mauritzson[a], K.G. Fissum[a,b,*], J.R.M. Annand[c], H. Perrey[a], R. Al Jebali[b,c], A. Backis[b,c], R. Hall-Wilton[b,c,d], K. Kanaki[b], V. Maulerova-Subert[a,b], F. Messi[a,2], R.J.W. Frost[a], E. Rofors[a], J. Scherzinger[e]

[a]*Division of Nuclear Physics, Lund University, SE-221 00 Lund, Sweden*
[b]*Detector Group, European Spallation Source ERIC, SE-221 00 Lund, Sweden*
[c]*School of Physics and Astronomy, University of Glasgow, Glasgow G12 8QQ, Scotland, UK*
[d]*Dipartimento di Fisica "G. Occhialini", Università degli Studi di Milano-Bicocca, Piazza della Scienza 3, 20126 Milano, Italy*
[e]*Thermo Fisher Scientific, Industrial Park Frankfurt Hoechst, 65926 Frankfurt am Main, Germany*

Abstract

Neutrons from 2–6 MeV have been used to study the scintillation light-yield response of the scintillators NE 213A, EJ 305, EJ 331, and EJ 321P using time-of-flight and event-by-event waveform digitization. Energy calibration was performed using a GEANT4 model to locate the edge positions of the Compton distributions produced by gamma-ray sources. The simulated light yield for neutrons from a PuBe source was compared to measured recoil proton distributions, where neutron energy was selected by time of flight. This resulted in an energy-dependent Birks parametrization to characterize the non-linear response of organic scintillators to low energy neutrons. The NE 213A and EJ 305 data agree very well with existing data and are reproduced well by the simulation. New results for EJ 331 and EJ 321P, where the simulation also reproduces the data well, are presented.

Keywords: NE 213A, EJ 305, EJ 331, EJ 321P, scintillator, time-of-flight, light yield, simulation

*Corresponding author. Telephone: +46 46 222 9677; Fax: +46 46 222 4709
[1]present address: CERN, European Organization for Nuclear Research, 1211 Geneva, Switzerland and Hamburg University, D-20148 Hamburg, Germany
[2]present address: Svensk Kärnbränslehantering AB, Evenemangsgatan 13, Box 3091, SE-169 03 Solna, Sweden

1. Introduction

The detection of fast neutrons in fields of gamma-rays is often accomplished using organic liquid scintillators. The organic liquid scintillator NE 213 [1] and its more recent derivative NE 213A [2] have been used widely [3]. The performance of these organics is often employed as a benchmark in the development of fast-neutron detector materials and systems [4–7]. More recently developed liquid scintillators include the high scintillation-light yield EJ 305 [8] and EJ 309 [9], EJ 331 [10] (which includes a thermal-neutron sensitive gadolinium additive), and EJ 321P [11] (a mineral oil based scintillator with a 2:1 hydrogen:carbon ratio). Recently, a GEANT4 model [12] was developed to facilitate the gamma-ray energy calibration of these types of detectors [13]. In this work, the GEANT4 model was extended to include the neutron scintillation-light yield with an energy-dependent Birks parameter. The time-of-flight technique and a polychromatic neutron source were employed to measure the scintillator responses as a function of incident neutron energy. The simulated neutron scintillation-light yield corresponding to the maximum neutron-energy deposition was compared to the measured scintillation yield at the edge of the recoil proton distribution. This edge corresponds to all of the kinetic energy of the incident neutron being transferred to a scintillator proton in a single collision. In this paper, a detailed study of the light yield of the NE 213A, EJ 305, EJ 331, and EJ 321P scintillators is presented. Results for NE 213 and EJ 305 are compared with previous studies and first results are presented for EJ 331 and EJ 321P.

2. Apparatus

2.1. PuBe-based neutron and gamma-ray source

A ^{238}Pu/^{9}Be (PuBe) source provided the fast neutrons used here. ^{238}Pu decays via α-particle emission to ^{234}U producing α particles of the energy around 5.5 MeV [14]. A cascade of low-energy gamma-rays is emitted from the subsequent de-excitation of ^{234}U to the ground state. α-particles which interact with ^{9}Be via the $\alpha + {}^9\text{Be} \rightarrow {}^{12}\text{C} + \text{n}$ reaction have a maximum kinetic energy of $\sim$11 MeV, with the recoiling ^{12}C left in the first-excited state $\sim$50% of the time. A 4.44 MeV gamma-ray is emitted from the subsequent de-excitation of ^{12}C* to the ground state. Thus, the radiation associated with PuBe includes fast neutrons with energies up to $\sim$11 MeV, low-energy cascade gamma-rays, and

2

energetic 4.44 MeV gamma-rays. Energy conservation restricts the maximum energy of neutrons emitted in coincidence with a 4.44 MeV gamma-ray to around 6 MeV. The neutrons are "tagged" if both particles are detected, as the coincident 4.44 MeV gamma-ray provides a reference for a neutron time-of-flight (TOF) measurement. The PuBe source emitted $\sim$2.9 $\times$ 10^6 neutrons per second [15] nearly isotropically, see Ref. [16].

2.2. Detectors

2.2.1. Gamma-ray trigger detectors

In the MeV energy range, Yttrium Aluminum Perovskit:Cerium (Ce^+ doped $YAlO_3$, YAP:Ce) [17] inorganic crystals have good gamma-ray detection efficiency and low efficiency for neutrons. Four YAP:Ce detectors from Scionix [18] were positioned $\sim$10 cm from the PuBe source. They detected both the low-energy cascade and 4.44 MeV gamma-rays. The cylindrical crystals were 1 in. $\times$ 1 in. (diameter $\times$ height) and were attached to a 1 in. Hamamatsu Type R1924 PMT [19]. Gamma-rays from a ^{22}Na source (E_γ = 1.28 MeV) were used to set the gains of the YAP:Ce detectors at an operating HV close to -750 V.

2.2.2. Fast-neutron/gamma-ray detectors

The liquid scintillators were contained in identical cylindrical aluminum cells (94 mm in diameter $\times$ 62 mm deep, $\sim$430 cm^3 detection volume, wall thickness 3 mm). A TiO_2-based reflector (EJ 520 [20]) coated the inside of each cell. Optical windows consisted of 5 mm thick borosilicate glass disks [21] glued to each cell using Araldite 2000+ [22]. The cells were filled through ports which were then sealed with Viton O-rings [23] compressed with aluminum screws. The cells were dry fitted (without optical coupling medium) to a cylindrical PMMA UVT [24] lightguide (72.5 mm in diameter $\times$ 57 mm long). TiO_2-based reflector (EJ 510 [25]) was used to coat the external curved surfaces of the light guide and each assembly was dry fitted to a 3 in. diameter Electron Tubes type 9821KB PMT [26]. A set of springs was used to hold the cell, lightguide and PMT face in contact and a mu-metal magnetic shield was was fitted around the PMT. The PMTs were operated at about -2 kV, the HV employed in previous investigations [7, 16, 27, 28]. The signal amplitudes were adjusted using variable attenuators (CAEN type N858 [29]). Typical 1 MeV_{ee} signals had amplitudes of about -700 mV, risetimes of $\sim$5 ns, and falltimes of $\sim$60 ns. Four different liquid scintillators were employed:

- NE 213A, a pseudocumene-based variant of the organic NE 213 developed for neutron/gamma-ray discrimination.

- EJ 305, a pseudocumene-based organic similar to NE 224 [30] and BC 505 [31] with a high scintillation-light yield.

- EJ 331, a pseudocumene-based organic doped with gadolinium (1.5% by weight)[3]

- EJ 321P, a mineral-oil based scintillator with a hydrogen-to-carbon ratio larger than 2.

Selected liquid-scintillator properties are presented in Table 1.

Table 1: Selected scintillator properties.

Scintillator	NE 213A	EJ 305	EJ 331[4]	EJ 321P
Density [g/cm^3]	∼0.87	∼0.89	∼0.89	∼0.85
Light Yield (% Anthracene)	∼75%	∼80%	∼68%	∼21%
Peak emission wavelength [nm]	420	425	424	425
Flash point [°C]	∼54	∼45	∼44	∼115
H/C ratio	∼1.21	∼1.33	∼1.32	∼2.06
Gadolinium content [%w/w]	-	-	1.5%	-

2.3. Experimental setup

2.3.1. Apparatus

Figure 1 shows the experimental setup. A water-filled shielding cube known as the "Aquarium" [32] housed the PuBe source. Each side wall of the cube had a central cylindrical penetration (17 cm in diameter × 50 cm in length) which allowed a mixed beam of fast neutrons and gamma-rays to escape. Four YAP:Ce detectors were placed at a distance of ∼10 cm from the center of the source which was centered on the beam port. A Pb-shielding hut was constructed outside of one of the beam ports which contained the liquid-scintillator detectors positioned at a distance of 92.5 cm from the center of the PuBe source. The symmetry axis of the neutron detector was aligned parallel to the beam port and pointed directly at the source. The background rate inside the Pb-shielding hut

---

[3]The base scintillator is taken to be EJ 309.
[4]These properties correspond to the data sheet for EJ 331 (0.5 Gd %w/w)

4

was measured to be $<1\,\text{Hz}$ with a 1.5 in. CeBr$_3$ detector ($-600\,\text{V}$, $-50\,\text{mV}$ threshold). In comparison, the neutron detectors showed a background rate of $<100\,\text{Hz}$ (-2 kV, $-25\,\text{mV}$ threshold). A $\sim$10x10 mm^2 aperture was left in the face of the Pb shielding to allow for the measurement of both the low-energy cascade gamma-rays and energetic 4.44 MeV gamma-rays. Two classes of event were of particular interest, see Ref. [27]:

1. "tagged-neutron" events: a fast neutron detected in the neutron detector in correlation with a 4.44 MeV gamma-ray detected in a YAP:Ce detector.
2. "gamma-flash" events: a low-energy cascade gamma-ray detected in the neutron detector in correlation with a 4.44 MeV gamma-ray detected in a YAP:Ce detector.

5
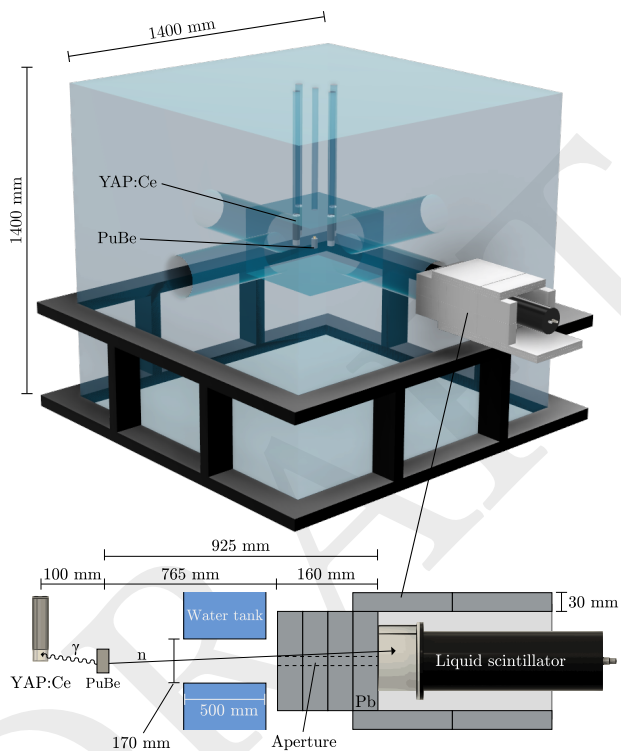
Figure 1: Experimental setup. Top (to scale): 3D rendering of the water tank (Aquarium, blue) and support frame (black) which housed the PuBe source. YAP:Ce detectors and the Pb-shielded liquid scintillator detector are also shown. Bottom (not to scale): Side view of detector setup. The PuBe source emitted correlated 4.44 MeV gamma-ray/fast-neutron pairs. A ~10x10mm^2 aperture in the shielding enabled gamma-flash measurements used to calibrate the TOF measurements.

6

2.3.2. Electronics and data acquisition

Liquid scintillator pulses were recorded using a CAEN VX1751 Waveform Digitizer [33]. A trigger point was set at $-25\,\mathrm{mV}$ on the falling edge of the pulse. This started a $1\,\mu\mathrm{s}$ wide acquisition window over which 10^3 voltage samples were digitised with 10-bit precision on a dynamic range of 1 V. Software tools [34] for waveform analysis based on the `Python` [35] code libraries `numpy` [36], `SciPy` [37] and `pandas` [38] were developed and employed. The event timing marker for each pulse was determined with an interpolating zero-crossover method [39] which largely removed the the time walk associated with the internal falling-edge trigger. Figure 2 shows the resulting waveform after the signal baseline was subtracted. The effective total signal charge ($6.35\pm5.5\%$ fC/channel) was determined by integrating each pulse over 500 ns starting 25 ns before the event-timing marker.
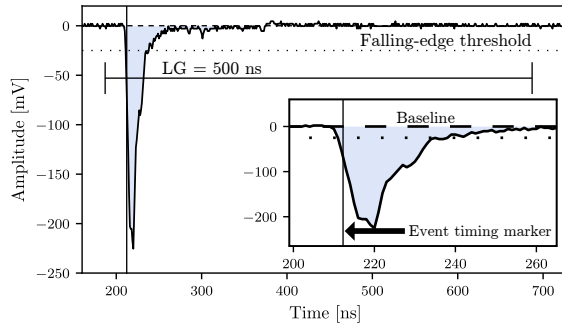

Figure 2: Digitized waveform. The displayed signal has a riseime of $\sim$5 ns, an amplitude $\sim$230 mV, and a falltime of $\sim$50 ns. The falling-edge trigger point set to -25 mV is shown as a dotted line. The event timing marker and the 500 ns integration window are also shown.

7

2.4. Scintillation simulation and calibration

2.4.1. Simulation

For a particle of energy E that stops in a scintillator, the scintillation light yield is given by

$$L(E) = \int_0^R \frac{dL}{dx} dx, \tag{1}$$

where $\frac{dL}{dx}$ is the scintillation gradient with respect to the position increment dx and R is the particle range. For minimum-ionizing particles such as the electrons produced by the gamma-ray sources employed here, the scintillation gradient is

$$\frac{dL}{dx} = S \frac{dE}{dx}, \tag{2}$$

where S is the scintillation efficiency and $\frac{dE}{dx}$ is the specific electron energy loss. For minimum-ionizing particles such as electrons above $\sim$100 keV, $L(E)$ is linear and it is convenient to express L in terms of E_{ee} (equivalent electron energy, units MeV$_{ee}$). In contrast, non minimum-ionizing particles have non-linear scintillation gradients given by the Birks formula [40], which is often modified with the Chou correction [41] to improve agreement with data at lower energies

$$\frac{dL}{dx} = S \frac{\frac{dE}{dx}}{1 + kB\frac{dE}{dx} + C\left(\frac{dE}{dx}\right)^2}. \tag{3}$$

Here, kB is the Birks parameter and C is the Chou correction. The scintillation light yield is quenched with respect to minimum-ionizing electrons having the same specific energy loss. Standard GEANT4 models the scintillation yield without the Chou correction ($C = 0$). For reproducibility, rather than modifying GEANT4 to include the C term, an energy-dependence in kB was permitted.

Simulations of the detector response to gamma-rays and neutrons were performed using GEANT4 [12] version 4.10.04 [42] patch 03 (8 February 2019) using a physics list based on the electromagnetic physics classes `G4EmStandardPhysics` and `G4EmExtraPhysics`, the hadronic physics class `FTFP_BERT_HP`, and optical photon class `G4OpticalPhysics`. Scintillation photons were produced along the tracks of secondary charged particles, electrons from gamma-rays and protons or ^{12}C from neutrons. Photons which reached the photocathode of the PMT generated photoelectrons with a probability derived from the wavelength-dependent quantum efficiency [26] of the PMT. The photoelectron yield as a

8

function of incident energy is effectively a pulse-height distribution which can be compared to the measured data.

2.4.2. Energy calibration

The scintillation-light yield produced by gamma-rays in scintillating liquids below pair-production threshold is dominated by Compton scattering due to the low average Z value of the constituent atoms of the scintillator. Although pair production becomes increasingly important as the gamma-ray energy increases above threshold, the Compton edge remains an invaluable feature for calibration of the pulse-height spectrum. The sources listed in Table 2 were placed in front of each neutron detector and spectra were obtained for run times of about one hour. The measured deadtime and pileup were negligible as the count rates were low ($<$ 1 kHz), and gain drift was corrected for offline. Background subtraction was performed after a real-time normalization.

Table 2: Calibration gamma-ray sources. Distances, gamma-ray energies, and Compton-edge energies E_{CE} are listed.

Source	Distance [cm]	E_γ [MeV]	E_{CE} [MeV$_{ee}$]
^{137}Cs	50	0.66	0.48
^{232}Th	50	2.62	2.38
^{241}Am/^{9}Be (AmBe)	200	4.44	4.20

For the full Geant4 simulations of the gamma-ray response, the only free parameter[5] was the scale factor necessary to match the distribution of simulated photoelectrons at the photocathode of the PMT to the pulse-height spectrum measured by the detector. The simulated locations of the Compton edges were determined by selecting events where the electron energy is less than 2 keV from E_{CE} [13].

---

[5]Smearing due to electronic jitter, extended source, and finite detector volume was also included.
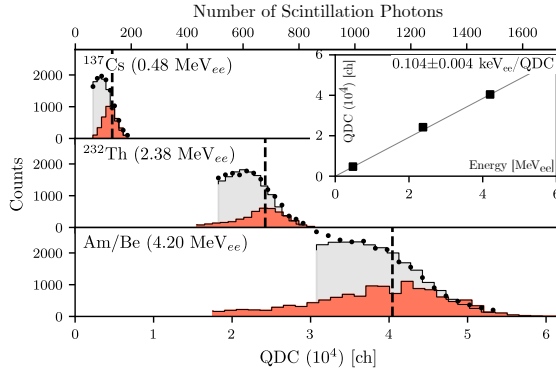
9

Figure 3: Energy calibration for NE 213A. Measured and simulated Compton distributions for three gamma-ray energies. Main plot: measurement (filled circles), simulation (gray shaded histograms), simulation with a very restrictive cut on the Compton edge (red shaded histograms). The mean values of the red shaded distributions are shown by the vertical dashed lines. Inset: the resulting QDC calibration. The uncertainties are smaller than the data points. For interpretation of the references to color in this figure caption, the reader is referred to the web version of this article.

2.5. Event selection

Figure 4 shows a typical energy-deposition correlation between a YAP:Ce and liquid scintillator (NE 213A) detector. The gain of the YAP:Ce detector was set using the full-energy peak of the 1.28 MeV gamma-ray from ^{22}Na and the Compton edge of the 4.44 MeV gamma-ray from PuBe. A 3 MeV$_{ee}$ threshold cut for the YAP:Ce detector allowed for the straightforward selection of 4.44 MeV gamma-rays, corresponding to neutron emission. The intense low-energy gamma-ray field at the center of the the water cube prevented selection of lower energy cascade gamma-rays, which in principle could correspond to higher energy neutrons. A 100 keV$_{ee}$ threshold was applied to the NE 213A detector.
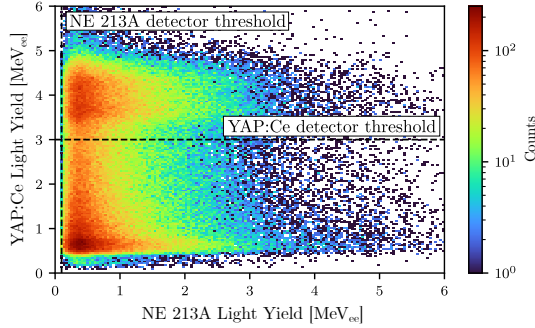
10

Figure 4: Calibrated scintillation light yields, YAP:Ce and NE 213A. The dashed lines are the detector thresholds, 3 MeV$_{ee}$ (YAP:Ce) and 100 keV$_{ee}$ (NE 213A). The events lying above the YAP:Ce threshold are candidate tagged neutrons. Figure from Ref. [43].

3. Results

Figure 5 shows a neutron TOF distribution obtained for a $\sim$96 cm drift distance between the PuBe source and the NE 213A detector. The time T_0 located at 0 ns indicates the instant of emission of the gamma-ray/gamma-ray (gamma flash) or gamma-ray/fast-neutron (tagged neutron) pairs from the PuBe source. T_0 is extrapolated from the gamma flash timing to the right of T_0 at $\sim$2.9 ns. The combination of electronic jitter, extended source, and finite detector volumes gives rise to the $\sim$1 ns width of the peak. The rightmost feature represents tagged neutrons. The flat distribution corresponds to uncorrelated signals in the YAP:Ce and liquid scintillator and the contribution of this random distribution was subtracted from the tagged-neutron distribution using an analysis technique employed for tagged-photon experiments [44].
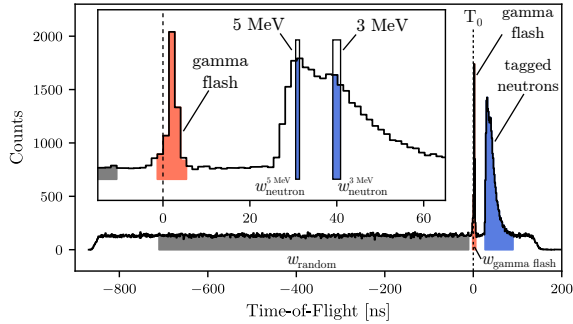
11

Figure 5: TOF spectrum, NE 213A. Main plot: the full range of the digitization window, displaying T_0 (vertical dashed line), gamma flash (sharp red peak) and neutron distribution (broader blue peak). The gray shaded region of the flat random background was employed for random subtraction. Inset: region-of-interest. The blue vertical rectangles illustrate the TOF range corresponding to 250 keV neutron-energy bins centered at 3 and 5 MeV.

Neutron TOF was converted to neutron kinetic energy on an event-by-event basis. Standard GEANT4 does not handle the inclusion of the Chou correction to the Birks formula, and thus kB was allowed to vary. For each scintillator and each neutron energy $2 - 6$ MeV in 0.5 MeV bins, the simulation was aligned with the data using a least-squares minimization to obtain the optimum value of kB. Additional fine-tuning in the agreement was provided by smearing the simulated scintillation light yield for each neutron energy bin. Smearing on average ranged from ∼35% at 2 MeV to ∼5% at 6 MeV, for all scintillators. Figure 6 shows the agreement between data and simulation over the entire energy range before and after kB optimization. Also illustrated are values of kB extracted using the optimization procedure, together with the a $1/T_n$ fit which follows the extracted kB values quite well. The trend in kB is used in the simulations.
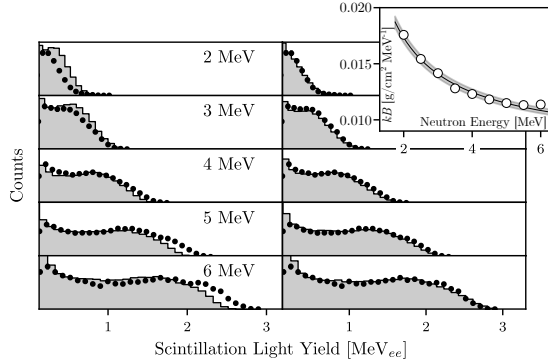
12

Figure 6: Scintillation light yield, EJ 305. Measured calibrated scintillation light yield (filled circles) and simulations (shaded histograms) shown before (left) and after (right) optimization. The uncertainties are smaller than the data points. The inset shows the variation in kB as a function of neutron kinetic energy.

Figure 7 shows the neutron scintillation light yield from EJ 305, for the measured data, the full simulation, and the simulated maximum neutron-energy deposition (SMD). To determine the SMD, point source, non-divergent, monoenergetic (pencil) neutron beams were directed at the center of the scintillator cells. For each incident neutron-beam energy, the energy deposited by recoiling protons as the neutrons traversed the cell was recorded. A 1% cut on the high-energy edge proton-energy distribution was then enforced to populate the scintillation light-yield spectra corresponding to the SMD. The SMD distributions were then fitted with a Gaussian function and $\pm 3\sigma$ from the mean was used to determine the average of the SMD distribution.

13
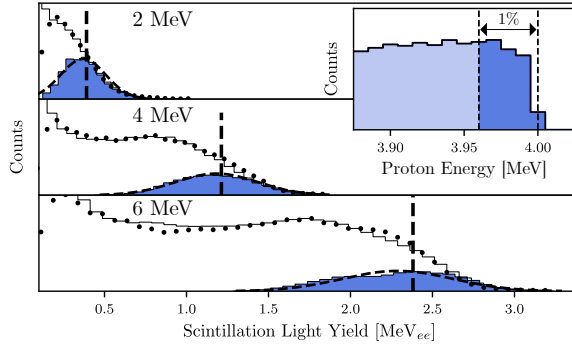
Figure 7: Simulated maximum neutron-energy depositions, EJ 305. Main plot: measured scintillation light yield (filled circles) and full simulations (open histograms) for incident neutron energies 2, 4, 6 MeV. Inset: simulated proton recoil energy for a 4 MeV pencil neutron beam incident at the centre of the detector. The dark shaded region between the vertical dashed lines in the inset corresponds to a 1% energy cut and results in the dark shaded simulated scintillation light yield in the middle panel. Fitted Gaussian functions (dashed trends) are shown together with the SMD locations (vertical dashed lines). The uncertainties are smaller than the data points.

Figure 8 shows a comparison between the data, the full simulations, the SMD simulations, and the corresponding SMD values for all scintillators. The neutron-energy bins centered at 3 and 5 MeV were ±0.125 MeV wide.
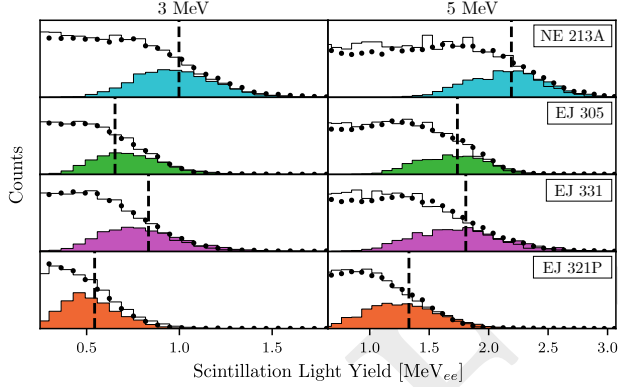
14

Figure 8: Simulated maximum depositions, all scintillators. Measured scintillation light yield (filled circles) and full simulations (open histograms) together with the SMD simulations (colored histograms). The SMD locations are shown as vertical dashed lines. The uncertainties are smaller than the data points.

In addition to simulation-based approaches such as the one detailed above, phenomenological parameterizations of neutron scintillation light yield based upon the specific energy loss of protons (E_p) have been used to characterize measured spectra. The correlation between recoiling electron (L_{ee}) and quenched recoiling proton ($L(E_p)$) scintillation light yields was determined by Cecil *et al.* [45] for NE 213 to be

$$L(E_p) = L_{ee} = K \left[p_1 E_p - p_2 \left(1 - e^{-p_3 E_p^{p_4}} \right) \right], \qquad (4)$$

while, Kornilov *et al.* [46] suggested

$$L(E_p) = L_{ee} = L_0 \frac{E_p^2}{E_p + L_1}, \qquad (5)$$

where K and L_0 are adjustable scaling parameters and p_{1-4} and L_1 are material specific light yield parameters. The maximum energy the incident neutron can transfer to the recoiling proton in a single scatter may be determined using three different methods to locate the high-energy edge of the scintillation distribution (see for example Ref. [28]):

1. The half-height (HH) method [47] involves fitting a Gaussian function to the edge

15

of the recoil-proton distribution and selecting the half maximum as the location of the maximum proton energy transfer.

2. The turning-point (TP) method also involves fitting a Gaussian function, but here the minimum of the first derivative of the function is selected as the maximum edge.

3. The first-derivative (FD) method [46] involves taking the first derivative of the distribution and selecting the minimum point as the edge. The first derivative was evaluated by considering five adjacent bins above and below each data point.

For the purposes of comparison, the SMD employed in the simulation-driven analyses of scintillation light yield may be compared with the maximum proton recoil edge employed in these data-driven analyses. Figure 9 shows an illustration of the scintillation light yields from 4 MeV neutrons with the SMD and HH, TP, and FD recoil-proton edge locations indicated. While the HH, TP, and FD locations generally have the same relative locations with respect to one another regardless of the neutron energy bin, the relative location of the SMD varies with neutron energy.
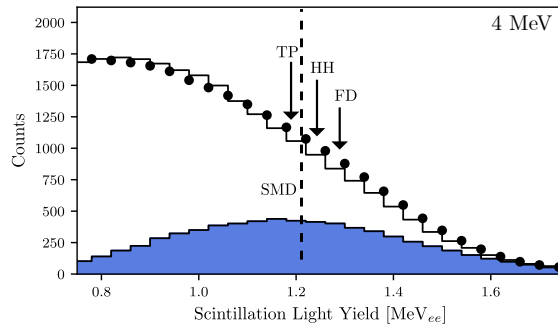

Figure 9: Simulated maximum depositions and proton edge locations, EJ 305. Measured scintillation light yield (filled circles) and full simulation (open histogram) together with the SMD simulation (shaded histogram) and the SMD location (dashed line) are shown. The vertical arrows indicate the maximum recoil proton edges as predicted by the HH, TP and FD methods.

For NE 213A and EJ 305, parameterization coefficients corresponding to NE 213 [45] (NE 213A equivalent) and EJ 309 [48] (EJ 305 equivalent) were employed to determine the light yield curves corresponding to Eq. 4 (Cecil *et al.*). The base organic in EJ 331 was assumed to be EJ 309, see Table 3. In the absence of previously published results, the parameterization coefficients p_{1-4} for EJ 321P were determined by fitting to the HH, TP and FD scintillation light yields. The results were averaged and fixed as constants. K was subsequently determined with these constants. The L_1 coefficients were similarly determined by fitting to the data using Eq. 5 (Kornilov *et al.*), for all four scintillators. First, the HH, TP and FD neutron scintillation light yields were fitted allowing both L_0 and L_1 to vary. The resulting L_1 parameters for HH, TP, and FD were then averaged and fixed as an L_1 constant. In comparison, Scherzinger *et al.* [28] report $L_1 = 2.48$ for NE 213 and Enqvist *et al.* [48] report $L_1 = 5.95$ for EJ 309.

Table 3: Fixed scintillator parametrization coefficients.

| Scintillator | Eq. 4, Cecil | | | | Eq. 5, Kornilov |
	p_1	p_2	p_3	p_4	L_1
NE 213A (NE 213 [45])	0.83	2.82	0.25	0.93	3.67 ± 0.19
EJ 305 (EJ 309 [48])	0.817	2.63	0.297	1	6.55 ± 0.38
EJ 331 (EJ 309 [48])	0.817	2.63	0.297	1	5.34 ± 0.48
EJ 321P	0.43 ± 0.01	0.77 ± 0.04	0.26 ± 0.07	2.13 ± 0.43	6.68 ± 0.82

Figure 10 shows the measured scintillation light yield as a function of recoil proton energy for NE 213A. The SMD methods for determining the maximum recoil proton edge is compared with the HH, TP and FD methods. A summary of the fixed parameters employed in the fitted functions may be found in Table 3. The scintillation light yield increases as a function of recoil proton energy, but not linearly due to quenching. There is little sensitivity to the methods (HH, FD) used to determine the recoil-proton edge, and the SMD approach does an excellent job of reproducing the TP data while underestimating the light yields of the HH and FD methods by up to ∼6%.

17

Figure 10: Comparison of recoil-proton light yield for NE 213A. Results have been obtained using the SMD (filled triangles), HH (top panel, open circles), TP (middle panel, open circles) and FD (bottom panel, open circles) methods. The Kornilov (Eq. 5) parameterizations are shown for the measured data (solid lines) and SMD method (dashed lines), respectively. The SMD method results are the same in all three panels. The uncertainties are smaller than the data points.

Figure 11 presents a comparison between the NE 213A SMD results detailed above

and the scintillation light yield for NE 213 measured by both Gagnon-Moisan *et al.* [49] and Scherzinger *et al.* [28]. Agreement between the data sets and the SMD prescription is very good. The classic scintillator NE 213A appears to be well understood in this energy region.
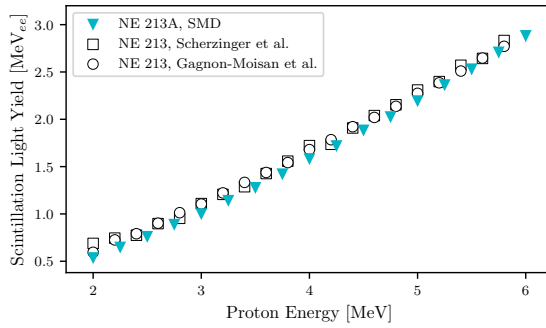
Figure 11: Comparison of recoil-proton light yield measurements for NE 213A. Results include SMD approach (filled triangles), Gagnon-Moisan *et al.* [49] (open circles), Scherzinger *et al.* [28] (open squares). The uncertainties are smaller than the data points.

Figure 12 shows trends in the measured scintillation light yield for EJ 305 as a function of recoil proton energy between the SMD and HH, TP and FD methods. Here again, there is little sensitivity to the method (HH, FD) used to determine the recoil proton edge, and the SMD approach does an excellent job of reproducing the TP data while underestimating the light yields of the HH and FD methods by up to ∼8%.
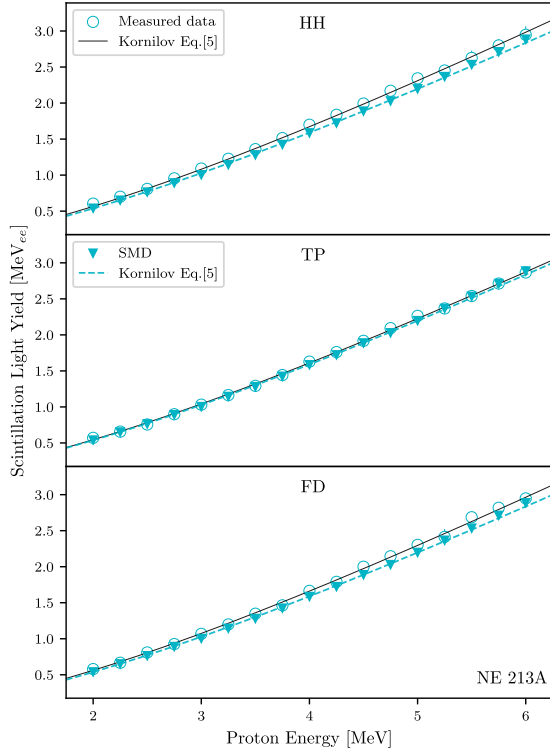
Figure 12: Comparison of recoil-proton light yield for EJ 305. Results have been obtained using the SMD (filled triangles), HH (top panel, open circles), TP (middle panel, open circles) and FD (bottom panel, open circles) methods. The Kornilov (Eq. 5) parameterizations are shown for the measured data (solid lines) and SMD method (dashed lines), respectively. The SMD method results are the same in all three panels. The uncertainties are smaller than the data points.

Figure 13 presents a comparison between the EJ 305 SMD prescription and the scintillation light yields for NE 224 (EJ 305 equivalent) measured by both Czirr *et al.* [50] and Madey *et al.* [30] together with the parameterization for BC 505 (EJ 305 equivalent) determined by Pywell *et al.* [51]. The dash-dotted line represents the Pywell *et al.* parameterization scaled by 0.76, determined by least-squares minimization. The scaled parameterization underestimates the scintillation light yields measured in NE 224 before 1980 and shows a slightly weaker scintillation light-yield gradient than the SMD predictions. This comparison between NE 224, BC 505, and EJ 305 may not be optimal but nevertheless provides insight.
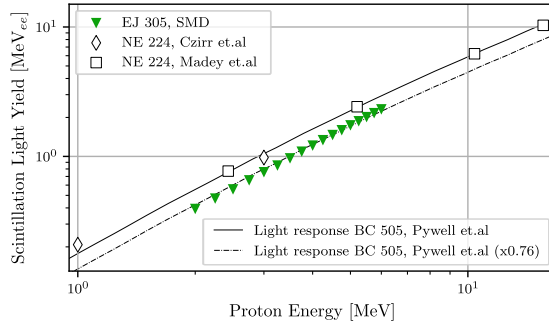
Figure 13: Calibrated neutron scintillation light-yield comparison, EJ 305 (this work), BC 505 and NE 224. The NE 224 results of Czirr *et al.* (open diamonds) and Madey *et al.* (open squares) are shown together with the EJ 305 SMD prescription (filled triangles). The uncertainties in the measured data are smaller than the data points.

Figures 14 and 15 show trends in the measured scintillation light yield as a function of recoil proton energy for EJ 331 and EJ 321P, respectively. The manner of presentation is identical to that employed for Figs. 10 and 12 and the trends in the results are similar. The SMD approach does an excellent job of reproducing the TP data for both scintillators while underestimating the light yields of the HH and FD methods by up to ∼5% and ∼7% for EJ 331 and EJ 321P, respectively.
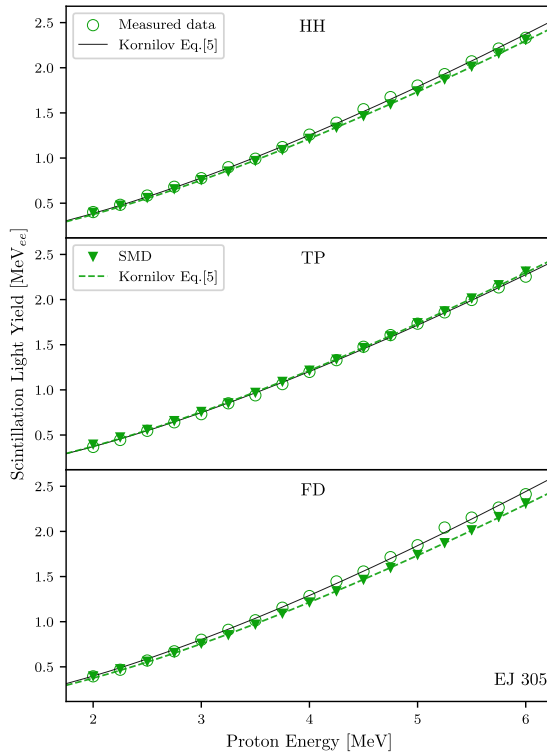
21
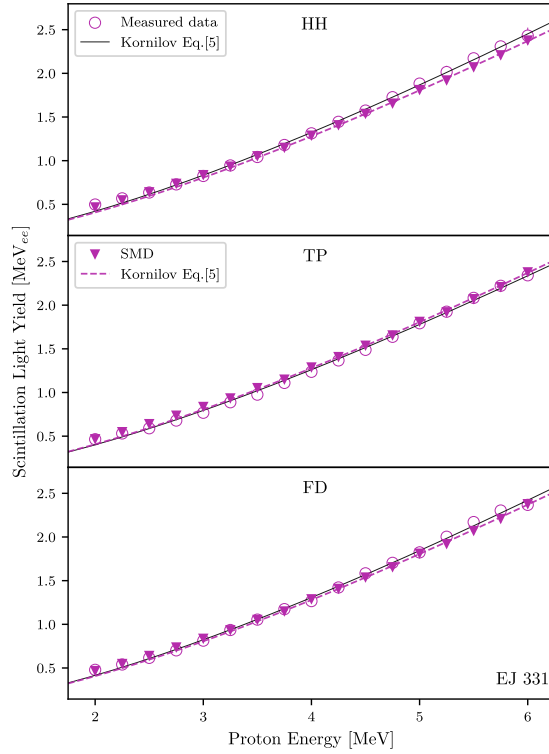
Figure 14: Comparison of recoil-proton light yield for EJ 331. Results have been obtained using the SMD (filled triangles), HH (top panel, open circles), TP (middle panel, open circles) and FD (bottom panel, open circles) methods. The Kornilov (Eq. 5) parameterizations are shown for the measured data (solid lines) and SMD method (dashed lines), respectively. The SMD method results are the same in all three panels. The uncertainties are smaller than the data points.
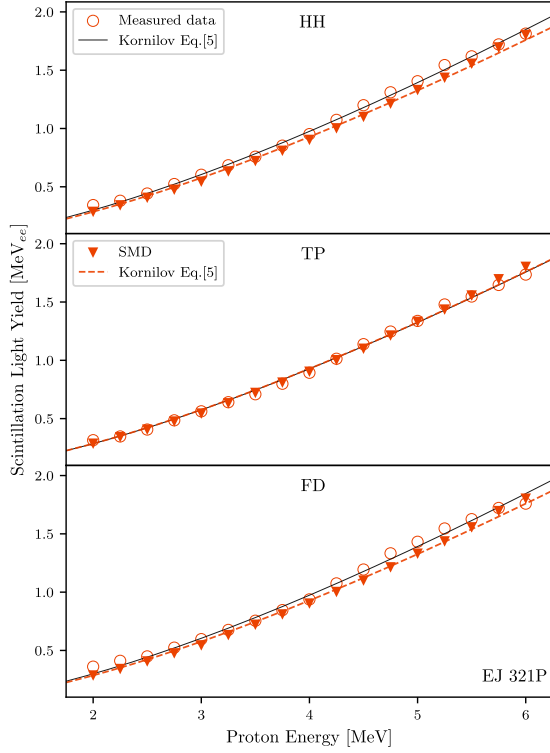
Figure 15: Comparison of recoil-proton light yield for EJ 321P. Results have been obtained using the SMD (filled triangles), HH (top panel, open circles), TP (middle panel, open circles) and FD (bottom panel, open circles) methods. The Kornilov (Eq. 5) parameterizations are shown for the measured data (solid lines) and SMD method (dashed lines), respectively. The SMD method results are the same in all three panels. The uncertainties are smaller than the data points.

Table 4 presents a summary of the K and L_0 results extracted from fitting the Cecil and Kornilov curves using the fixed parameters described in Table 3 to the scintillation light yield data and SMD results shown in Figs. 10, 12, 14, and 15. While generally not consistent within uncertainty, there is little to distinguish between the K and L_0 coefficients resulting from the different methods for determining the recoil proton edges. The NE 213A results are systematically ∼3% lower for K and about ∼8% higher for L_0 than those measured for NE 213 by Scherzinger *et al.* [28]. This is due to the fact a different L_1 has been employed in this work. The K and L_0 coefficients corresponding to the SMD results tend to be systematically lower than the data-driven results by ∼5%.

Table 4: Fitted scintillation parameterization coefficients. "Edge" denotes the method used to determine the maximum proton transfer edge. The factors K and L_0 are from Eqs. 4 and 5, respectively. The fixed parameters employed may be found in Table 3.

Scintillator	Edge	K	χ^2/d.o.f.	L_0	χ^2/d.o.f.
NE213A	HH	1.02 ± 0.01	1.6	0.80 ± 0.01	2.4
	TP	0.98 ± 0.01	4.7	0.77 ± 0.01	1.8
	FD	1.01 ± 0.01	1.8	0.80 ± 0.01	0.7
	SMD	0.97 ± 0.01	2.2	0.76 ± 0.01	0.4
EJ305	HH	0.87 ± 0.01	0.4	0.83 ± 0.01	0.7
	TP	0.84 ± 0.01	1.3	0.79 ± 0.01	0.7
	FD	0.90 ± 0.01	1.1	0.85 ± 0.01	0.7
	SMD	0.84 ± 0.01	0.1	0.80 ± 0.01	0.3
EJ331	HH	0.91 ± 0.01	24.5	0.77 ± 0.01	20.1
	TP	0.87 ± 0.01	11.3	0.74 ± 0.01	10.0
	FD	0.90 ± 0.01	3.5	0.76 ± 0.01	2.9
	SMD	0.88 ± 0.01	4.7	0.75 ± 0.01	3.2
EJ321P	HH	1.02 ± 0.01	1.3	0.65 ± 0.01	7.2
	TP	0.97 ± 0.01	1.2	0.62 ± 0.01	3.2
	FD	1.02 ± 0.01	1.7	0.65 ± 0.01	4.5
	SMD	0.97 ± 0.01	3.2	0.62 ± 0.01	1.8

4. Summary and discussion

Beams of energy-tagged neutrons from 2–6 MeV provided by a PuBe source have been used to perform a systematic study of the scintillation light-yield response of the scintilla-

24

tors NE 213A, EJ 305, EJ 331, and EJ 321P. Neutron tagging exploits the $\alpha + {}^9\text{Be} \rightarrow {}^{12}\text{C} + n + \gamma (4.44\,\text{MeV})$ reaction, with the gamma-rays providing a reference for measuring the TOF of the corresponding neutron liquid scintillator. The PuBe source and YAP:Ce gamma-ray detectors were placed within a water-filled shielding cube. The cube employed cylindrical ports to define beams of gamma-rays and fast neutrons. Pb shielding attenuated the majority of the direct gamma-rays from the PuBe and the background gamma-rays from the room (Fig. 1). The analog signals from the detectors were digitized on an event-by-event basis, with the event-timing marker determined using an interpolating zero-crossover method (Fig. 2). Energy calibration of the resulting spectra was performed using a GEANT4 model of the liquid scintillator to locate the position of the Compton edge in the measured gamma-ray spectra from gamma-ray sources (Fig. 3). The correlation between the energy registered in a YAP:Ce gamma-ray detector and the energy deposited in a liquid-scintillator was used to select tagged events (Fig. 4). Neutron energies were determined using a TOF method, and the data were corrected for random background (Fig. 5).

Neutron scintillation light yield was simulated using the same GEANT4 model, and matched to the data by allowing an energy dependence in the Birks parameter (Fig. 6). The simulated yield corresponding to the maximum neutron-energy deposition was determined with a very strict cut on the deposited neutron energy (Fig. 7). The method worked very well (Fig. 8). The relationship between the simulated maximum deposition (SMD) light yield and measured scintillation light yields corresponding to the maximum proton recoil edge was established (Fig. 9). Data and simulation for NE 213A were internally consistent (Fig. 10) and nicely reproduced existing results (Fig. 11). Data and simulation for EJ 305 were also internally consistent (Fig. 12), however they showed a steeper scintillation light-yield gradient compared with paramerization of existing data from the 1980s. Data and simulation for EJ 331 (Fig. 14) and EJ 321P (Fig. 15) were measured for the first time to the knowledge of the authors.

The GEANT4 simulation developed and tested here provides valuable insight into the behavior of the scintillators, and does a very good job of replicating the data. The tagged neutron energy range provided by the PuBe source is relatively small. An accelerator-based neutron generator could be used to extend the results to higher neutron energies. The neutron-tagging technique facilitates the measurement of energy-dependent scintillator response using radioactive neutron sources. The simulation further refines the

25

understanding of the underlying processes.

Acknowledgements

26

References

[1] NE213 is no longer produced. Eljen Technologies EJ-301 or Saint Gobain BC-501 are similar. [link].
URL   `https://eljentechnology.com/products/`
`liquid-scintillators/ej-301-ej-309`

[2] J. Annand, B.-E. Andersson, I. Akkurt, B. Nilsson, An ne213a tof spectrometer for high resolution (γ, n) reaction measurements, Nuclear Instruments and Methods in Physics Research Section A: Accelerators, Spectrometers, Detectors and Associated Equipment 400 (2-3) (1997) 344–355.

[3] R. Batchelor, W. Gilboy, J. Parker, J. Towle, The response of organic scintillators to fast neutrons, Nuclear Instruments and Methods 13 (1961) 70–82. `doi:https://doi.org/10.1016/0029-554X(61)90171-9.`
URL   `https://www.sciencedirect.com/science/article/pii/`
`0029554X61901719`

[4] E. Bayat, N. Divani-Vais, M. Firoozabadi, N. Ghal-Eh, A comparative study on neutron-gamma discrimination with ne213 and ugllt scintillators using zero-crossing method, Radiation Physics and Chemistry 81 (3) (2012) 217–220. `doi:`
`https://doi.org/10.1016/j.radphyschem.2011.10.016.`
URL   `https://www.sciencedirect.com/science/article/pii/`
`S0969806X11003653`

[5] J. Iwanowska, L. Swiderski, T. Szczesniak, P. Sibczynski, M. Moszynski, M. Grodzicka, K. Kamada, K. Tsutsumi, Y. Usuki, T. Yanagida, A. Yoshikawa, Performance of cerium-doped gd3al2ga3o12 (gagg:ce) scintillator in gamma-ray spectrometry, Nuclear Instruments and Methods in Physics Research Section A: Accelerators, Spectrometers, Detectors and Associated Equipment 712 (2013) 34–40. `doi:https://doi.org/10.1016/j.nima.2013.01.064.`
URL   `https://www.sciencedirect.com/science/article/pii/`
`S0168900213001848`

[6] I. Pawełczak, S. Ouedraogo, A. Glenn, R. Wurtz, L. Nakae, Studies of neutron–gamma pulse shape discrimination in ej-309 liquid scintillator using charge integration

27

method, Nuclear Instruments and Methods in Physics Research Section A: Accelerators, Spectrometers, Detectors and Associated Equipment 711 (2013) 21–26. `doi:https://doi.org/10.1016/j.nima.2013.01.028.`
URL `https://www.sciencedirect.com/science/article/pii/S0168900213000880`

[7] R. Jebali, J. Scherzinger, J. Annand, R. Chandra, G. Davatz, K. Fissum, H. Friederich, U. Gendotti, R. Hall-Wilton, E. Håkansson, K. Kanaki, M. Lundin, D. Murer, B. Nilsson, A. Rosborg, H. Svensson, A first comparison of the responses of a 4he-based fast-neutron detector and a ne-213 liquid-scintillator reference detector, Nuclear Instruments and Methods in Physics Research Section A: Accelerators, Spectrometers, Detectors and Associated Equipment 794 (2015) 102–108. `doi:https://doi.org/10.1016/j.nima.2015.04.058.`
URL `https://www.sciencedirect.com/science/article/pii/S0168900215005690`

[8] Ej-305 highest light output liquid scintillator.
URL `http://www.ggg-tech.co.jp/maker/eljen/ej-305.html`

[9] Ej-309 – eljen technology.
URL `https://eljentechnology.com/products/liquid-scintillators/ej-301-ej-309`

[10] Ej-331, ej-335 – gadolinium loaded liquid scintillator – eljen technology.
URL `https://eljentechnology.com/products/liquid-scintillators/ej-331-ej-335`

[11] Ej-321 series – mineral oil based liquid scintillator – eljen technology.
URL `https://eljentechnology.com/products/liquid-scintillators/ej-321-series`

[12] S. Agostinelli, J. Allison, K. Amako, J. Apostolakis, H. Araujo, P. Arce, M. Asai, D. Axen, S. Banerjee, G. Barrand, F. Behner, L. Bellagamba, J. Boudreau, L. Broglia, A. Brunengo, H. Burkhardt, S. Chauvie, J. Chuma, R. Chytracek, G. Cooperman, G. Cosmo, P. Degtyarenko, A. Dell'Acqua, G. Depaola, D. Dietrich, R. Enami, A. Feliciello, C. Ferguson, H. Fesefeldt, G. Folger, F. Foppiano, A. Forti, S. Garelli, S. Giani,

28

R. Giannitrapani, D. Gibin, J. Gómez Cadenas, I. González, G. Gracia Abril, G. Greeniaus, W. Greiner, V. Grichine, A. Grossheim, S. Guatelli, P. Gumplinger, R. Hamatsu, K. Hashimoto, H. Hasui, A. Heikkinen, A. Howard, V. Ivanchenko, A. Johnson, F. Jones, J. Kallenbach, N. Kanaya, M. Kawabata, Y. Kawabata, M. Kawaguti, S. Kelner, P. Kent, A. Kimura, T. Kodama, R. Kokoulin, M. Kossov, H. Kurashige, E. Lamanna, T. Lampén, V. Lara, V. Lefebure, F. Lei, M. Liendl, W. Lockman, F. Longo, S. Magni, M. Maire, E. Medernach, K. Minamimoto, P. Mora de Freitas, Y. Morita, K. Murakami, M. Nagamatu, R. Nartallo, P. Nieminen, T. Nishimura, K. Ohtsubo, M. Okamura, S. O'Neale, Y. Oohata, K. Paech, J. Perl, A. Pfeiffer, M. Pia, F. Ranjard, A. Rybin, S. Sadilov, E. Di Salvo, G. Santin, T. Sasaki, N. Savvas, Y. Sawada, S. Scherer, S. Sei, V. Sirotenko, D. Smith, N. Starkov, H. Stoecker, J. Sulkimo, M. Takahata, S. Tanaka, E. Tcherniaev, E. Safai Tehrani, M. Tropeano, P. Truscott, H. Uno, L. Urban, P. Urban, M. Verderi, A. Walkden, W. Wander, H. Weber, J. Wellisch, T. Wenaus, D. Williams, D. Wright, T. Yamada, H. Yoshida, D. Zschiesche, Geant4—a simulation toolkit, Nuclear Instruments and Methods in Physics Research Section A: Accelerators, Spectrometers, Detectors and Associated Equipment 506 (3) (2003) 250 – 303. doi:https://doi.org/10.1016/S0168-9002(03)01368-8.
URL http://www.sciencedirect.com/science/article/pii/S0168900203013688

[13] N. Mauritzson, K. Fissum, H. Perrey, J. Annand, R. Frost, R. Hall-Wilton, R. A. Jebali, K. Kanaki, V. Maulerova-Subert, F. Messi, E. Rofors, Geant4-based calibration of an organic liquid scintillator, Nuclear Instruments and Methods in Physics Research Section A: Accelerators, Spectrometers, Detectors and Associated Equipment 1023 (2022) 165962. doi:https://doi.org/10.1016/j.nima.2021.165962.
URL https://www.sciencedirect.com/science/article/pii/S0168900221009104

[14] NuDat2.8, National Nuclear Data Center, Brookhaven National Laboratory.
URL http://www.nndc.bnl.gov/nudat2/

[15] Exactly 4.26×10^6 neutrons per second. Calibration certified at The Radiochemical Centre, Amersham, England HP7 9LL on 3 September (1973).

29

[16] J. Scherzinger, R. Al Jebali, J. Annand, K. Fissum, R. Hall-Wilton, S. Koufi-gar, N. Mauritzson, F. Messi, H. Perrey, E. Rofors, A comparison of un-tagged gamma-ray and tagged-neutron yields from 241ambe and 238pube sources, Applied Radiation and Isotopes 127 (2017) 98–102. `doi:https://doi.org/10.1016/j.apradiso.2017.05.014`.
URL `https://www.sciencedirect.com/science/article/pii/S0969804316309861`

[17] M. Moszyński, M. Kapusta, D. Wolski, W. Klamra, B. Cederwall, Properties of the yap : Ce scintillator, Nuclear Instruments and Methods in Physics Research Section A: Accelerators, Spectrometers, Detectors and Associated Equipment 404 (1) (1998) 157–165. `doi:https://doi.org/10.1016/S0168-9002(97)01115-7`.
URL `https://www.sciencedirect.com/science/article/pii/S0168900297011157`

[18] Scionix holland bv.
URL `http://www.scionix.nl`

[19] Hamamatsu photonics.
URL `http://www.hamamatsu.com`

[20] Ej-520 – reflective paint for liquid scintillator cell, [accessed 2022, Dec. 2].
URL `http://www.ggg-tech.co.jp/maker/eljen/ej-520.html`

[21] Borofloat, supplied by Glasteknik i Emmaboda AB, Utvägen 6 SE-361 31 Emmaboda, Sweden.
URL `https://www.schott.com/en-gb/products/borofloat`

[22] Araldite 2000, Araldite is a registered trademark of Huntsman.
URL `http://www.araldite2000plus.com`

[23] Viton o-rings, viton is a registered trademark of DuPont Performance Elastomers LLC.
URL `https://www.oringsusa.com/o/viton/`

30

[24] Poly-methyl-methacrylate, also known as PMM, acrylic, plexiglass, and lucite. Supplied by Nordic Plastics Group AB, Bronsyxegatan 6, SE-213 75 Malmoe, Sweden.

[25] [accessed 2022, Dec. 2]. [link].
URL https://eljentechnology.com/products/accessories/ej-510

[26] [accessed 2022, Dec. 2]. [link].
URL https://et-enterprises.com/images/data_sheets/9821B.pdf

[27] J. Scherzinger, J. Annand, G. Davatz, K. Fissum, U. Gendotti, R. Hall-Wilton, E. Håkansson, R. Jebali, K. Kanaki, M. Lundin, B. Nilsson, A. Rosborge, H. Svensson, Tagging fast neutrons from an 241am/9be source, Applied Radiation and Isotopes 98 (2015) 74–79. doi:https://doi.org/10.1016/j.apradiso.2015.01.003.
URL https://www.sciencedirect.com/science/article/pii/S0969804315000044

[28] J. Scherzinger, R. Al Jebali, J. Annand, K. Fissum, R. Hall-Wilton, K. Kanaki, M. Lundin, B. Nilsson, H. Perrey, A. Rosborg, H. Svensson, The light-yield response of a ne-213 liquid-scintillator detector measured using 2–6 mev tagged neutrons, Nuclear Instruments & Methods in Physics Research. Section A: Accelerators, Spectrometers, Detectors, and Associated Equipment 840 (2016) 121–127. doi:10.1016/j.nima.2016.10.011.

[29] CAEN, N858 dual attenuator.
URL https://www.caen.it/products/n858/

[30] R. Madey, F. M. Waterman, A. R. Baldwin, J. N. Knudson, J. Carlson, J. Rapaport, The response of ne-228a, ne-228, ne-224, and ne-102 scintillators to protons from 2.43 to 19.55 mev, Nuclear Instruments and Methods 151 (3) (1978) 445–450. doi:https://doi.org/10.1016/0029-554X(78)90154-4.
URL https://www.sciencedirect.com/science/article/pii/0029554X78901544

[31] [link].
URL https://www.crystals.saint-gobain.com/sites/hps-mac3-cma-crystals/files/2021-09/BC505-Data-Sheet.pdf

31

[32] Modern Neutron Detection, no. 1935 in TECDOC Series, INTERNATIONAL ATOMIC ENERGY AGENCY, Vienna, 2020.
URL `https://www.iaea.org/publications/14690/modern-neutron-detection`

[33] CAEN, VX1751 4/8 channel 10 bit 2/1 GS/s digitizer.
URL `https://www.caen.it/products/vx1751/`

[34] H. Perrey, N. Mauritzson, R. Kjær Høier, L. Ros, F. Thomson, NPPP – nuclear physics pulse processing library, `https://gitlab.com/ANPLU/nppp` (2020).

[35] Python 3.8.5.
URL `https://www.python.org/`

[36] numpy 1.20.3.
URL `https://pypi.org/project/numpy/`

[37] Pandas 1.6.1. `doi:10.5281/zenodo.4547611`.
URL `https://www.scipy.org/`

[38] Pandas 1.2.3. `doi:10.5281/zenodo.4572994`.
URL `https://pandas.pydata.org/`

[39] G. Knoll, Radiation detection and measurement, Wiley, New York, NY, U.S.A., 1989.

[40] J. B. Birks, Scintillations from organic crystals: Specific fluorescence and relative response to different radiations, Proceedings of the Physical Society. Section A 64 (10) (1951) 874. `doi:10.1088/0370-1298/64/10/303`.
URL `https://dx.doi.org/10.1088/0370-1298/64/10/303`

[41] C. N. Chou, The nature of the saturation effect of fluorescent scintillators, Phys. Rev. 87 (1952) 904–905. `doi:10.1103/PhysRev.87.904`.
URL `https://link.aps.org/doi/10.1103/PhysRev.87.904`

[42] J. Allison, K. Amako, J. Apostolakis, H. Araujo, P. Arce Dubois, M. Asai, G. Barrand, R. Capra, S. Chauvie, R. Chytracek, G. A. P. Cirrone, G. Cooperman, G. Cosmo, G. Cuttone, G. G. Daquino, M. Donszelmann, M. Dressel, G. Folger, F. Foppiano,

32

J. Generowicz, V. Grichine, S. Guatelli, P. Gumplinger, A. Heikkinen, I. Hrivnacova, A. Howard, S. Incerti, V. Ivanchenko, T. Johnson, F. Jones, T. Koi, R. Kokoulin, M. Kossov, H. Kurashige, V. Lara, S. Larsson, F. Lei, O. Link, F. Longo, M. Maire, A. Mantero, B. Mascialino, I. McLaren, P. Mendez Lorenzo, K. Minamimoto, K. Murakami, P. Nieminen, L. Pandola, S. Parlati, L. Peralta, J. Perl, A. Pfeiffer, M. G. Pia, A. Ribon, P. Rodrigues, G. Russo, S. Sadilov, G. Santin, T. Sasaki, D. Smith, N. Starkov, S. Tanaka, E. Tcherniaev, B. Tome, A. Trindade, P. Truscott, L. Urban, M. Verderi, A. Walkden, J. P. Wellisch, D. C. Williams, D. Wright, H. Yoshida, Geant4 developments and applications, IEEE Transactions on Nuclear Science 53 (1) (2006) 270–278. `doi:10.1109/TNS.2006.869826`.

[43] N. Mauritzson, K. Fissum, J. Annand, H. Perrey, R. Frost, R. A. Jebali, A. Backis, R. Hall-Wilton, K. Kanaki, V. Maulerova-Subert, C. Maurer, F. Messi, E. Rofors, Technique for the measurement of intrinsic pulse-shape discrimination for organic scintillators using tagged neutrons, Nuclear Instruments and Methods in Physics Research Section A: Accelerators, Spectrometers, Detectors and Associated Equipment 1039 (2022) 167141. `doi:https://doi.org/10.1016/j.nima.2022.167141`.
URL `https://www.sciencedirect.com/science/article/pii/S0168900222005265`

[44] R. Owens, Statistical treatment of tagged photon experiments, Nuclear Instruments and Methods in Physics Research Section A: Accelerators, Spectrometers, Detectors and Associated Equipment 288 (2) (1990) 574–584. `doi:https://doi.org/10.1016/0168-9002(90)90154-X`.
URL `https://www.sciencedirect.com/science/article/pii/016890029090154X`

[45] R. Cecil, B. Anderson, R. Madey, Improved predictions of neutron detection efficiency for hydrocarbon scintillators from 1 mev to about 300 mev, Nuclear Instruments and Methods 161 (3) (1979) 439–447. `doi:https://doi.org/10.1016/0029-554X(79)90417-8`.
URL `https://www.sciencedirect.com/science/article/pii/0029554X79904178`

33

[46] N. Kornilov, I. Fabry, S. Oberstedt, F.-J. Hambsch, Total characterization of neutron detectors with a 252cf source and a new light output determination, Nuclear Instruments and Methods in Physics Research Section A: Accelerators, Spectrometers, Detectors and Associated Equipment 599 (2) (2009) 226–233. doi:https://doi.org/10.1016/j.nima.2008.10.032.
URL https://www.sciencedirect.com/science/article/pii/S0168900208015519

[47] A. Naqvi, M. Al-Ohali, M. Nagadi, A. Bari, Response function measurement of a deuterated scintillator using a 241ambe source, Nuclear Instruments and Methods in Physics Research Section A: Accelerators, Spectrometers, Detectors and Associated Equipment 353 (1) (1994) 156–159. doi:https://doi.org/10.1016/0168-9002(94)91626-8.
URL https://www.sciencedirect.com/science/article/pii/0168900294916268

[48] A. Enqvist, C. C. Lawrence, B. M. Wieger, S. A. Pozzi, T. N. Massey, Neutron light output response and resolution functions in ej-309 liquid scintillation detectors, Nuclear Instruments and Methods in Physics Research Section A: Accelerators, Spectrometers, Detectors and Associated Equipment 715 (2013) 79–86. doi:https://doi.org/10.1016/j.nima.2013.03.032.
URL https://www.sciencedirect.com/science/article/pii/S0168900213003203

[49] F. Gagnon-Moisan, M. Reginatto, A. Zimbal, Results for the response function determination of the compact neutron spectrometer, Journal of Instrumentation 7 (03) (2012) C03023.

[50] J. Czirr, D. Nygren, C. Zafiratos, Calibration and performance of a neutron-time-of-flight detector, Nuclear Instruments and Methods 31 (2) (1964) 226–232. doi:https://doi.org/10.1016/0029-554X(64)90163-6.
URL https://www.sciencedirect.com/science/article/pii/0029554X64901636

[51] R. Pywell, B. Sawatzky, J. Ives, N. Kolb, R. Igarashi, W. Wurtz, Light output response

34

of bc-505 liquid scintillator, Nuclear Instruments and Methods in Physics Research Section A: Accelerators, Spectrometers, Detectors and Associated Equipment 565 (2) (2006) 725–730.

35

133

Appendix
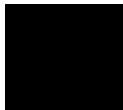
A.1 GEANT4 Geometry, Material and Scintillator-Emission Spectra

A.1.1 Geometry and Material Definitions

Material definitions used for each liquid organic scintillator can be found in Table A.1.1.

Table A.1.1: Material definitions for scintillator simulations.

Scintillator	NE 213A [33]	EJ 305 [30]	EJ 331 [31]	EJ 321P [32]
Density [g/cm^3]	0.873 [79]	0.893	0.890	0.850
Element: H ([% w/w])	91.0 [79]	90.0	9.25	14.6
Element: C ([% w/w])	9.0 [79]	10.0	89.25	85.4
Element: Gd ([% w/w])	-	-	1.5	-
Refractive index	1.505 [79]	1.505	1.500	1.470
Absorption length [m]	2.5 [79]	3.0	4.5	6.0

Material definitions used for the EJ 520 reflective paint which lines the inside of the aluminum cup can be found in Tables A.1.2 and A.1.4. Due to lack of documentation, a combination of EJ 520 [55] and EJ 510 [60] material definitions were used. It is anticipated that this approximation had a negligible effect on the accuracy of the simulation results. For simplicity, the paint was approximated using the `G4OpticalSurface` class on the aluminum cup/liquid organic scintillator interface with `SetType(dielectric_metal)` [80, 81]. The `dielectric_metal` model type makes the optical surface 100% reflective.

Material definitions used for the borosilicate window which separates the scintillator from the light guide can be found in Tables A.1.2 and A.1.5.

Material definitions used for the PMMA light guide which bridges the distance between the optical window and the PMT can be found in Tables A.1.2 and A.1.6.

Material definitions used for the EJ 510 reflective paint which is used on the outside of the light guide can be found in Tables A.1.2 and A.1.3. The EJ 510 paint was geometrically modeled[2] and a `G4OpticalSurface` class with `SetType(dielectric_metal)` was implemented on the light guide/EJ 510 coating interface.

The PMT window was modeled with the same material definitions as the borosilicate window material above. A parabola shape was coded out of the backside of the PMT window and replaced with a new geometry representing the photocathode surface on the inside of the PMT.

---

[2]The paint was modelled as 110 μm thick, as per manufacturer documentation for application.

Table A.1.2: Material definitions for EJ 510, EJ 520, borosilicate and PMMA.

Scintillator	EJ 510 [60]	EJ 520 [55]	Borosilicate[56]	PMMA[59]
Density [g/cm^3]	1.182	1.182 [60]	2.230	1.190
Element: H ([% w/w])	2.9	2.9 [60]	-	8.0
Element: B ([% w/w])	-	-	6.6	-
Element: C ([% w/w])	17.2	17.2 [60]	-	60.0
Element: O ([% w/w])	38.8	38.8 [60]	47.5	32.0
Element: Na ([% w/w])	-	-	1.3	-
Element: Al ([% w/w])	-	-	8.4	-
Element: Si ([% w/w])	-	-	34.7	-
Element: K ([% w/w])	-	-	1.5	-
Element: Ti ([% w/w])	51.1	41.1 [60]	-	-
Refractive index	Table A.1.3	Table A.1.4	Table A.1.5	Table A.1.6
Reflectivity	Table A.1.3	Table A.1.4	Table A.1.5	Table A.1.6
Absorption length [m]	Table A.1.3	Table A.1.4	Table A.1.5	Table A.1.6

Figure A.1.1 shows a cross-sectional view of the simulated detector geometry and materials. As a rule, no gaps between material interfaces were used. All materials in contact were defined to share the same plane.
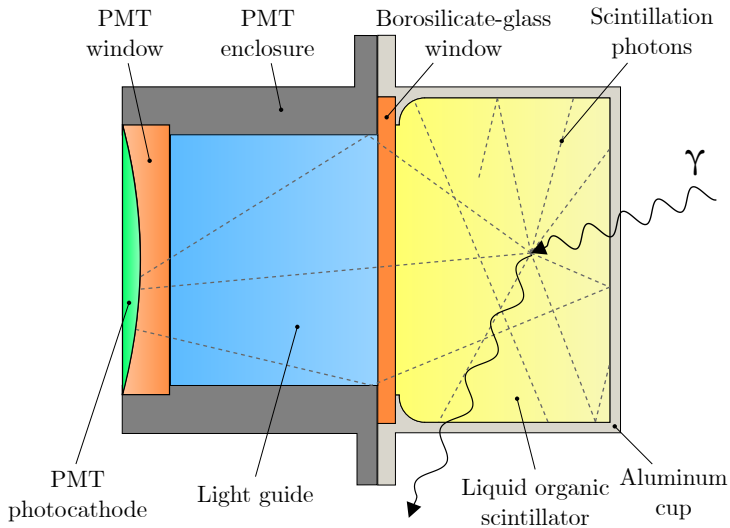

Figure A.1.1: Detector geometry overview. A typical gamma-ray interaction is shown.

Table A.1.3: Material definitions for EJ 510 reflective paint. Data from Ref. [60] and as TiO_2 from Ref. [82].

Wavelength [nm]	Refractive index	Reflectivity	Absorption length [mm]
400	2.68	0.917	4.9
405	2.66	0.938	7.6
410	2.64	0.946	11.7
415	2.63	0.950	17.7
420	2.62	0.954	26.7
425	2.61	0.956	39.7
430	2.59	0.958	58.7
435	2.58	0.957	85.9
440	2.57	0.959	124.7
445	2.56	0.958	179.7
450	2.55	0.960	256.5
455	2.54	0.960	363.7
460	2.53	0.961	511.6
465	2.53	0.959	715.4
470	2.52	0.959	990.5
475	2.51	0.961	1357.9
480	2.51	0.962	1855.0
485	2.50	0.962	2523.1
490	2.49	0.961	3406.3
495	2.49	0.961	4577.1
500	2.48	0.961	6095.0

Table A.1.4: Material definitions for EJ 520 reflective paint. Data from Refs. [55, 60] and as TiO_2 from Ref. [82].

Wavelength [nm]	Refractive index	Reflectivity	Absorption length [mm]
400	2.68	0.827	4.9
405	2.66	0.854	7.6
410	2.64	0.875	11.7
415	2.63	0.892	17.7
420	2.62	0.904	26.7
425	2.61	0.914	39.7
430	2.59	0.921	58.7
435	2.58	0.926	85.9
440	2.57	0.927	124.7
445	2.56	0.928	179.7
450	2.55	0.928	256.5
455	2.54	0.927	363.7
460	2.53	0.927	511.6
465	2.53	0.927	715.4
470	2.52	0.927	990.5
475	2.51	0.927	1357.9
480	2.51	0.927	1855.0
485	2.50	0.923	2523.1
490	2.49	0.923	3406.3
495	2.49	0.924	4577.1
500	2.48	0.924	6095.0

Table A.1.5: Material definitions for borosilicate glass. Data from Refs. [56] and as SCHOTT Borosilicate from Ref. [82].

Wavelength [nm]	Refractive index	Absorption length [mm]
400	1.484	235.9
405	1.483	234.6
410	1.483	233.6
415	1.482	232.5
420	1.482	231.5
425	1.481	230.4
430	1.481	229.4
435	1.480	228.4
440	1.480	227.6
445	1.480	226.8
450	1.479	226.0
455	1.479	225.2
460	1.478	224.4
465	1.478	223.6
470	1.478	223.1
475	1.477	222.3
480	1.477	221.5
485	1.477	221.0
490	1.476	220.4
495	1.476	219.8
500	1.476	219.2

Table A.1.6: Material definitions for PMMA using `G4_PLEXIGLASS` base material and adding PMMA from Ref. [82].

Wavelength [nm]	Refractive index	Absorption length [mm]
400	1.505	235.9
405	1.505	234.6
410	1.504	233.6
415	1.503	232.5
420	1.503	231.5
425	1.503	230.4
430	1.502	229.4
435	1.502	228.4
440	1.501	227.6
445	1.500	226.8
450	1.500	226.0
455	1.500	225.2
460	1.499	224.4
465	1.498	223.6
470	1.498	223.1
475	1.498	222.3
480	1.497	221.5
485	1.496	221.0
490	1.496	220.4
495	1.496	219.8
500	1.496	219.2

A.1.2 GEANT4 Scintillator Emission Spectra

A wavelength dependent emission spectrum for each scintillator material was included in the simulation. Figure A.1.2 shows the scintillation emission spectra for all four scintillators while Table A.1.7 shows the numerical representation used in the simulation framework.
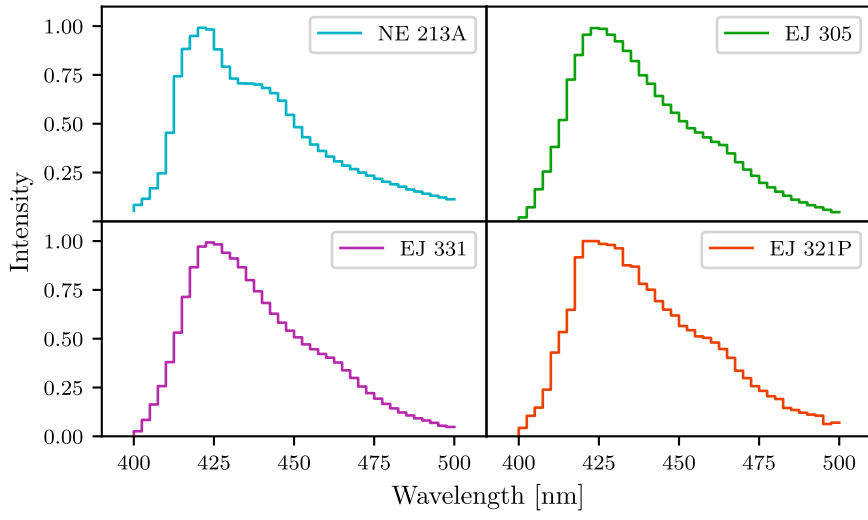
Figure A.1.2: Wavelength-dependent scintillation emission spectra.

Table A.1.7: Wavelength-dependent emission. Data from Refs. [33, 30, 31, 32].

Wavelength [nm]	NE 213A	EJ 305	EJ 331	EJ 321P
400	0.054	0.000	0.011	0.000
402	0.084	0.020	0.026	0.043
405	0.116	0.072	0.084	0.105
407	0.170	0.164	0.163	0.147
410	0.246	0.255	0.257	0.239
412	0.454	0.381	0.380	0.429
415	0.743	0.519	0.531	0.534
417	0.883	0.726	0.714	0.648
420	0.949	0.852	0.866	0.917
422	0.991	0.956	0.972	1.000
425	0.983	0.990	0.993	1.000
427	0.881	0.986	0.983	0.985
430	0.792	0.956	0.940	0.980
432	0.731	0.922	0.911	0.963
435	0.707	0.873	0.866	0.876
437	0.706	0.821	0.800	0.869
440	0.701	0.748	0.743	0.781
442	0.683	0.705	0.683	0.751
445	0.657	0.642	0.628	0.692
447	0.618	0.597	0.582	0.649
450	0.545	0.556	0.541	0.619
452	0.483	0.513	0.507	0.565
455	0.431	0.477	0.471	0.544
457	0.394	0.455	0.446	0.512
460	0.361	0.430	0.422	0.504
462	0.332	0.407	0.403	0.480
465	0.307	0.391	0.378	0.447
467	0.286	0.348	0.338	0.402
470	0.268	0.303	0.299	0.336
472	0.250	0.265	0.255	0.298
475	0.234	0.233	0.221	0.257
477	0.218	0.197	0.193	0.233
480	0.203	0.174	0.166	0.205
482	0.190	0.152	0.143	0.191
485	0.177	0.131	0.122	0.145
487	0.163	0.111	0.107	0.135
490	0.153	0.097	0.092	0.121
492	0.141	0.083	0.081	0.111
495	0.131	0.072	0.069	0.106
497	0.122	0.059	0.054	0.063
500	0.113	0.047	0.048	0.070

Since the simulation also accounted for the wavelength-dependent quantum efficiency at the photocathode [61], the resulting photoelectron conversion spectrum looked slightly different for each scintillator material. Figure A.1.3 shows the wavelength-dependent quantum efficiency employed in the simulation. The relevant scintillation emission range (400 − 500 nm) of the scintillator materials employed, is also highlighted.
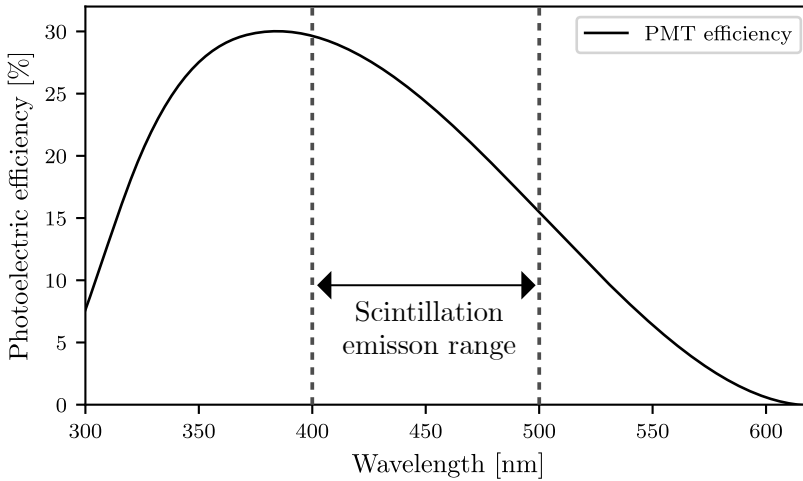

Figure A.1.3: PMT quantum efficiency. The typical scintillation emission range is also shown. Data from Ref. [61]

A.2   A Design for an Active Moderator

One of the original goals of the author was to extend the fast-neutron tagging method [64, 68] into the domain of thermalized neutrons. A significant portion of time was spent on the concept and design of a liquid scintillation-based active moderator. Employing a high ^{1}H/^{12}C ratio scintillator to increase the neutron moderation efficiency, the aim was to identify a thermalizing neutron signature in the moderator. Coupled with a thermal-neutron sensitive detector, the thermalizing signature would provide an additional timing reference, allowing the reconstruction of the full process chain from the decay to the detection of a thermalized neutron.

The active moderator design employs an existing 3 in. PMT and light-guide assembly and includes a μ-metal shield. The width and depth of the scintillator cell is constrained by the size of the light guide. Figure A.2.4 shows a cross-sectional view of the assembly and highlights the relevant parts. The main scintillator cell volume is made of 5 mm thick aluminum and encloses a volume of 4 l. A 8.8 mm borated glass window separates the scintillator volume and light guide. The protruding expansion chamber houses the gas bubble, which normally forms during the filling of the cell, away from the borated glass surface. This maximizes light transmission from the scintillator to the light guide. Figure A.2.6 shows different views of the aluminum construction of the active moderator.

A beneficial side effect of the gas bubble is that it serves as a pressure regulator (since the liquid scintillator is incompressible) during thermal expansion and contraction cycles due to temperature changes. A pressure ring and spring assembly keeps the PMT and light-guide assembly in contact with the glass window.

This detector is envisioned as a first prototype of an active moderator to enable initial testing and tagging of thermalized neutrons in a proof-of-concept experiment. Ideally, simulation work will be used to give a better understanding of the optimal volume of the active moderator for a future improved version. This will need to take into account the material properties of the scintillator used as well as the energy range of the neutron source employed. This active moderator may allow for the transfer of the methodologies and results presented as part of this work towards the development of a thermal-neutron tagger.

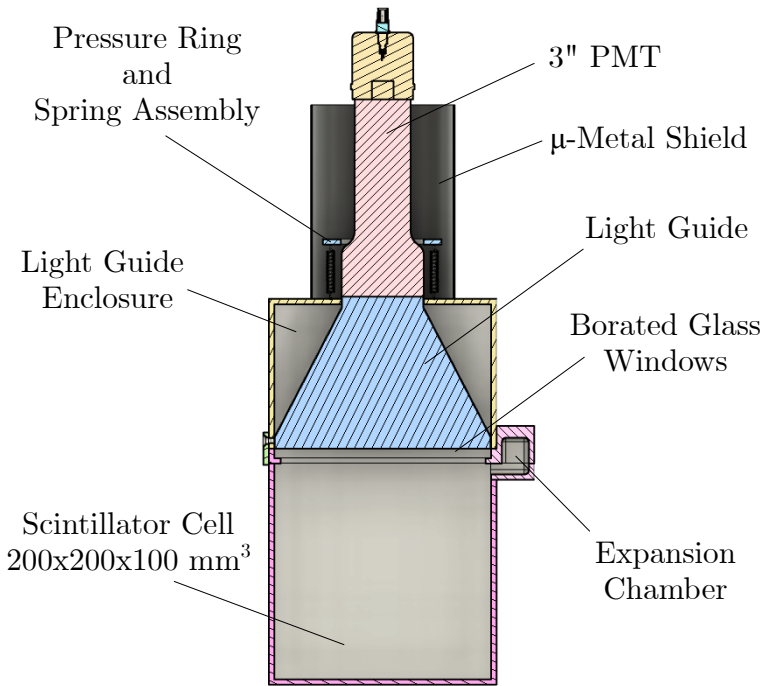Figure A.2.5 show the fabricated components before and after assembly.

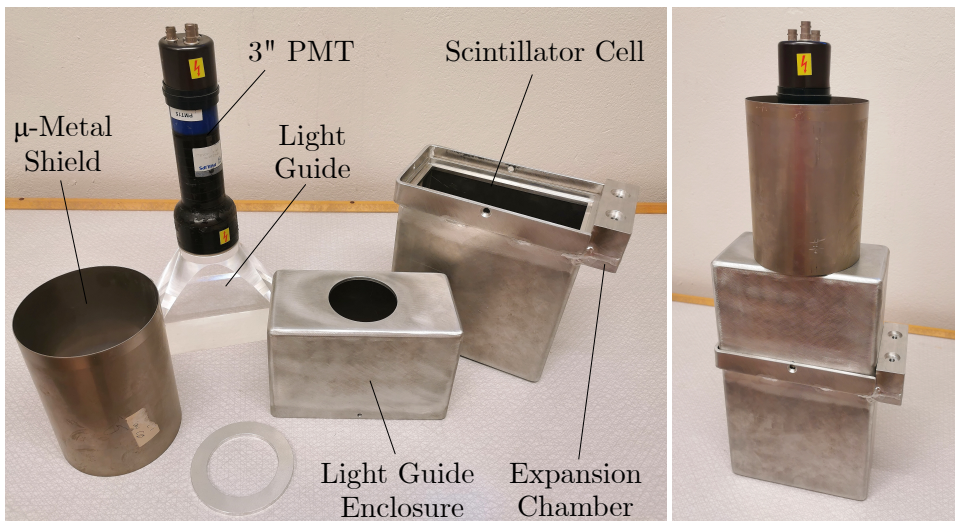**Figure A.2.4:** A cross-sectional view of the active moderator. Major components are highlighted.

Figure A.2.5: Active moderator before and after assembly. Major components are highlighted.
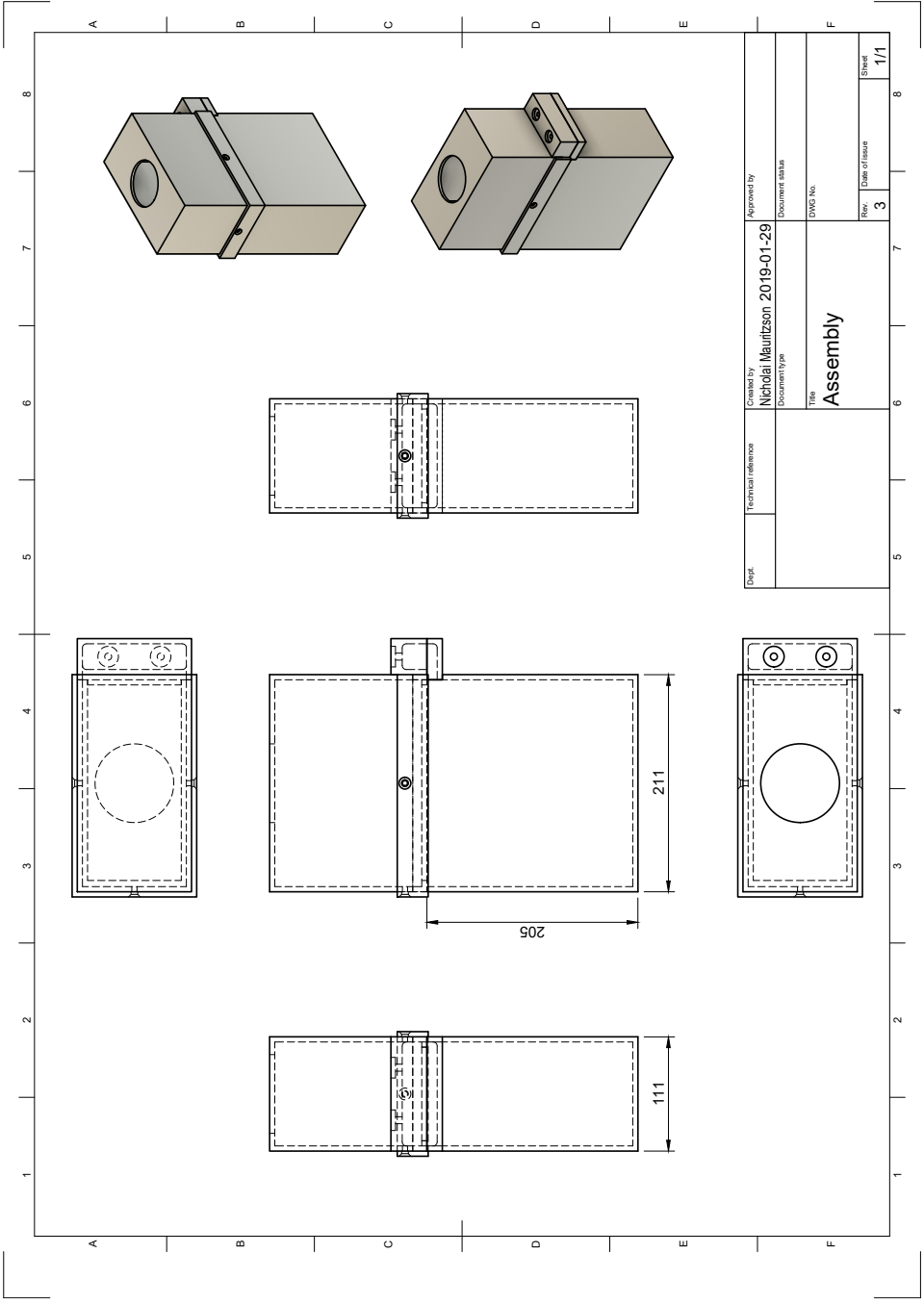
Figure A.2.6: CAD drawing of the active moderator vessel.

A.3 Improving Student Labs During COVID-19 Restrictions

During 2020 and the start of the COVID-19-related restrictions, students were restricted from visiting Lund University and course-responsible teachers were given the task to convert their teaching activities to fit an online format. This also included the accompanying laboratory exercises. It presented itself as an opportunity for restructuring and rethinking of some of the well-established laboratory exercises. New tools and approaches to pedagogy were developed to suit the new situation. While some labs where given completely online, others were deemed unsuitable for online formats and received special permission for on-campus teaching. For these special cases, a maximum of 4 students were allowed to attend each session for a maximum of 3 hours, in contrast to the usual groups of 8 students working in pairs for half- or full-day experiments. It was therefore decided to prioritize the interaction of the student with the experiment itself and have the teacher focus on guiding rather than lecturing.

To obtain the same learning outcome, additional preparation by the students was required. The lab manuals and related materials were rewritten with clear and step-wise instructions and published online. Specific changes and improvements included the recording of videos which gave guided tours of the laboratory environment and explained specific lab concepts. Care was taken to make these videos as general as possible allowing different labs on similar subject matter to reuse relevant videos. Also, online quizzes were prepared for each student to complete before attending the lab. These highlighted the major focus of each lab with the goal of making it clear to students what was expected from them. Finally, Jupyter Notebooks[83] were employed (an interactive document able to run in a normal web-browser) to allow for easy visualization and aid in numerical analysis all in one place. The tools within the notebook were developed using the Python programming language [84] and ran in the background producing the relevant results based on the input of the students. This facilitated a focus on subject matter rather than on analysis or data management. For those labs which had to be run completely online, analytical or numerical simulation tools were also developed using Jupyter Notebooks. For instance, one such simulation allowed the student to "run" the data acquisition of a detector using a radioactive source and observe the evolution of a pulse-height spectrum over time, similar to using the real data-acquisition normally used in the lab.

Overall, the student feedback showed that the streamlined way of handling data management and analysis using Jupyter Notebooks was very positively received. Furthermore, the additional workload put to the students, in terms of pre-lab preparations, was also very positively received since it allowed them to better understand the focus of the lab. This had the effect of increasing the confidence of the students which also increased their level of participation. An overview of the results and experience of the author was published in Fysikaktuellt Nr. 4 on December 2020 and is included below.
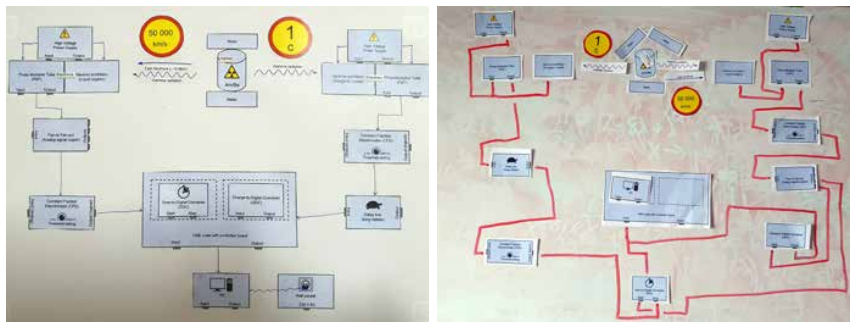
FIGUR 1: Inför laborationerna får studenterna klippa och klistra ihop ett flödesschema över hur experimentet ska utföras.

Nya metoder gav bättre laborationer

I Lund innebar pandemin att formatet för laborationer uppdaterades – och i slutändan blev bättre.

Å r 2020 har varit en stor utmaning för alla som är inblandade i undervisning. Som en reaktion på den rådande pandemin fick kursansvariga i uppgift att på mycket kort tid göra om sina kurser till ett onlineformat. All undervisning skulle göras på distans. Detta gällde även för experimentella laborationer som ur en undervisningssynpunkt är en nyckelkomponent för många fysikkurser. Under höstterminen har vi återigen haft möjlighet att erbjuda laborationer i sal, men med en del begränsningar. Vi konstaterade tidigt att dessa begränsningar krävde en uppdatering av det tidigare laborationsformatet. På grund av detta inleds en modernisering av våra laborationer i kärnfysik. Vi vill här dela med oss av våra och studenternas erfarenhet av dessa förändringar.

Det nya laborationsformatet

Laborationer som handlar om mätning, karakterisering och avskärmning av olika typer av strålning brukar ges som antigen halv- eller heldagslaboration. En av de införda begränsningarna är att salstiden får vara max tre timmar.

Vi bestämde oss för att studenternas interaktion med experimentet skulle vara i fokus: handledaren ska leda mer och undervisa mindre så att tiden som studenterna sitter och passivt lyssnar minimeras.

För att uppnå detta mål krävdes mer omfattande förberedelser från studenternas sida inför laborationerna. Vi ville att dessa förberedelser skulle har tydliga mål för att främja en mer effektiv laborationsmiljö, med en tydlig "röd tråd" för studenterna att följa. Enligt denna princip (nära kopplad till så kallat "flipped classroom") skrev vi om allt material för varje laboration och gjorde detta tillgängligt för studenterna via onlineplatformen "Canvas" (som används på Lunds universitet). Vi gjorde följande ändringar och tillägg för laborationerna:
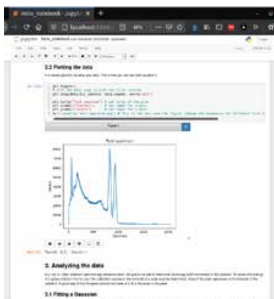
■ **Video** som introducerar den underliggande fysiken men också visar laborationssalen och försöksuppställning. Varje video var mindre än tio minuter lång och spelades in av samma handledare som ansvarade för laborationen.

■ **Läsmaterial** från läroboken samt andra relevanta källor sammanställdes i en lista. Detta gav en övergripande struktur med överlappande läsuppdrag mellan de olika laborationerna.

Manualerna till laborationerna skrevs om med ett fokus på laborationens uppställning samt uppgifterna, helt utan någon teorisektion.

■ **Quiz** som täckte relevanta frågor för varje laboration var ett obligatoriskt moment som varje student behövde klara innan de kunde delta i laborationen. Studenterna kunde ta detta quiz flera gånger men var tvungna att svara rätt på alla frågor. Syftet med detta var att både säkerställa förkunskaperna hos studenterna och att tydliggöra vad som förväntades av dem.

■ **Klipp ut-papper** som visar de experimentella komponenter som studenterna ska använda i en specifik laboration. Från "klipp ut-pappret" får studenterna välja vilka komponenter som de tror behövs och klippa ut dessa. Studenterna skall sedan ordna ett kopplingschema med komponenterna i en rimlig ordning. Detta ger dem möjlighet att koppla den abstrakta kunskapen från läsmaterialet till en konkret förståelse av uppbyggnaden av experimentet. Figur 1 visar två exempel på studenternas lösningar på denna uppgift.

Att erbjuda en variation av förberedelseuppgifter och inlärningsmaterial gör ▶

149

FIGUR 2: Jupyter Notebook kombinerar instruktioner, kod och resultat.
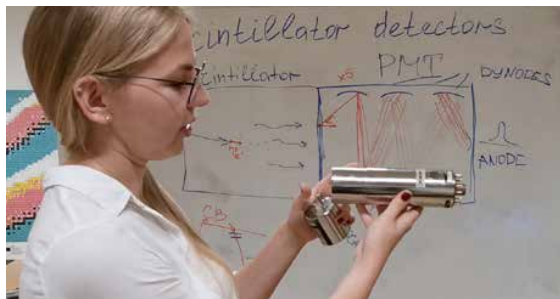
Den handledare som håller i laborationen spelar in en kort video som både introducerar den underliggande fysiken och visar försöksuppställningen.

▶ att vi också tar hänsyn till studenternas olika inlärningsstilar.

Vi förberedde också ett Jupyter Notebook-dokument för samtliga laborationer. Detta är ett interaktivt dokument som studenterna kan arbeta med i en vanlig webbläsare. Jupyter Notebook blandar beskrivande text och programmeringskod på ett pedagogiskt sätt och studenterna kan importera sin data, ändra parametrar, benämna axlar på en graf och visa resultat (till exempel figurer) direkt i dokumentet. Vi skrev koden i Python, men andra programmeringsspråk kan användas. I dokumentet tog vi också med frågor som studenterna ska svara på, vilket även gör dessa Notebooks lämpliga som inlämningsuppgifter.

Eftersom det var första gången många av studenterna kom i kontakt med Jupyter Notebook, förberedde vi en separat "introduktions"-Notebook som vi presenterade under en vanlig föreläsning där studenterna själva kunde testa koden och funktionerna. Figur 2 visar ett exempel av en Jupyter Notebook från studentens perspektiv.

Tre timmar i laborationssalen

Vi blev mycket positivt överraskade av hur bra den nya laborationsstrukturen fungerade i praktiken. Vi var från början beredda på att det skulle uppstå problem gällande hantering av Jupyter Notebook och att studenterna inte skulle ta till sig all den förberedelseinformation som vi gav dem. Men vi hade fel!

Studenterna kom bättre förberedda till laborationerna och mindre tid behövdes till teorigenomgång. Genom att också använda ett interaktivt verktyg, Jupyter Notebook, för analysen blev kommunikationen av laborationens metod och resultat mer transparent och tydligt. Denna ökade effektivitet gav oss möjligheten att använda mer tid till fördjupande frågor, diskussion och även eventuella sidospår som studenterna var nyfikna på. Detta ledde till en öppen och stressfri atmosfär där såväl studenterna som handledaren kunde känna sig bekväma.

Överlag behövdes handledaren mindre i "bredden" och mer i "spetsen" för diskussion och slutsats av experimentet.

Studentens perspektiv

För att ge oss möjlighet att förstå hur studenterna tillägnade sig detta nya upplägg bad vi varje laborationsgrupp att lämna in en anonym utvärdering av sina upplevelser i form av en kort blankett. Vi ställde frågor som "Vad var det bästa med laborationen?", "Vad var det sämsta med laborationen?", "Saknade du någon information under/innan laborationen" och "Vad har du lärt dig av laborationen?". Studenternas svar var överväldigande positiva.

Bland annat så uppskattade majoriteten av studenterna att vi införde mer förberedelsekrav inför laborationerna. De tyckte att detta gav en bättre insikt i vad syftet med laborationerna var. Resultatet var att studenterna visade större självförtroende och ökad villighet att ställa frågor och inledda diskussioner med varandra och med handledaren.

Det framgick också av studenternas respons att det inte räcker att bara ställa högre krav på förberedelserna inför laborationen. Det var de högre kraven i kombination med att vi förberett specifika läsanvisningar, videor där vi förklarade teorin samt en quiz som gav studenterna denna djupare insikt i syftet med laborationerna.

Ökat engagemang

Det som började med en anpassning av laborationerna till pandemins krav resulterade i ett nytt undervisningsformat som uppskattas av både studenter och handledare.

Det står nu klart för oss att vi tidigare underskattat studenternas engagemang och ambitioner, men att vi nu med ett strukturerat och varierande förberedelsematerial lyckats ta tillvara dem bättre. Eftersom studenterna var bättre förberedda var de också mindre beroende av handledning och kunde jobba mer självständigt under hela laborationsmomentet.

NICHOLAI MAURITZSON
OCH HANNO PERREY
Lunds universitet

Faculty of Science
Department of Physics

ISBN 978-91-8039-556-4